Transportphänomene in biologischen Membranen: Simulation von Massen-, Impuls- und Wärmetransport

Nicht-Gleichgewicht-Simulationen an Zellmembran-Modellsystemen

TECHNISCHE
UNIVERSITÄT
DARMSTADT

Vom Fachbereich Chemie
der Technischen Universität Darmstadt

Zur Erlangung des akademischen Grades
eines Doktor rerum naturalium (Dr. rer. nat.)

genehmigte Dissertation

eingereicht von
Dipl. Chem. Thomas J. Müller
aus Winterthur (Schweiz)

Berichterstatter:	Prof. Dr. Florian Müller-Plathe
Mitberichterstatter:	Prof. Dr. Markus Biesalski

Eingereicht am:	2. November 2009
Mündliche Prüfung am:	14. Dezember 2009

Darmstadt 2010

D 17

I. Inhaltsverzeichnis

II. Abbildungsverzeichnis

Die mit Buchstaben gekennzeichneten Figuren finden sich in den in dieser Arbeit zusammengefassten Publikationen:

[a] J. Chem. Phys. 129 (2008) 014102
[b] J. Hazard. Mat. 138 (2009) 13-24
[c] ChemPhysChem 10 (2009) 2305-2315
[d] Vorgesehen für International Journal of Quantum Chemistry
[e] Fluid Phase Equilibria 274 (2008) 27-35

III. Dissertationszeitraum

Die in dieser Dissertation zusammengefassten Arbeiten wurden in der Forschungsgruppe von Prof. Dr. Florian Müller-Plathe von Januar 2005 bis September 2009 durchgeführt. Die Themen wurden bis Mai 2005 an der International University Bremen (heute Jacobs University Bremen) und ab Juni 2005 an der Technischen Universität Darmstadt bearbeitet.

1. Zusammenfassung und Einleitung / Summary and Introduction

1.1. Membranen im Nicht-Gleichgewicht – ein Abriss

Die biologische Zelle, der Baustein allen Lebens, ist seit ihrer Entdeckung durch Robert Hook 1665 ein Objekt wissenschaftlicher Untersuchungen der verschiedensten naturwissenschaftlichen Disziplinen. Musste zunächst durch Louis Pasteur und andere im 19. Jahrhundert noch widerlegt werden, dass Zellen spontan aus toter Materie entstehen können, so hat sich im Laufe des letzten Jahrhunderts mit dem Verständnis von Zellen auch eine biologische Definition für das Leben entwickelt. [1] Die Grundlage für alle Voraussetzungen von Leben wie die Zusammensetzung aus verschiedenen Komponenten, der Stoff-, Energie- und Informationsaustausch mit der Umgebung, das Wachstum und die Fortpflanzung ist die Existenz einer klaren Abgrenzung nach aussen. In der biologischen Zelle übernimmt diese Rolle die Zellmembran, deren Eigenschaften als strukturbildendes Element und vor allem als selektiv permeabler Abteilbildner Physiker, Chemiker und Biologen in unzähligen Experimenten untersucht haben. Diese Doktorarbeit auf der Basis von Computersimulationen vereint interdisziplinär nun numerisch-mathematische Methoden, die auf grundlegenden physikalischen Gesetzen, den Newtonschen Bewegungsgleichungen, basieren, um aus dem Blickwinkel eines Chemikers physikalische Eigenschaften von biologischen Phänomenen zu untersuchen.

Der Aufbau der Membran einer eukariotischen Zelle ist hoch komplex [2]. Das zentrale Element ist eine Doppelschicht aus Lipiden, deren hydrophobe Schwanzgruppen einander zugewandt sind, während vom Zentrum der Zellle aus gesehen, die hydrophilen Kopfgruppen der äusseren Schicht nach aussen und die Kopfgruppen der inneren Schicht ins Zellinnere gerichtet sind. Auf der Aussenseite findet man die Kohlenhydrat-Glykokalyx (aufgebaut aus Polysacchariden), während im Inneren ein polymeres Netzwerk aus Proteinen als ein gummiartiges Zytoskelett der Membran Stabilität verleiht. Zusätzliche in die Membran integrierte Proteine und Polypeptide sorgen u.a. für Stofftransport durch die per se nur schwer durchdringbare Membran. Im Rahmen der hier präsentierten Forschungsergebnisse wurde die Membran aufgrund der Limitierung der Computerleistung auf die zentrale Lipiddoppelschicht als Modellsystem beschränkt.

Computersimulationen werden bereits seit über 50 Jahren zur theoretischen Vorhersage von physikochemischen Eigenschaften verschiedenster chemischer Systeme angewendet. Im Laufe der Zeit wurden hierzu viele Programme entwickelt, wovon das für diese Arbeit verwendete YASP [3,4] den Vorteil hat, dass der „Reverse Non-Equilibrium Molecular Dynamics (RNEMD)“ Algorithmus [5] bereits implementiert war. Im Zusammenhang mit Nicht-Gleichgewichts-Simulationen an Membranen ist der RNEMD Algorithmus, der im Methodenteil von Kapitel 2 sowie in Kapitel 3 und 4 anhand akuteller Fragestellung eingehender beschrieben wird, ein zentraler Aspekt. Die erstmalige Anwendung dieser Methode auf Systeme mit konstanter Teilchenzahl, konstanter Temperatur und konstantem Druck (*NpT*), bzw. die erstmalige Anwendung auf Systeme mit stark geordneter Struktur führten neben der biologischen Anwendung zu neuen methodischen Herausforderungen und Fragestellungen.

In der vorliegenden kumulativen Doktorarbeit fasse ich nun meine sämtlichen Arbeiten (publizierte Artikel und vorbereitete Artikel) zusammen, die zum Thema der Nicht-Gleichgewichts-Simulationen angefertigt wurden.

Bevor die Resultate der Berechungen präsentiert werden, finden sich in einem ersten Teil die theoretischen Grundlagen. Da zu den Grundlagen von Computersimulationen aber bereits eine ausgiebige Literatur existiert, beschränke ich mich hier darauf, den RNEMD Algorithmus detailliert vorzustellen. Dabei werden nicht nur die theoretischen Grundlagen, sondern auch der aktuelle Wissensstand bezüglich der Methode und aktuelle Anwendungsbeispiele behandelt.

Im ersten angewandten Teil sind die vorbereitenden Arbeiten zu den weiteren Simulationen zusammengefasst. Darin zeige ich anhand von einfachen Gasen und Flüssigkeiten auf, dass der

RNEMD Algorithmus auch auf *NpT* Systeme anwendbar ist, und welche Kriterien dabei besonders zu beachten sind. Da, um den Druck eines Systems festzusetzen, nach jedem Zeitschritt das Reskalieren der Atompositionen notwendig wird, muss zunächst geklärt werden, ob der Einfluss dieses Rechenschrittes auf das Endresultat vernachlässigbar ist, bevor solche Berechnungen in den folgenden Kapiteln Anwendung finden können.

Der Hauptteil der Resulate findet sich in Kapitel vier, welche in drei Unterkapitel unterteilt ist.

Das erste Unterkapitel beschäftigt sich mit der Durchdringbarkeit der Dipalmitoylphosphatidylcholin (DPPC) Membran, welche als Modellsystem gewählt wurde. Den Vorteil von Computersimulationen der ungefährlichen Untersuchung auch von gefährlichen Stoffen ausnutzend (resp. das Ersetzen von Tierversuchen durch Computerberechnungen), vergleiche ich Mobilität und Ausrichtung des Kampfstoffes Senfgas und des Alkans Heptan während des erzwungenen Durchdringens der Membran. Im Gegensatz zu den anderen beiden Kapiteln kommt hier das Nichtgleichgewicht nicht durch den RNEMD Algorithmus, sondern durch Anlegen von konstanten äusseren Kräften an den Testmolekülen zustande.

Im nächsten Unterkapitel wird unter Verwendung der RNEMD Methode die Membran einer Scherkraft ausgesetzt. Die daraus resultierende Verscherung der einzelnen Lipidschichten gegeneinander wird nicht nur global, wie das schon anhand von Coarse-Grained-Simulationen (Berechnungen, die um Resourcen und Zeit zu sparen, die aus einzelnen Atomen bestehenden Moleküle durch wenige Superatome annähern) gezeigt wurde, sondern in atomistischer Auflösung aufgezeigt und interpretiert. Die Definition einer lokalen Scherviskosität ist dabei ein zentrales Instrument.

Das letzte Unterkapitel beschäftigt sich ein weiteres Mal mit dem RNEMD Algorithmus. Statt wie im vorhergehenden Unterkapitel Impuls auszutauschen, was eine Scherung zur Folge hat, wird nun Wärme ausgetauscht, wodurch im System ein Temperaturgradient entsteht, der die Untersuchung der Wärmeleitfähigkeit erlaubt. Hier wird aufgezeigt, inwieweit die RNEMD Resultate dieses Systems interpretiert werden können und ab wann weitere Modifikationen an der Simulationskonfiguration notwendig werden.

Mit Kapitel fünf, den Folgerungen und einem Ausblick auf weiterführende Untersuchungen, schliesst diese Arbeit.

1.2. Membranes in nonequilibrium – an outline

Since its discovery by Robert Hook in 1665, the biological cell, the building block of all life, has been subject of scientific research in various fields. While in the 19th century Louis Pasteur and others still had to disprove that life can arise from dead matter, in the last hundred years a new definition on the basis of the understanding of the living cell has been developed [1]. This definition includes exchange of matter, energy, and information with the surroundings, growth, and reproduction. One of the major prerequisites is the existence of a well-defined border which separates the life form from its environment. In biological cells, this feature is imposed by the membrane. This structure-building, selectively permeable, compartment-defining element of the cell has been subject to a vast number of experiments of physicist, chemists, and biologists. This PhD thesis focuses on the physical properties of biological systems from the point of view of a chemist. This interdisciplinary approach is executed by computer calculations on the basis of the fundamental physical laws of Newton.

The structure of the membrane of a eukaryotic cell is very complex [2]. The central element is a double layer of lipids whose hydrophobic tail regions are pointing toward each other. The hydrophilic head groups are oriented either towards the center of the cell or towards the outside of the cell. The outer monolayer is covered by a carbohydrate glycocalyx (made of polysaccharides) while the inner layer of the membrane is stabilized by a network of proteins which form a rubber like cytoskeleton. Additional proteins and polypeptides are incorporated into the lipid double layer. They support mass transport through the otherwise hardly penetrable membrane. Limited by the currently available computational power all simulation presented in this work are executed on a model system which concentrates on the central lipid bilayer.

Since more than fifty years computer simulations have been used to predict physicochemical properties of numerous chemical systems. During this period many programs have been developed. The program YASP [3,4], which is used in this work, has the advantage that the “Reverse Non-Equilibrium Molecular Dynamics” (RNEMD) algorithm [5] has already been incorporated and tested. This method is crucial for the momentum and heat transport part of this work and will be explained in more detail in the theory section in chapter 2 as well as in the publications of sections 3 and 4. For the first time it is applied on systems of constant number of particles, constant temperature and constant pressure (*NpT*). On top of this we apply it for the first time to highly structured systems. Next to the biological questions of the membrane system, this leads to additional questions and challenges from the methodological point of view.

In this cumulative PhD thesis I resume all works (published articles and articles in preparation) which have been written for the topic of non equilibrium molecular dynamics on membranes.

Before presenting the simulation results, a first part of this work is devoted to the theoretical background of the methods in use. Since the fundamentals of molecular simulations are widely covered in literature, I will only focus on the RNEMD algorithm. The theoretical background, the current state of knowledge and recent examples of its application will be presented.

In the first applied part of this thesis preliminary works for the subsequent simulations are summarized. For simple gases and fluids I demonstrate that the RNEMD algorithm can also be applied to *NpT* systems. I also point at the critical conditions for its applicability. Fixing the pressure is imposed by rescaling the atoms positions. Therefore it was important to confirm that the influence of this calculation step on the final results is negligible before applying RNEMD on *NpT* systems in the following chapters.

Chapter four is the main results section of this thesis and is divided into three subsections.

The first section deals with the permeability of a dipalmitoylphosphatidylcholine (DPPC) membrane. This lipid bilayer has been chosen as a model system for the human cell membrane. Making use of the advantage of computer simulation to investigate safely hazardous materials (respectively to substitute animal experiments) I compare the mobility and the orientation of the chemical warfare agent sulfur mustard (mustard gas) and the alkane heptane during a forced penetration process through the membrane. In contrast to the other non equilibrium chapters, the non equilibrium of this chapter is not induced via the RNEDM mechanism but by constant external forces acting on the test molecules.

In the next section, the membrane is exposed to an external shear force induced by the RNEMD method. The resulting shearing of the lipid layers against each other is resolved in atomistic detail. This compares to a global description of the shear process which has been investigated by coarse grained simulations (simulations which simplified the model in order to increase the total simulated time). The definition of a local shear viscosity is a central element of this comparison.

The last section of chapter four deals again with the RNEMD algorithm. Unlike the calculations in the previous section, where momentum has been exchanged to achieve shearing, in this section heat is exchanged. This causes a temperature gradient within the system which allows the investigation of the thermal conductivity. In this section I show to what extent the results of RNEMD calculations of highly structured systems can be interpreted. This chapter will also explain why RNEMD can break down and which modifications might be necessary.

This work concludes with chapter five, the conclusions and an outlook to further investigations.

2. Theorie und Hintergrund: Reverse Non-Equilibrium Molecular Dynamics

2.1. Definition von RNEMD

Die umgekehrte Nicht-Gleichgewichtsmolekulardynamik (engl. reverse non-equilibrium molecular dynamics, abgekürzt RNEMD) ist eine computergestützte Methode der theoretischen physikalischen Chemie zur Berechnung von Transporteigenschaften (z.B. Viskosität und Wärmeleitfähigkeit) von Flüssigkeiten und Gasen.

2.2. Der Algorithmus im Detail

Die Methode basiert auf klassischen Molekulardynamik-Simulationen, deren umfassende Theorie, Besonderheiten der Durchführung, Implementationsaspekte und Anwendungsbeispiele in der gängigen Literatur im Detail beschrieben werden. Diese Doktorarbeit wird diese Grundkenntnisse nicht wiederholen, sondern konzentriert sich auf die spezifischen Neuerungen, welche die RNEMD Methode mit sich bringt. Lesern, die sich eingehender in die Grundlagen der Molekulardynamik einarbeiten wollen, sei 'Computer Simulation of Liquids' [6] empfohlen.

Eine RNEMD Simulation wird analog zu einer gewöhnlichen Molekulardynamik-Rechnung aufgesetzt. Zunächst wird eine Box mit den Dimensionen L_x *x* L_y *x* L_z erzeugt, wobei eine ausgewählte Dimension (für den Rest dieses Artikels L_z) aus technischen Gründen drei mal (empirischer Faktor) so lang wie die anderen beiden Seiten der Box gewählt werden kann. Diese Box wird so mit Molekülen gefüllt, dass die Dichte des simulierten Systems mit experimentellen Werten übereinstimmt. Periodische Randbediungen sorgen für ein virtuell unendliches System.

Diese Box wird zunächst äquilibriert. Dabei gilt zu beachten, dass auch Systeme, welche bereits unter MD Bedingungen äquilibiert wurden (siehe dazu technische Aspekte in Kapitel 3.4), nochmals eine „Äquilibrierung" unter RNEMD Bedingungen erfordern, da das System erst nach einer Relaxationszeit einen stationären Zustand erreicht. In Ermangelung eines besseren griffigen Ausdrucks wird Äquilibrierung hier als Kurzschreibweise für die Simulation bis zum Erreichen eines konvergierten, stabilen stationären Zustands verwandt, obwohl natürlich unter Nichtgleichgewichtsbedingungen nicht strikt von Äquilibrierung im Sinne von „ins Gleichgewicht bringen" gesprochen werden kann.

Äquilibrierung und Produktionsläufe folgen demselben Schema:

1) Eine gewöhnliche Simulation mit *m* Zeitschritten wird ausgeführt. D.h. nur alle *m* Zeitschritte wird der im folgenden genauer beschriebene, RNEMD spezifische Austauschschritt eingelegt. Deshalb spricht man bei *m* auch von der Austauschperiode.

2) Die Simulationsbox wird entlang der ausgezeichneten Raumrichtung L_z virtuell in eine gerade Anzahl n_{tot} gleich grosser Scheiben unterteilt. Die Scheiben stehen senkrecht zur *z*-Achse.

3) Suche in der ersten ($n_{erste}=1$) und in der mittleren ($n_{mitte}=n_{tot}/2+1$) Scheibe jeweils nach

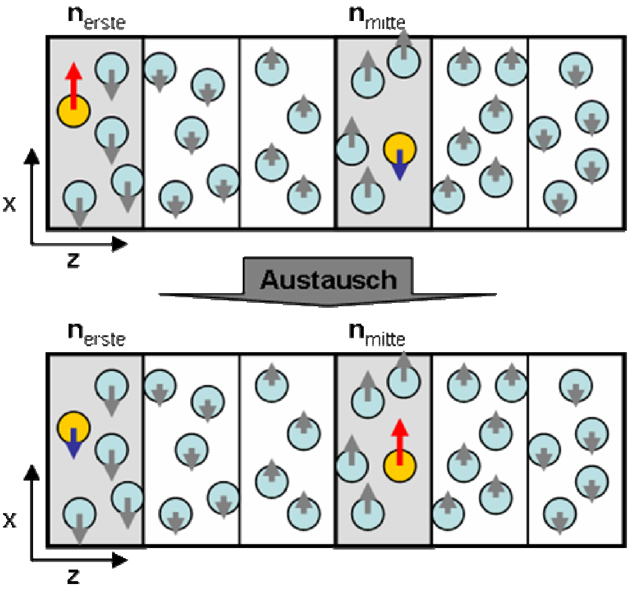

Abb. 1: Schematische Darstellung der RNEMD Methode für Scherviskosität:
In den Austauschscheiben (grau hinterlegt) werden die Impulse (blaue/rote Pfeile) von spezifischen Atomen (gelb) ausgetauscht.

bestimmten Atomen mit jeweils derselben Masse. Nach welchen im einzelnen gesucht wird, hängt von der Fragestellung der RNEMD Simulation ab.

- **Scherviskosität:** Da aufgrund von Scherung ein Impulstransport durch das System erfolgt, wird in der einen Austauschscheibe nach dem Atom mit dem größten Impuls in eine Richtung, in der anderen nach dem Atom mit dem größten Imuls in die entgegengesetzte Richtung gesucht. Dieser Impuls muss rechtwinklig zur ausgezeichneten *z*-Achse gerichtet sein. Im Folgenden wird der Impuls p_x parallel zur *x*-Achse betrachtet.
- **Wärmeleitfähigkeit:** Transport von Wärme resultiert aus einem Temperaturgradienten. Deshalb wird in der einen Austauschscheibe nach dem Atom mit der maximalen kinetischen Energie gesucht und in der anderen nach dem Atom mit der minimalen kinetischen Energie.

4) Vertausche den Impuls entlang der Scherrichtung (bei Scherviskosität) oder die kinetische Energie (bei Wärmeleitfähigkeit) der beiden oben gefundenen Atome. Da die Atome jeweils die gleiche Masse besitzen, reicht hierfür ein Austausch der entsprechenden Geschwindigkeit(en). Dieser Austausch ist absolut unphysikalisch, verändert aber keine Erhaltungsgrößen und führt dazu, dass sich in der Simulationsbox ein Gradient einstellt, den das System auszugleichen versucht.

5) Beginne den Zyklus erneut bei Punkt 1.

Durch den obigen Algorithmus wird ein Impuls-Fluss $j_z(p_x)$ resp. ein Wärmefluss $j_z(Q)$ entlang der *z*-Achse generiert (Herleitung in Kapitel 3.6).

Für die Scherviskosität:

$$j_z(p_x) = \sum_{Austausche} \frac{p_{x,mitte} - p_{x,erste}}{2tL_x L_y} \tag{1}$$

Für die Wärmeleitfähigkeit:

$$j_z(Q) = \sum_{Austausche} \frac{E_{kin,mitte} - E_{kin,erste}}{2tL_x L_y} \tag{2}$$

Jedes System, das eine Störung erfährt, strebt wieder seinem Gleichgewicht entgegen. Bei kleinen, periodischen Störungen, wie sie durch den RNEMD Austausch verursacht werden, etabliert sich nach einiger Zeit ein stationärer Zustand. Bei Transportprozessen wird experimentell oft eine lineare Antwort gefunden: Sind die Störungen klein genug, bildet das System entlang der Austauschachse (*z*-Achse) einen linearen Gradienten in der ausgetauschten Größe aus. Dieser Gradient ist dann proportional zum Fluss, wobei der Proportionalitätsfaktor je nach Simulationsart die Scherviskosität η resp. die Wärmeleitfähigkeit κ des Systems darstellt.

Für die Scherviskosität:

$$j_z(p_x) = -\eta \frac{\partial v_x}{\partial z} \tag{3}$$

Für die Wärmeleitfähigkeit:

$$j_z(Q) = -\kappa \frac{\partial T}{\partial z} \tag{4}$$

Da der induzierte Fluss während des Austausches exakt berechnet wird, muss zur Bestimmung der Stoffkonstanten nur noch der Gradient aus den Simulationsergebnissen ermittelt werden, um über Gleichungen 3 und 4 die Viskosität, respektive die Wärmeleitfähigkeit zu berechnen.

2.3. Anwendungen

Der RNEMD Algorithmus wurde 1997 von F. Müller-Plathe mit einem Lennard-Jones-System eingeführt [5]. Seitdem wurde die Methode in mehreren Phasen auf immer neue Arten von Untersuchungen und physikalisch-chemischen Systemen ausgeweitet. Tabelle 1 bietet einen Überblick über die Entwicklung der Methode im letzten Jahrzehnt.

Nachdem RNEMD zunächst für die Wärmeleitfähigkeit einfacher Lennard-Jones-Flüssigkeiten eingeführt wurde [5], fand die Adaption für molekulare Flüssigkeiten bald mehrfach Anwendung [7,8]. Im Laufe der letzen Jahre wurden die betrachteten Systeme immer komplexer. Zu diesen gehören amorphe Polymere [9-12], Polymerkristalle [13] und Kohlenstoff-Nanoröhren [14]. Zur Zeit wird die Gleichrichtung der Wärmeleitung in Nanoröhren untersucht [15].

Nachdem 1999 eine Übereinstimmung der mittels RNEMD berechneten Scherviskositäten von Lennard-Jones-Flüssigkeiten nahe des Tripelpunktes mit den Ergebnissen anderer Methoden gezeigt wurde [16], fand RNEMD alsbald Anwendung bei molekularen Flüssigkeiten [17], Polystyrol als Modellpolymer [18] und der ionischen Flüssigkeit 1-n-Butyl-2-Methylimidazolium Hexafluorophosphat [19]. Eine der hier präsentierten Arbeiten fügt der Liste die Scherviskosität von Membranen [20] an.

Auch wenn der unter dem Namen Ludwig-Soret-Effekt bekannte, durch einen Temperaturgradient verursachte Massentransport in dieser Arbeit keine Rolle spielt, so sei hier der Vollständigkeit halber dennoch erwähnt, dass die RNEMD Methode auch zur Erklärung und zur Berechnung von Soret-Koeffizienten eingesetzt wurde. Auch hier bildeten binäre Lennard-Jones-Flüssigkeiten die Grundlage [21,22], welche alsbald auch bei Benzol/Cyclohexan-Mischungen [23], Heptan/Benzol-Mischungen [24], sphärischen Molekülen [25] und an verdünnten Polymerlösungen [26] angewendet wurde.

Neben den oben erwähnten Anwendungen finden sich in der Literatur auch immer wieder technische Untersuchungen und Erweiterungen der RNEMD Methode. Darunter fallen nicht nur neue Implementierungen, so wie diejenige in GMQ [27], sondern auch komplett neue Ansätze wie derjenige der Nutzung von thermischem Rauschen als Wärmequelle [28, 29].

Tabelle 1: Evolution der RNEMD Methode und ihrer Anwendungen

Jahr	Neuerung	Anwendungsbereich	System	Referenz
1997	Einführung der RNEMD Methode	Wärmeleitfähigkeit	Lennard-Jones	5
1999	Adaption der RNEMD für Scherviskosität	Scherviskosität	Lennard-Jones	16
2000	Adaption für Soret-Ludwig-Effekt	Thermodiffusion	Lennard-Jones	20,21
2002	Einführung von fixierten Bindunglängen	Scherviskosität	kleine Moleküle	17
2005	Neue Methode: Rauschen als Wärmequelle	Wärmeleitfähigkeit	Wasser	28,29
	Anwendung auf kleine Moleküle	Wärmeleitfähigkeit	kleine Moleküle	8
	Erste Wärmediffusionsanwendung	Thermodiffusion	Benzol/ Cyclohexan	23
2006	Soret-Effekt in verdünnter Polymerlösung	Thermodiffusion	generisches Polymer	26
2007	Anwendung: amorphes Polymer	Wärmeleitfähigkeit	Polyamid-6,6	9,10
	Anwendung: sphärische Moleküle	Thermodiffusion	kleine Moleküle	25
	Anwendung: Scherung an Polymeren	Scherviskosität	Polystyrol	18
2008	Scherung von ionischen Flüssigkeiten	Scherviskosität	[bmim][PF$_6$]	19
	Technische Studie zu Manostaten	Scherviskosität	kleine Moleküle	30
	Weitere Wärmediffusionsanwendung	Thermodiffusion	Heptan/Benzol	24
2009	Wärmetransport in Röhren	Wärmeleitfähigkeit	Nanoröhren	14
	Wärmetransport in Polymerkristallen	Wärmeleitfähigkeit	Polystyrol	13
	Scherviskosität von Biomembranen	Scherviskosität	DPPC	20

2.4. Methodische Aspekte

So genial einfach der RNEMD Mechanismus auch ist, die Umsetzung der Methode birgt ihre Tücken. Einige davon, sowie mögliche Verallgemeinerungen zum RNEMD Algorithmus sind in der folgenden Auflistung zusammengefasst:

Äquilibrierte MD Systeme: Oftmals wird die RNEMD Methode angewendet, nachdem ein System bereits mit herkömmlicher Molekulardynamik untersucht wurde. In diesem Fall bietet es sich an, das bereits mit MD äquilibrierte System einfach mehrmals in z-Richtung aneinander zu fügen, um eine Ausgangskonfiguration zu erhalten, die sich schon nahe dem Gleichgewicht befindet. In solchen Fällen verkürzt sich die Äquilibrierungsdauer vor allem bei nur langsam relaxierenden Systemen entscheidend.

Grösse der Simulationsbox: Auch wenn physisch mit einzelnen Partikeln in einer beschränkten Box gerechnet wird, so sorgen periodische Randbedingungen in alle Raumrichtungen für ein virtuell unendliches System. Die dadurch garantierte Abwesenheit von Oberflächeneffekten ist eine der Voraussetzungen für die RNEMD. Wird die Box jedoch zu klein gewählt, so verliert diese virtuelle Unendlichkeit ihre Unabhängigkeit und es treten analog zu herkömmlichen MD Simulationen finite Grösseneffekte auf, welche die Resultate von RNEMD Simulationen beeinflussen.

Austausch von Schwerpunktsgeschwindigkeiten: Da der Algorithmus auch für Berechnungen mit Schwerpunkten gültig ist, können auch Atomgruppen zusammengefasst und die Methode dann statt auf die einzelnen Atome auf die Schwerpunkte angewendet werden. Das bietet sich z.B. bei molekularen Flüssigkeiten an.

2.5. Vor- und Nachteile gegenüber anderen Rechenverfahren

Wie schon der Name der RNEMD verrät, kehrt diese Methode das Ursache-Wirkungs-Prinzip der Experimente und herkömmlicher Nichtgleichgewichts-Simulationsansätze um. Solche Methoden (z.B. sliding bricks Simulationen für Viskositäten, etc.) etablieren zunächst einen Gradienten im System und versuchen dann, den dadurch verursachten Fluss zu messen. RNEMD wiederum induziert einen wohldefinierten Fluss und misst den daraus resultierenden Gradienten. Neben ihrer einfachen Implementierung und Analyse konvergiert RNEMD sehr schnell, was vor allem bei Gleichgewichtsmethoden nicht der Fall ist. Auch sind die gemessenen Gradienten um vieles robuster als die berechneten Flüsse anderer Methoden.

Zusätzlich bietet RNEMD vom physikalischen Standpunkt her eine Besonderheit. RNEMD erhält die Gesamtenergie und den Gesamtimpuls des Systems und braucht daher per se keine Thermostaten. Dadurch ist die Methode nicht nur für Programme mit Newton'scher Mechanik anwendbar, sondern auch in anderen, die lokale Energie und Impuls erhalten (Dissipative Particle Dynamics, etc).

In Berechnungen der Wärmeleitfähigkeit ist das Ermitteln des nur makroskopisch wohl definierten Wärmeflusses in herkömmlichen NEMD oder Gleichgewichtssimulationen nicht eindeutig. Der Temperaturgradient führt auch zu einem Dichtegradienten. Ist deswegen nun der Fluss der Energie oder der Fluss der Enthalpie zu betrachten? Wie definiert man lokal eine mikroskopische Enthalpie? Der Vorteil der RNEMD liegt nun darin, dass der Nettowärmefluss durch den Austauschschritt klar definiert ist und man sich nicht darum zu kümmern hat, auf welche Art und Weise die Wärme genau durch das System fliesst.

Der grösste Nachteil der Methode ist, dass sie durch die Umkehr von Ursache und Wirkung nicht das experimentelle Geschehen widerspiegelt. Dies erlaubt nur einen Vergleich der finalen Transportkoeffizienten, führt aber dazu, dass aufbauspezifische Probleme (z.B. im Falle der

Scherviskosität, das Fliessverhalten nahe der Scherplatten) bis vor kurzem nicht mir RNEMD nicht behandelt wurden [31].

Eine weitere Einschränkung der RNEMD Methode besteht darin, dass sie eine lineare Antwort des Systems voraussetzt. Wird eine zu grosse Scherung angelegt, so verliert der Gradient seine lineare Form, wodurch die Voraussetzungen der hier vorgestellte Theorie nicht mehr gültig sind. Zu kleine Scherung wiederum resultiert in einem sehr flachen Gradienten, der durch statistische Fehler stark verrauscht werden kann. Dadurch werden für immer kleinere Scherraten stark zunehmende Simulationdauern nötig. Insofern ist der Anwendungsbereich der Methode bezüglich Scherung sowohl nach oben als auch nach unten beschränkt. Diese Eigenschaft teilt sie mit allen anderen NEMD-Verfahren.

So elegant die Methode des Austausches auch ist, so führt die Anforderung, dass sich im stationären Zustand der Fluss und der unphysiklische Transfer gegenseitig ausgleichen, zu einer ersten Beschränkung der Allgemeinheit der Methode auf den Transport von Erhaltungsgrössen. Beispielsweise ist die Berechnung der Rotationsviskosität von nematischen Flüssigkristallen mittels Austausch von Direktoren nicht möglich. Des weiteren wäre es zwar prinzipiell denkbar, Massentransport (Diffusion) oder Ionentransport (ionische Leitfähigkeit) auf diese Weise zu untersuchen. Da der Austausch von Partikeln/Partikeleigenschaften aber die Bedingung der Energieerhaltung verletzt, sind auch solche Untersuchungen nicht praktikabel.

2.6. Eigenschaften und Beweise: Der Fluss durch eine Scheibe

Der Fluss resultiert aus einem periodischen Austausch von Impuls p (bei Scherviskosität) oder kinetischer Energie E_{kin} (bei Wärmeleitfähigkeit) zwischen der ersten und der mittleren Scheibe. Die eine Scheibe (Maximumscheibe) akkumuliert dadurch Impuls resp. kinetische Energie während die andere (Minimumscheibe) negativen Impuls akkumuliert resp. kinetische Energie verliert. Der in einer Simulation insgesamt durch den Austausch im System verschobene Impuls errechnet sich über die Summe sämtlicher Austausche. Analoges gilt auch für die kinetische Energie:

$$p_{x,tot} = \sum_{Austausche} \left(p_{x,mitte} - p_{x,erste} \right) \tag{5}$$

$$E_{kin,tot} = \sum_{Austausche} \left(E_{kin,mitte} - E_{kin,erste} \right) \tag{6}$$

Fluss j ist allgemein definiert als der Transport der Menge X einer Grösse durch eine Fläche pro Zeit t. In dem vorliegenden Fall ist dies die auf der z-Achse senkrecht stehende Seitenfläche der Simulationsbox, welche durch die beiden Seitenlängen L_x und L_y aufgespannt wird:

$$j = \frac{X}{tL_x L_y} \tag{7}$$

Der durch den Austausch im System induzierte Gesamtfluss lässt sich durch Einsetzen des gesamten ausgetauschen Impulses ($X=p_{x,tot}$), resp. der gesamten ausgetauschten kinetischen Energie ($X=E_{kin,tot}$) in Gleichung (7) berechnen.

Gesamter Impulsfluss bei der Scherviskosität:

$$j_{Austausch}(p_x) = \sum_{Austausche} \frac{p_{x,mitte} - p_{x,erste}}{tL_x L_y} \tag{8}$$

Beim Austausch der kinetischen Energien wird ein Wärmefluss generiert, der die künstlich durch den Austausschritt transportierte Wärmemenge durch verschiedenste physikalische Mechanismen wieder durch das System zur kalten Scheibe zurückfliessen lässt. Die dabei zu transportierende Wärmemenge Q entspricht dabei der zur ausgetauschten kinetischen Energie ($Q = E_{kin,mitte} - E_{kin,erste}$).

Gesamter Wärmefluss bei der Wärmeleitfähigkeit:

$$j_{Austausch}(Q) = \sum_{Austausche} \frac{E_{kin,mitte} - E_{kin,erste}}{tL_x L_y} \tag{9}$$

Aufgrund der periodischen Randbedingungen der Simulation fliesst die während des Austausches von der Minimumscheibe zur Maximumschreibe transportierte Menge an Impuls oder kinetischer Energie (der Gesamtfluss $j_{Austausch}$) entlang z zu gleichen Teilen j_z sowohl nach links $j_{z,links}$ als auch nach rechts $j_{z,rechts}$ ($-j_{z,links} = j_{z,rechts} = j_z$) ab.

$$j_{Austausch} = j_{z,rechts} - j_{z,links} = 2 j_z \tag{10}$$

NB: Die Tatsache, dass der Fluss nach links und nach rechts gleich ist, erlaubt in der Analyse der Simulationsergebnisse eine Mittelung der Profile, wobei zur Korrektur des negativen Vorzeichens des Flusses das Profil gespiegelt wird.

Das Auflösen von Gleichung (10) nach dem in der Simulation effektiv beobachteten Fluss j_z durch eine der Scheiben und das anschliessende Einsetzen in Gleichung (5) führt zu den in Kapitel 3.2 angebenen Gleichungen (1) und (2).

Q.E.D

3. Vorbereitende Arbeiten:

Seit der Einführung der „reverse non-equilibrium molecur dynamics“ (RNEMD) Methode [5] wurden unterschiedliche Transporteingeschaften verschiedenster Systeme damit berechnet. Dazu gehören Berechnungen von Scherviskositäten von kleinen Molekülen und Polymeren [16-18] sowie die Bestimmung von Wärmeleitkoeffizienten in Flüssigkeiten oder Polymermatrizes [7-15]. Auch zur Untersuchung des Soret-Koeffizienten ist RNEMD eine elegante Methode [21-26].

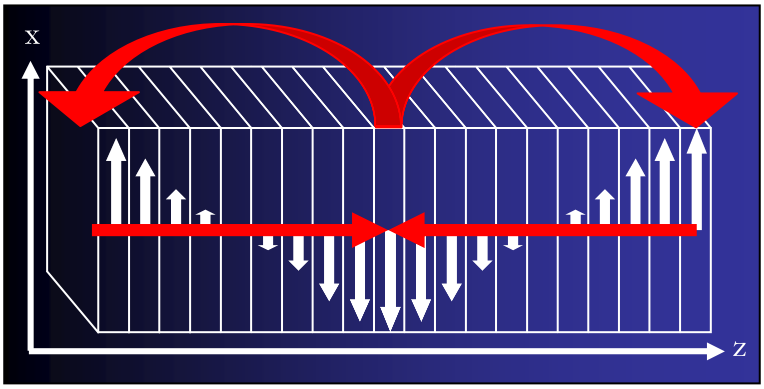

Abb. 2: Die Flüsse bei der RNEMD Methode: Durch einen erzwungenen, genau kontrollierbaren Austausch bringt man das System aus dem Gleichgewicht (geschwungene Pfeile). Dadurch entsteht ein Rückfluss der ausgetauschten Grösse entlang eines Gradienten (weisse Pfeile).

Der im Gegensatz zu anderen Methoden den Energieerhaltungssatz erfüllende Algorithmus unterteilt die periodische Simulationsbox entlang einer ausgewählten Raumrichtung (in unserem Falle z) in virtuelle Scheiben. In eine rechtwinklig dazu gewählte Richtung (in diesem Falle x) wird in einem konstanten Zeitintervall Impuls von einer bestimmten Scheibe zu der eine halbe Simulationsbox entfernten Scheibe übertragen. Dadurch wird die eine Scheibe in die entgegengesetzte Richtung der anderen bewegt und es entsteht Scherung. Damit wird aber ein Ungleichgewicht aufgebaut, welches das System mit einem Rückfluss des transportierten Impulses ausgleicht. In der Box entsteht ein Geschwindigkeitsgradient, der im Fall der Linearen-Antwort-Theorie proportional zum ausgetauschten Impuls ist. Der Proportionalitätsfaktor ist die Scherviskosität des Systems.

In der eleganten Einfachheit der Methode liegen aber viele Anforderungen, welche Computersimulationen nicht unbedingt erfüllen können. So verlangt die Methode strikt nach einem System mit konstanter Teilchenzahl, konstantem Volumen und konstanter Energie. Während die erste Bedingung in konventionellen Molekularsimulationen nur selten verletzt wird, so ist das für die beiden anderen Zustandsgrössen nicht unbedingt der Fall. So können Systeme, die sich aufgrund von numerischen Rundungsfehlern aufheizen, mittels eines Thermostaten bei konstanter Temperatur gehalten werden, wohingegen dann ein konstant Halten der Energie nicht möglich ist. Ebenso gibt es dynamische Systeme (nicht zuletzt die von mir untersuchten Biomembranen), die räumliche Fluktuationen aufweisen, die mit einem fixen Boxvolumen ihrer Freiheitsgrade beraubt würden.

Patrice Bordat hatte bereits gezeigt, dass ein Thermostat – obwohl die Anforderung der Energie- und Impulserhaltung verletztend – auf die Resultate von Scherviskositätsrechungen keinen erkennbaren Einfluss hat [17]. Analog dazu beschäftigte ich mich in den vorbereitenden Arbeiten zu meiner Dissertation mit der Frage, ob das zusätzliche Anwenden eines Manostaten, um statt dem Volumen den Druck konstant zu halten, einen erkennbaren Einfluss auf die Resultate von Scherviskositätsberechnungen hat.

Auch wenn diese Fragestellung für die Simulationen der Biomembranen von zentraler Bedeutung war, so wurde der Effekt an einfachen niedermolekularen Gasen und Flüssigkeiten studiert, um lange Äquilibrierungszeiten und den Einfluss von komplexen Interaktionen schon im Vorfeld auszuschliessen.

In der vorliegenden Publikation (J. Chem. Phys. 129 (2008) 014102) fasse ich zusammen, aufgrund welcher Ergebnisse wir zu dem Schluss kamen, dass auch (wie schon bei Thermostaten) der Einsatz von Manostaten die Resultate von Scherviskositätsberechnungen nur unwesentlich beeinflusst.

The influence of thermostats and manostats on reverse nonequilibrium molecular dynamics calculations of fluid viscosities

Thomas J. Müller,[a] Michael Al-Samman, and Florian Müller-Plathe
Theoretische Physikalische Chemie, Eduard-Zintl-Institut für Anorganische und Physikalische Chemie,
Technische Universität, Petersenstrasse 20, 64287 Darmstadt, Germany

(Received 29 February 2008; accepted 21 May 2008; published online 1 July 2008)

Reverse nonequilibrium molecular dynamics to calculate the shear viscosity of Lennard-Jones liquids was extended to simulations at constant number of particles, constant volume, and constant pressure using a Berendsen thermostat and a Berendsen manostat. Using additional systems such as water and hexane, we also report on the performance of shear viscosity calculations of systems with electrostatic and nontrivial intramolecular interactions when a manostat is applied. We compare the shear viscosities of simulations using no coupling, only temperature coupling, and temperature and pressure coupling and characterize discrepancies, where observed. From this, we deduce guidelines for when and how manostats can be usefully applied in reverse nonequilibrium simulations. © *2008 American Institute of Physics*. [DOI: 10.1063/1.2943312]

I. INTRODUCTION

To investigate shear viscosity, several techniques have been invented. The reverse nonequilibrium dynamics[1] (RNEMD) is one algorithm in the evolving chain of these techniques belonging to the class of nonequilibrium molecular dynamics (NEMD) techniques. Equilibrium molecular dynamics (EMD) techniques which rely on the calculation of time correlation functions by measuring near equilibrium fluctuations of the fluid properties (Green–Kubo methods[2–4]) or on the accumulation of displacement properties of the fluid over time (Einstein methods[2–4]) tend to require long simulations to get an acceptable level of error, while RNEMD, as the other nonequilibrium techniques, measures a macroscopic steady-state response of the system to a perturbing field which leads to robust and rapidly converging raw data.[1] The results of RNEMD and MD calculations differ as well. While EMD techniques calculate the zero-shear viscosity, RNEMD (and the other NEMD schemes) calculates shear field dependent shear viscosities. Although there is no generally accepted relation between zero-shear viscosity and non-zero-shear viscosity, NEMD can converge to zero-shear viscosities by reducing the shear field at the expense of slowed down convergence of raw data and thus longer simulation times.

In the class of NEMD simulations, there are a few properties of the RNEMD simulations to stress out, which make it unique. The RNEMD is "reversed" in the sense that cause and effect are reversed in comparison to general NEMD simulations: The flux is imposed and the corresponding field is measured.[1] This is advantageous if the flux is difficult to define microscopically or is slowly converging.

The beauty of this algorithm is its simple implementation. No specific thermostats (for example, in the transient-time correlation function[5,6]) or additional energy sinks (for example, in the momentum impulse relaxation method[7]) are required. Even more, RNEMD is designed to conserve the total energy and the total linear momentum, which allows calculations in a microcanonical ensemble—without thermostats. This is another advantage of RNEMD over most of other NEMD simulation techniques which essentially require a thermostat. The fact that for technical issues (such as heating of the system due to truncation errors) a thermostat or even a manostat might be necessary is the motivation to this work.

Since the introduction of the RNEMD method,[8] it has been applied to many systems for the calculation of shear viscosities,[9,10] thermal conductivities,[11–13] and related properties, such as Soret coefficients.[14–16] Viscosities have been calculated for simple liquids, molecular liquids,[9] and polymer melts.[17,18] Most of these simulations were performed in the canonical ensemble with constant number of particles, constant volume, and constant temperature (*NVT*). Although RNEMD can be performed in the microcanonical ensemble with constant number of particles, constant volume, and constant energy (*NVE*), it has been shown that a thermostat has only a minor influence on the shear viscosity.[9] At the beginning of the present work, test simulations had indicated that the influence of a manostat may be more severe. However, this has never been the subject of a detailed investigation.

Since several, especially inhomogeneous, systems require simulations in an isothermal and isobaric ensemble (*NPT*), the investigation of the impact of manostats for pressure coupling became an important practical point for further research on shear viscosity using the RNEMD technique. The purpose of the present contribution is to establish if and under which conditions the RNEMD method for viscosities may be used in connection with a manostat.

II. METHOD

All simulations were performed with the molecular dynamics simulation package YASP,[19,20] in which the RNEMD method has been implemented and tested for the shear vis-

---

[a] Electronic mail: t.mueller@theo.chemie.tu-darmstadt.de.

TABLE I. Force field parameters of the simulated fluids.

	Argon	Water	Hexane
Mass (g/mol)	$m_{\mathrm{Ar}}=39.95$	$m_{\mathrm{O}}=15.9949$ $m_{\mathrm{H}}=1.007\,825$	$m_{\mathrm{CH_3}}=15.023\,475$ $m_{\mathrm{CH_2}}=14.01\,565$
ε (kJ/mol)[a]	$\varepsilon_{\mathrm{Ar}}=0.996\,07$	$\varepsilon_{\mathrm{O}}=0.650\,17$ $\varepsilon_{\mathrm{H}}=0.0$	$\varepsilon_{\mathrm{CH_3}}=0.864\,687\,2$ $\varepsilon_{\mathrm{CH_2}}=0.480\,794\,94$
σ (nm)[a]	$\sigma_{\mathrm{Ar}}=0.340$	$\sigma_{\mathrm{O}}=0.3166$ $\sigma_{\mathrm{H}}=0.0$	$\sigma_{\mathrm{CH_3}}=0.391$ $\sigma_{\mathrm{CH_2}}=0.393$
Partial charge (e)[a]	$\sigma_{\mathrm{Ar}}=0$	$q_{\mathrm{O}}=-0.8476$ $q_{\mathrm{H}}=0.4238$	$q_{\mathrm{CH_3}}=0$ $q_{\mathrm{CH_2}}=0$
Bond length (nm)	⋯	$b_{\mathrm{OH}}=0.1$	$b_{\mathrm{CH}_x\text{-}\mathrm{CH}_x}=0.154$[b]
Angle (deg)	⋯	$a_{\mathrm{HOH}}=109.47$	$a_{\mathrm{CH}_x\text{-}\mathrm{CH}_x\text{-}\mathrm{CH}_x}=114$[b]
k_{angle} (kJ mol^{-1} rad^{-2})	⋯	⋯	$k_{\mathrm{CH}_x\text{-}\mathrm{CH}_x\text{-}\mathrm{CH}_x}=508.937$[b]
Multiplicity m,[c] phase shift τ (deg), k_{torsion} (kJ mol^{-1})	⋯	⋯	$m=1,\ \tau=180,\ k=9.8$ $m=2,\ \tau=180,\ k=6.6$ $m=3,\ \tau=180,\ k=10.6$
Reaction-field dielectric constant	⋯	72	⋯

[a] Intramolecular 1–2 and 1–3 interactions have been totally omitted. In the hexan model, 1–4 interaction have been modified: CH_2-CH_3 Lennard-Jones interactions were set to 0.8737 for ε and to 0.343 for σ, while CH_3-CH_3 Lennard-Jones interactions were set to 0.7843 for ε and to 0.343 for σ.

[b] CH_x may be CH_2 or CH_3.

[c] This set for parameters has been applied to all torsions.

cosity of molecular fluids.[9] In the linear response approximation, the shear viscosity η is defined as the proportionality constant between the imposed flux of transverse momentum $j_z(p_x)$ and the calculated transverse velocity gradient $(\partial v_x/\partial z)$[21]

$$j_z(p_x) = -\eta\left(\frac{\partial v_x}{\partial z}\right). \tag{1}$$

The details of the RNEMD method can be found in Ref. 22.

MD simulations at constant temperature or at constant pressure can be performed using Berendsen's thermostat[23] or manostat. The temperature and the pressure are coupled in first order to an external bath

$$\frac{dT}{dt} = \frac{1}{\tau_T}(T_{\mathrm{bath}} - T), \tag{2}$$

$$\frac{dP}{dt} = \frac{1}{\tau_P}(P_{\mathrm{bath}} - P). \tag{3}$$

Hereby, the temperature T and the pressure P of the system relax in time t towards a target temperature T_{bath} and the target pressure P_{bath}, while the time constants τ_T and τ_P determine how fast the system reacts to deviations from the bath values. Constant temperature is implemented by uniform scaling of the atomic velocities, whereas constant pressure is achieved by scaling uniformly the atom positions and the lengths of the simulated box.

The Berendsen method has in the past met with criticism because it cannot be shown unambiguously to generate strictly canonical distributions in EMD simulations.[24] We still investigate it here not only because of its robustness, which has been proven in many applications of MD to biological or materials problems. It has also been argued that the Berendsen thermostat may have advantages over other methods in the context of nonequilibrium simulations of viscous flow:[25] Most of the common thermostats and manostats are not momentum conserving. Among them, the Berendsen method shows a relatively mild form of nonconservation and is therefore advantageous in the calculation of the viscosity, the property that governs the transport of linear momentum.

III. COMPUTATIONAL DETAILS

For the sake of diversity, three different fluid systems have been simulated: Argon, water, and n-hexane. The force field parameters for these systems were the same as used by Bordat and Müller-Plathe.[9] They can be found in Table I.

As in previous RNEMD simulations, the orthorhombic periodic simulation box was taken three times as long in the z direction ($3L$) as the box size L in x and y. It was divided into 20 slabs along the z axis. The transverse momentum flux was imposed by periodically exchanging the v_x components of the center-of-mass velocities of suitably chosen molecules in slabs 1 and 11 (molecular exchange). The local transverse flow velocity v_x was calculated as the average x component of the velocities of all atoms in each slab. The gradient of v_x in the z direction [Eq. (1)] was determined by a linear least-squares fit, with the exchange slabs excluded. The period between two velocity exchanges w varied between 3 MD time steps and 1200 time steps. The applied perturbation is proportional to $w\Delta t$. This is described in detail in previous contributions.[8] The values of w are given below for each simulated system.

As implemented in YASP, pressure control is handled by a Berendsen manostat and temperature is controlled by a Berendsen thermostat. The coupling times used are reported below for each system.

A. Simulations with constant coupling conditions: Influence of the exchange period

All three systems start from a configuration with the molecules equally distributed on a grid within the simulation box. In the first stage they have been equilibrated under constant-temperature conditions, until the total energy reached a constant value and was fluctuating by less than 2%. For simulations with constant temperature and pressure, an additional equilibration was performed until the density reached a constant value and was fluctuating by less than 5%.

For all systems, three types of RNEMD simulations were performed. During simulations with constant number of particles, volume, and energy (*NVE*), no thermostat or manostat was applied. During simulations with constant particle number, volume, and temperature (*NVT*), the Berendsen thermostat was applied. While the target temperature varied for different fluids, the coupling time τ_T remained 0.2 ps for all simulations. In simulations with constant particle number, pressure, and temperature (*NPT*), both thermostat and manostat were used. In these simulations the target pressure of 101.3 kPa was maintained by a pressure coupling time τ_P of 0.5 ps.

The output interval for the RNEMD system properties [transverse momentum flux $j_z(p_x)$, velocity gradient (dv_x/dz), and shear viscosity η] and the velocity profiles (mean flow velocity in the x direction $\langle v_x \rangle$, temperature, and density) was always chosen to be 101 time steps.

Argon. 2592 atoms were distributed in a box $(L \times L \times 3L)$ with $L=3.424\,99$ nm leading to a density of 1426.621 kg/m^3. For all argon simulations, the time step was $\Delta t=5$ fs, the cutoff radius was 1.0251 nm, and the neighbor list with a cutoff of 1.2 nm was updated every 15 time steps. The equilibration of the system at 86.5 K with a coupling time of $\tau_T=0.2$ ps ran for 5×10^5 time steps (2.5 ns). After this, the RNEMD simulations under *NVE*, *NVT*, and *NPT* conditions ($\tau_T=0.2$ ps, $\tau_P=0.5$ ps) were performed for 5×10^5 time steps (2.5 ns) at exchange periods w of 3, 15, 60, 300, and 1200 time steps (corresponding to time intervals between the exchanges of 0.015, 0.075, 0.3, 1.5, and 6 ps). For *NPT* conditions, additional simulations have been performed at $w=200$ and $w=400$ time steps. The first 50 000 time steps (100 ps) which were in all simulations enough to reach steady-state flux, temperature, and density were considered necessary to reach the steady state and were not analyzed.

Water. The 1535 water molecules were distributed in the box $(L \times L \times 3L)$ with $L=2.479\,11$ nm leading to a density of 1005 kg/m^3. Water was described by the extended simple point charge (SPC/E) model.[26] In all simulations, the time step was 2 fs and the cutoff radius was 1.0 nm. The neighbor list with a cutoff of 1.2 nm was updated every 15 time steps. The equilibration at 300 K with a coupling time of $\tau_T=0.2$ ran for 10^5 time steps (200 ps). This calculation was followed by RNEMD simulations under *NVE*, *NVT*, and *NPT* conditions ($\tau_T=0.2$ ps, $\tau_P=0.5$ ps) of 5×10^5 time steps (1 ns) at exchange periods of 20, 100, 250, 500, and 1000 time steps (corresponding to time intervals of 0.04, 0.2, 0.5, 1, and 2 ps). The first 50 000 time steps (100 ps) were considered necessary to reach the steady state (monitored by flux, temperature, and average density) and were not analyzed.

Water is the only one of the three molecules with atomic partial charges. The resulting electrostatic interactions were treated by an atom-based cutoff (1.0 nm) together with a reaction-field correction with a reaction-field dielectric constant of 72. For details see Ref. 19.

n-hexane. The 324 molecules consisted of altogether 1944 united CH_2 and CH_3 atoms. They were distributed in a box $(L \times L \times 3L)$ with $L=2.8044$ nm leading to a density of 700 kg/m^3. In all hexane simulations, the time step was 2 fs, the cutoff radius was 1.0 nm, and the neighbor list with the cutoff of 1.12 nm was updated every 15 time steps. For comparability the cutoff was chosen to match the model of Ref. 9. Preliminary results in *NPT* and *NVT* simulations showed that enlarging the cutoff radius to 1.3 nm yields shear viscosities differing from the ones obtained using a cutoff of 1.0 nm by less than 2.5%.

The equilibration of the system at 311 K (as chosen in Ref. 9) with a coupling time of $\tau_T=0.2$ ps ran for 10^5 time steps (200 ps). Then, RNEMD simulations under *NVE*, *NVT*, and *NPT* conditions ($\tau_T=0.2$ ps, $\tau_P=0.5$ ps) were performed for 5×10^5 time steps (1 ns) at exchange periods of 5, 100, 1000, and 3000 time steps (corresponding to time intervals of 0.01, 0.2, 2, and 6 ps). The first 50 000 time steps (100 ps) were considered necessary to reach the steady state and were not analyzed.

B. Simulations with different coupling constants τ_P and τ_T: Influence of thermostat and manostat

Studies of the influence of different temperature and pressure coupling times have been performed for SPC/E water and n-hexane.

SPC/E water. For the RNEMD calculations with exchange periods w of 3, 15, 60, 300, and 1200 time steps, additional simulations were performed. Two changes were made: While the target values for temperature (300 K) and pressure (101.3 kPa) remained, the coupling times τ_T and τ_P were changed to 1 ps for the thermostat (*NVT* and *NPT* conditions) and to 5 ps for the manostat (*NPT*).

The starting point for these simulations was the output of the simulations with the original coupling times ($\tau_T=0.2$ ps for *NVT*, respectively, $\tau_T=0.2$ ps and $\tau_P=0.5$ ps for *NPT*). The first 5×10^4 time steps (100 ps) were considered necessary to reach the steady state and were not analyzed.

n-hexane. A set of additional simulations was performed with different temperature coupling times. The simulation parameters were the same as in the simulation under *NVT* conditions at an exchange period w of 1000 time steps. The number of time steps was increased to 2 000 000 resulting in a total simulated time of 4 ns for each run. While keeping the same target temperature (311 K), the coupling time for the thermostat τ_T has been taken as 0.05, 0.1, 0.2, 0.5, 1, and 2 ps.

The starting point for the additional RNEMD simula-

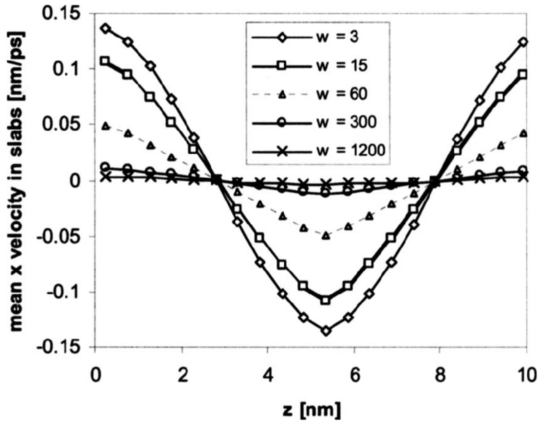

FIG. 1. Velocity profiles of argon at different exchange intervals *w* (number of time steps of length of 5 fs between velocity exchanges). This example was taken from calculations at constant volume and constant temperature with $T_{\text{targ}}=86.5$ K and $\tau_T=0.2$ ps.

tions was the output of the simulations without varying the coupling times (i.e., $\tau_T=0.2$ ps). The first 5×10^4 time steps were not included in the analysis.

C. Evaluation of shear viscosities and error bars

In all simulations, the average flow velocity $\langle v_x\rangle$ of each slab is stored every 101 time steps. Averaging the velocities leads to velocity profiles such as reported in Fig. 1. The error bars correspond to the standard deviations of the calculated mean values of the flow velocities. Excluding velocities of the exchange slabs 1 and 11 (which might contain artifacts of the exchange algorithm), the remaining velocities have to be symmetrical with respect to slab 11 (since the setup of the algorithm is periodic along the *z* axis). Each two symmetric values have been averaged again. An error-weighted linear regression calculates the slope of the gradient and its standard error.

For exchange periods $w=3$ and $w=15$, one identifies a nonlinear response of the system to the imposed field. This effect indicates shear thinning near the positions where the field is imposed. Applying Eq. (1) will lead only to rough estimates rather than trustable values in the limit of linear response theory. The shear viscosities from nonlinear regimes will be shown in the plot of this paper but will be neglected in the final results.

To calculate the momentum flux $J=j_z(p_x)$ in the system, we use the fact that in steady state it has to be proportional to the exchange rate. Therefore we observe the cumulative exchanged momentum $p_{x,\text{acc}}$ (known from the exchange steps) divided by the area perpendicular to the flux A_{xy} (*xy* plane with dimensions $L\times L$ in these simulations) with respect to time

$$\frac{p_{x,\text{acc}}(t)}{2A_{xy}}=Jt. \tag{4}$$

A linear regression through the points $(p_{x,\text{acc}}/A_{xy},t)$ leads to the reported values for the flux (slope of the interpolated line) and its error (the standard deviation of the linear regression).

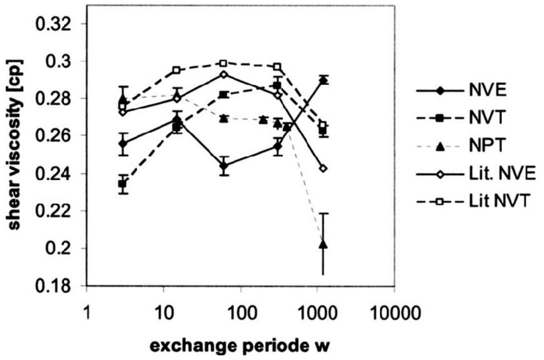

FIG. 2. Shear viscosity of argon: Comparison between the result of our simulations and the reported ones from Bordat and Müller-Plathe (Ref. 9). Where necessary, the thermostat/manostat parametrization was $T_{\text{targ}}=86.5$ K, $p_{\text{targ}}=101.3$ kPa, $\tau_T=0.2$ ps, and $\tau_p=0.5$ ps. The calculated average temperature in each *NVE* run was between 86.0 and 87.4 K.

In the linear response limit, the shear viscosity is the flux $J=j_z(p_x)$ divided by the gradient $G=(dv_x/dz)$. Thus we can estimate its error $\Delta\eta$ by summing the relative errors of the flux and the gradient

$$\Delta\eta=\eta\left(\frac{\Delta J}{J}+\frac{\Delta G}{G}\right). \tag{5}$$

IV. RESULTS AND DISCUSSION

A. Argon

The results for argon under constant *NVE* and under constant *NVT* conditions (Fig. 2) correspond within the error bars to the reported values of Bordat and Müller-Plathe.[9] Similar to these authors, we find a decreased value for the shear viscosities at short exchange periods (in the case of argon, $w=3$ and $w=15$) and at long exchange periods ($w=1200$). The reduction in the shear viscosity at short exchange periods (corresponding to high exchange frequencies and large perturbations) has been attributed to the shear thinning. In contrast, the shear viscosities at small perturbation carry statistical uncertainty since they are derived from a velocity gradient, which is so small that noise influences the results. This statistical uncertainty can be reduced by averaging over longer simulation. For all investigated systems (Ar, H_2O, and hexane) in this work, the two limiting behaviors were also reported by Bordat and Müller-Plathe.[9]

When switching to constant *NPT* conditions, the dependence of the shear viscosity on the exchange period changes. While the absolute values at the intermediate exchange periods of $w=15$, 60, and 300 time steps still correspond within less than 10% to the *NVE* and *NVT* values also for exchange periods smaller than $w=100$, there is a trend of a steadily decreasing shear viscosity with increasing exchange period. The main reason for this lies in the variation in the average density in the system (Fig. 3). Under constant *NPT* conditions, the system adopts at short exchange periods (high shear) a higher average density because of a cooperative packaging effect near the exchange slabs. In fact, for short exchange periods the density profile between the two exchange slabs becomes parabolic. In the extreme case of an

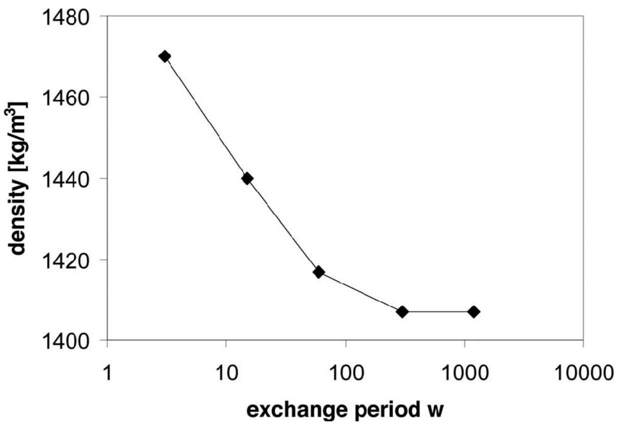

FIG. 3. Variation in the average density in the argon simulations at constant *NPT* conditions. The parameters for the thermostat were $T_{\text{targ}}=86.5$ K and $\tau_T=0.2$ ps while the manostat parameters were $p_{\text{targ}}=101.3$ kPa and $\tau_p=0.5$ ps.

exchange period of 3, the parabola has a minimum value of 1407 kg/m^3, which is the average density of a nonperturbed simulation and a maximum of 1552 kg/m^3 in the exchange slabs. In total, this leads to an increased average density in simulations with high shear. Therefore, at high shear the shear viscosity is systematically higher than it would be if the density remained constant. Under the given conditions, this increase compensates the expected decrease due to shear thinning. Note that the change in the average density is still visible until an exchange period of $w=300$ time steps. Thus, it influences the results at exchange periods where simulations for argon have traditionally been performed.

B. Water

The calculated shear viscosities for *NPT* and *NVT* simulations for the SPC/E water model (Fig. 4) agree to within their error bars with the literature values.[9]

From Fig. 4 it is also evident that *NVE* gives much lower viscosities than either *NVT* or *NPT* for the SPC/E water model. This is different from the case of both argon and *n*-hexane. The effect has nothing to do with the choice of the ensemble *per se*. Rather, treating a partially charged model such as SPC/E by a finite cutoff (albeit with a reaction-field correction) leads to truncation errors, which in turn cause heating of the system with time. In 1 ns of simulation, the water system warms up by 27 K. Correspondingly, the apparent viscosity is lower. To compensate for this drift, we started the simulations below the target temperature, so that the average temperature over the total simulation corresponds to the target temperature.

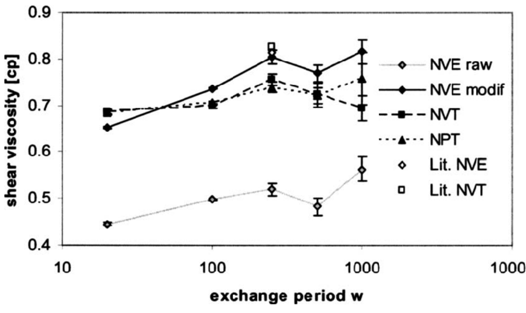

FIG. 4. Shear viscosity of the SPC/E water model: Comparison of the results of our simulations with the ones from the reference of Bordat and Müller-Plathe (Ref. 9) ($T_{\text{targ}}=300$ K, $p_{\text{targ}}=101.3$ kPa, $\tau_T=0.2$ ps, $\tau_P=0.5$ ps). In the case of *NVE* runs, the viscosities labeled "raw" are calculated by starting the simulations at 300 K without controlling the self-heating of the system due to truncation errors. The viscosities labeled "modified" were obtained with simulations starting at lower densities to achieve an average temperature over the whole simulation close to 300 K. 303 K for exchange period $w=20$, 297 K for $w=100$, and 295 K for all other w.

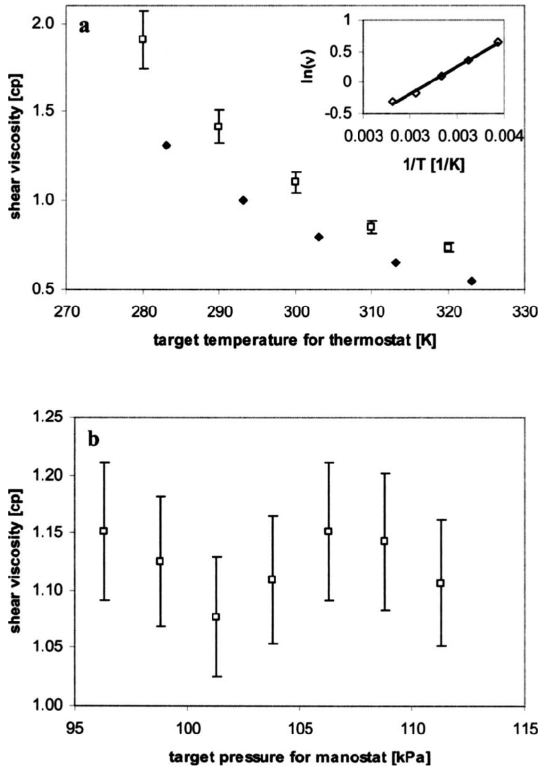

FIG. 5. Dependence of shear viscosities of SPC/E water on deviation in temperature and pressure. (a) The results of *NVT* runs (empty squares) with constant $\tau_T=0.2$ ps show a strong nonlinear dependence of the shear viscosity on the temperature indicating that in *NVE* runs, a small deviation of the temperature from the desired temperature may cause significant changes in the shear viscosity. The same dependence can be also observed in experimental data (filled diamonds). (b) The results of *NPT* runs with constant $T_{\text{targ}}=311$ K, $\tau_T=0.2$ ps, and $\tau_p=0.5$ ps show no significant dependence of the shear viscosity on the pressure in the observed range. Thus if the pressure in *NVT* runs is off by 10%, the shear viscosity remains the same within error bars.

To estimate the systematical error induced by truncation heating, we monitored the shear viscosity of SPC/E water at different temperatures. With this proviso, we are able to estimate the temperature dependence of the shear viscosity [Fig. 5(a)]. Under the given simulation conditions, a deviation of the target temperature from the average temperature by 10% changes the observed shear viscosity by more than 65%. For *NVE* simulation where the temperature drifts, this is a major source of systematical error. From the data also follows an Arrhenius-like behavior with an activation energy of $E_a=-2.18$ kJ/mol. A comparison to $E_a=-1.94$ kJ/mol derived from experimental data[27] is difficult since all the simu-

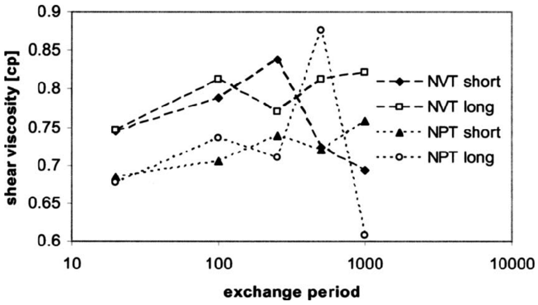

FIG. 6. Dependence of the viscosity of SPC/E water ($T=300$ K, $\rho=1001$ kg/m^3) on the exchange period and the temperature coupling time τ_T and the pressure coupling time τ_p; “short” refers to $\tau_T=0.2$ ps and $\tau_P=1$ ps (*NPT* only); “long” denotes $\tau_T=1$ ps and $\tau_P=5$ ps (*NPT* only).

lations were executed at a constant density of 1005 kg/m^3. From the technical point of view, the nonlinear behavior has an additional consequence for *NVE* runs with a (linear) temperature drift. The observed viscosity is not the one of the average temperature of the run. However, in the range of drift of *NVE* simulations for SPC/E water in this work, this influence is less than the error bar.

The shear viscosity depends much less on the pressure [Fig. 5(b)] than on the temperature, as water is an incompressible liquid, so small pressure changes do not influence the density, which is the determining factor for the viscosity besides the temperature. In fact, pressure fluctuations in the same percentage range ($\pm 10\%$) as for the temperature in Fig. 5(a) are in the order of atmospheric pressure fluctuations so that a significant change in viscosities over this range is not expected.

The value of the viscosity obtained in *NVT* and *NPT* does not seem to depend systematically on the strength of the perturbation, i.e., exchange period w, or the coupling times τ_T and τ_p (Fig. 6). Simulations with $\tau_T=0.2$ ps and $\tau_T=1.0$ ps (*NVT*/*NPT*) and with $\tau_P=1$ ps and $\tau_p=5$ ps (*NPT*) find very similar and small dependencies on w, and *NVT* and *NPT* viscosities show the same deviation from each other.

C. *n*-hexane

Comparing the shear viscosities of our simulations at constant *NVE* and constant *NVT* conditions with the values reported by Bordat and Müller-Plathe[9] shows agreement to within the error bars for exchange periods up to $w=1000$ (Fig. 7). Changing, however, the simulation conditions to constant *NPT* leads to a systematic decrease in the calculated shear viscosity by 30%–40%. The reason for this decrease can be found in a decrease in the density in the simulated system. While simulations under *NVE* and *NVT* conditions have an imposed density of 700 kg/m^3, the density under constant *NPT* conditions drops for all simulations to an equilibrium value of 660 kg/m^3 during the first 100 ps. To undo this 5% density reduction to get back to the density of 700 kg/m^3, we have increased the applied target pressure from 101.3 kPa to 60 000 kPa which is in the same order as the pressure calculated from the *NVE* runs ($p_{w=5}=47$ MPa, $p_{w=100}=54$ MPa, $p_{w=1000}=52$ MPa, and $p_{w=3000}=53$ MPa). Under these conditions the shear viscosity is increased to ≈ 0.43 cP. Thus, the shear viscosity for a given density can be reproduced to within error bars by increasing the pressure.

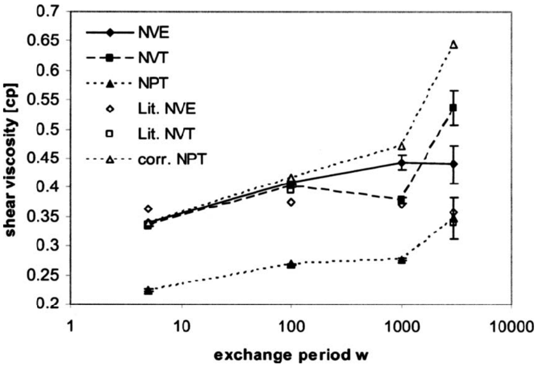

FIG. 7. Shear viscosity of hexane. The filled data points result from calculations with $T_{\mathrm{targ}}=311$ K, $\tau_T=0.2$ ps, $p_{\mathrm{targ}}=101.3$ kPa, and $\tau_p=0.5$ ps for the manostat and the thermostat. The results of the more suitable *NPT* calculations with the corrected pressure to obtain the same densities as in the *NVE* and *NVT* simulations had $p_{\mathrm{targ}}=60\,000$ kPa instead. As in all the other graphs, the results have been compared to the reference of Bordat and Müller-Plathe (Ref. 9).

Since Bordat and Müller-Plathe[9] compared their results to previous simulations of Rivera and Alejandre,[28] they chose the unusual simulation conditions $T=311$ K and $\rho=700$ kg/m^3. While the density $\rho=660$ kg/m^3 found at $p=101.3$ kPa is comparable to measured densities at standard pressure and 313 K of $\rho=639$ kg/m^3, choosing the standard pressure as the target value for the manostat leads to systematical errors. The disagreement of the shear viscosities between *NVT* and *NPT* conditions is entirely due to the density deviation and has nothing to do with the application of a Berendsen manostat within the RNEMD algorithm.

This observation leads to the question how sensitive the shear viscosity reacts on the variation in the two target properties fixed by the thermostat and the manostat. Unlike in the water case, the viscosity dependence on the temperature for hexane is weaker by an order of magnitude. A variation in temperature from the standard simulations at 311 K by up to $\pm 7\%$ leads to variations in the shear viscosity up to 5% [Fig. 8(a)]. In analogy to the water model, we assume that an Arrhenius-like behavior leads to an activation energy of -0.14 kJ/mol. Note that the behavior is not as visible as in the water simulations since the ratio of the gradient $\Delta\nu/\Delta T$ and the error of each data point are smaller than in the water simulations. The linear dependence is also an indicator that an *NVE* run with a (linearly) drifting temperature finally shows the shear viscosity at the average temperature. This small dependence is the counterexample to the case demonstrated in the water simulations.

On the other hand, a small variation in the target pressure [Fig. 8(b)] for the system by up to 5% does not produce any significant change in the shear viscosity of *n*-hexane as is expected for an incompressible fluid.

The water case has shown that *NVE* runs, in which the temperature tends to increase due to truncation errors (especially when long range forces are important), could lead systematically to small shear viscosity. However, the temperature drift in the *n*-hexane simulations with an exchange period of $w \geqslant 100$ is not observable (less than 0.1 K in 1 ns),

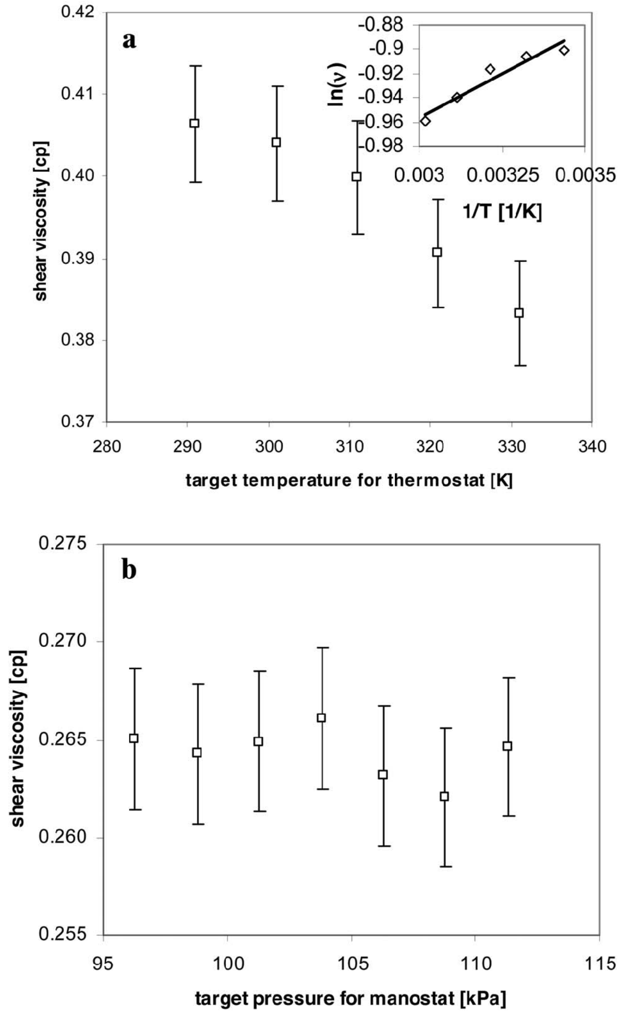

FIG. 8. Dependence of shear viscosities of hexane on deviation in temperature and pressure. (a) The results of *NVT* runs with constant τ_T=0.2 ps show small (less than 7% over the observed range) almost linear dependence of the shear viscosity on the temperature. (b) The results of *NPT* runs with constant T_{targ}=311 K, τ_T=0.2 ps, and τ_p=0.5 ps show no significant dependence of the shear viscosity on the pressure in the observed range. Thus if the pressure in *NVT* runs is off by 10%, the shear viscosity remains the same within error bars.

so the problem does not arise in the runs here. However, be aware that for small exchange periods, a temperature drift can be observed: With w=5, the drift is −28 K in 1 ns.

We also tested the influence of the temperature coupling time on the calculated shear viscosity. The influence is below 10% as in the case of water. It appears to be more systematic though: For constant *NVT* simulations, there is a trend of decreasing shear viscosities with increasing coupling times (Fig. 9). Varying from very short temperature coupling times of 0.05 ps (which violate the rule that the coupling constant should be >100 times larger than the time step) to longer ones of 2 ps, the observed shear viscosity decreases and approaches asymptotically 0.403 cP, the shear viscosity at constant *NVE* conditions. At coupling times of 2 ps for the thermostat, the *NVT* simulations agree to within half of the error bars with the *NVE* results. Our default temperature coupling time of 0.2 ps yields shear viscosities, which still agree within the error bars.

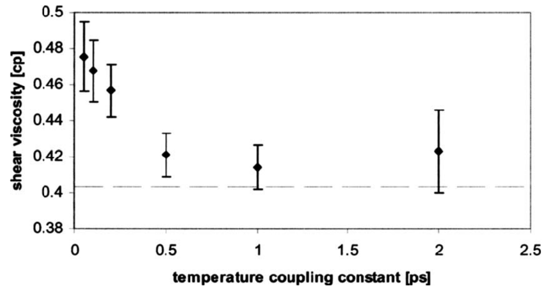

FIG. 9. Shear viscosity of hexane under constant *NVT* conditions with different coupling times at an exchange rate of w=1000. The Berendsen thermostat was parametrized to achieve a target temperature T_{targ}=311 K with a coupling constant τ_T=0.2 ps. The dotted line is the shear viscosity of the corresponding *NVE* calculation.

V. CONCLUSIONS

The reverse nonequilibrium method has been used to calculate the shear viscosities of molecular fluids using constant *NVE*, *NVT*, and *NPT* conditions. Starting with the Lennard-Jones liquid argon, the complexity of intermolecular interactions and flexibility of the chosen system has been increased up to a fully flexible liquid in atomistic detail. We studied the accuracy of the RNEMD method for the liquids under the different simulation conditions and looked for a significant influence of the parameters of the Berendsen thermostat and manostat on the shear viscosities.

The calculated shear viscosity depends much more on the state of the system (temperature and density) than on the ensemble used. Its temperature dependence becomes an issue if the temperature does not remain constant without a thermostat. In the example of SPC/E water under *NVE* conditions, potential truncation causes heating of the system, so that the calculated viscosity is a badly defined average over a temperature range. In such cases, *NVE* calculations are in practice less accurate than *NVT* calculations. (We expect this problem to completely disappear when an energy-conserving treatment of the electrostatic interactions, such as Ewald summation is used. This is, however not the subject of the present investigation.)

The strong density dependence of the shear viscosity may cause an apparent difference between viscosities obtained under constant-volume and constant-pressure conditions, if the force field is such that under *NPT*, it favors a density different from what is imposed by *NVT*. If the density of both ensembles is the same, they have the same viscosity. The force field problems were observed in our *n*-hexane system and, to a smaller extent, also in the SPC/E water. For *n*-hexane we showed that they could be removed by bringing the density of the *NPT* simulation to that of the *NVT* simulation. Additionally, we demonstrated in the case of argon that large perturbations (shear rates beyond the linear response limit) can cause the density to increase. The concomitant viscosity increase causes the onset of shear thinning to be delayed in *NPT* compared to *NVT* calculations.

This contribution shows that a thermostat and/or a manostat can be used with RNEMD (summarized in Fig. 10), provided certain precautions are taken. One should keep in mind, though, that RNEMD itself requires neither external

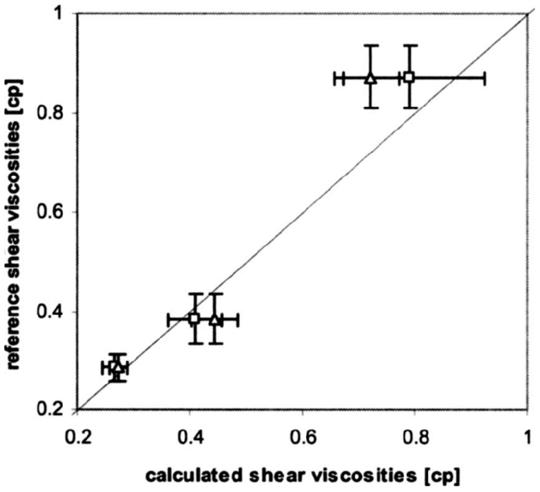

FIG. 10. Comparison of shear viscosities at *NVE*/*NVT* conditions and *NPT* conditions with the calculated values and error bars of Bordat and Müller-Plathe (Ref. 9). The x coordinates of the squares report for each system in this work the average of all reported *NVE* and *NVT* simulations omitting the simulations with the smallest and the biggest exchange period w. The x coordinates of the triangles report the average of the *NPT* simulations at exchange periods $w=100$ and $w=1000$. The error bars in the x direction take into account the error bars of each calculated shear viscosity and the variation in these shear viscosities.

thermostat nor manostat, and it is the only NEMD method which operates at constant *NVE* conditions. As any thermostat or manostat can be a potential source or sink of linear momentum, they should be avoided as a matter of principle, unless requirements from outside the RNEMD scheme dictate their use. Such outside requirements can arise often in practical simulations, for example, from the need to counteract heating of the simulations due to truncation errors or from the need to conduct *NPT* simulations because the system density is not *a priori* known.

[1] F. Müller-Plathe, Phys. Rev. E **54**, 4894 (1999).

[2] M. P. Allen and D. J. Tildesley, *Computer Simulation of Liquids* (Oxford Science, Oxford, 1987).

[3] D. A. McQuarrie, *Statistical Mechanics* (Harper Collins, New York, 1976).

[4] R. Kubo, M. Toda, and N. Hashitsume, *Statistical Physics II* (Springer, Berlin, 1985).

[5] G. P. Morriss and D. J. Evans, Mol. Phys. **54**, 629 (1985).

[6] G. P. Morriss and D. J. Evans, Phys. Rev. A **35**, 792 (1987).

[7] G. Arya, E. J. Maginn, and H.-C. Chang, J. Chem. Phys. **113**, 2079 (2000).

[8] F. Müller-Plathe, J. Chem. Phys. **106**, 6082 (1997).

[9] P. Bordat and F. Müller-Plathe, J. Chem. Phys. **116**, 3362 (2002).

[10] M. S. Kelkar, J. L. Rafferty, and E. J. Maginn, Fluid Phase Equilib. **260**, 218 (2007).

[11] M. Zhang, E. Lussetti, L. E. S. de Souza, and F. Müller-Plathe, J. Phys. Chem. B **109**, 15060 (2005).

[12] T. Terao, E. Lussetti, and F. Müller-Plathe, Phys. Rev. E **75**, 057701 (2007).

[13] E. Lussetti, T. Terao, and F. Müller-Plathe, J. Phys. Chem. B **111**, 11516 (2007).

[14] M. Zhang and F. Müller-Plathe, J. Chem. Phys. **123**, 124502 (2005).

[15] M. Zhang and F. Müller-Plathe, J. Chem. Phys. **125**, 124903 (2006).

[16] D. Reith and F. Müller-Plathe, J. Chem. Phys. **112**, 2436 (2000).

[17] W. L. Cavalcanti, X. Chen, and F. Müller-Plathe, Phys. Status Solidi A **204**, 935 (2007).

[18] X. Chen, P. Carbone, W. L. Cavalcanti, G. Milano, and F. Müller-Plathe, Macromolecules **40**, 8087 (2007).

[19] F. Müller-Plathe, Comput. Phys. Commun. **78**, 77 (1993).

[20] K. Tarmyshov and F. Müller-Plathe, J. Chem. Inf. Model. **45**, 1943 (2005).

[21] P. W. Atkins, *Physical Chemistry*, 5th ed. (Oxford University Press, Oxford, 1994).

[22] F. Müller-Plathe and P. Bordat, in *Novel Methods in Soft Matter Simulations*, Lecture Notes in Physics Vol. 640, edited by M. Karttunen, I. Vattulainen, and A. Lukkarinen (Springer, Heidelberg, 2004), p. 310.

[23] H. J. C. Berendsen, J. P. M. Postma, W. F. van Gunsteren, A. DiNola, and J. R. Haak, J. Chem. Phys. **81**, 3684 (1984).

[24] D. J. Evans and G. P. Morriss, *Statistical Mechanics of Nonequilibrium Liquids* (Academic, London, 1990).

[25] X. Chen, P. Carbone, W. L. Cavalcanti, G. Milano, and F. Müller-Plathe, Macromolecules **40**, 8087 (2007).

[26] H. J. C. Berendsen, J. R. Grigera, and T. P. Straatsma, J. Phys. Chem. **91**, 6269 (1987).

[27] *CRC Handbook of Chemistry*, 73rd ed. (CRC Press, London, 1992–93).

[28] J. L. Rivera and J. Alejandre, Fluid Phase Equilib. **185**, 389 (2001).

4. Nicht-Gleichgewichtssimulationen an Membranen

4.1. Massentransport: Vergleich von Senfgas und Heptan

Zu den maßgeblichen Vorteilen von Molekulardyamiksimulationen gehört nicht nur die große Auflösung im atomaren Maßstab, sondern auch die Möglichkeit, gefährliche Substanzen auf eine komplett risikofreie Art und Weise zu untersuchen.

Senfgas, Sulfur Mustard, Yperit: Dieses als Kampfstoff eingesetzte, trotz seines Namens flüssige Reagens trägt verschiedenste Bezeichungen und ist das wohl bekannteste militärisch genutze Zellgift. Während der Mechanismus seiner zerstörerischen, am Genmaterial von Zellen angegreifenden Wirkung gut verstanden ist [32], so finden sich in der wissenschaftlichen Literatur keine Aussagen über den Weg des Senfgasmoleküls von der Hautoberfläche bis ins Innere des Zellkerns.

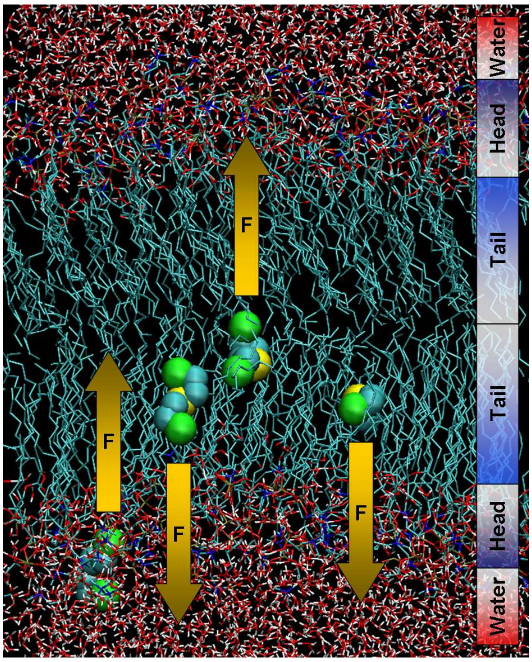

Abb. 3: Momentaufnahme während der Simulation: Mittels konstanter externer Kräfte werden vier Senfgasmoleküle durch die Membran (Kopfgruppen: braun, blau, rot; Schwanzgruppen: cyan) gezogen

Mit dieser ersten Studie des Transportes von Senfgas im Körper untersuchen wir den möglichen Permeationsprozess des Senfgasmoleküls direkt durch die Membran. Als Vergleichs- und Referenzobjekt ziehen wir Heptan heran, das mit Senfgas viele Ähnlichkeiten aufweist. So besitzen die Moleküle etwa dasselbe Volumen und wenn man zu Simulationszwecken die Wasserstoffatome in die Kohlenstoffatome hineinparametrisiert (united atoms Ansatz), so besitzen beide auch sieben (Super-)Atome. In der Ladungsverteilung unterscheiden sich beide Moleküle aber signifikant. Während Senfgas durch die elektronegativen Chloratome eine große interne Ladungsverschiebung aufweist, was in der Parametrisierung von Simulationen zu ausgeprägten Punktladungen führt, ist eine solche Polarisierung im Alkan nicht zu beachten. Dementsprechend sind die Punktladungen hier verschwindend klein.

In dieser Publikation (J. Hazard. Mat. 138 (2009) 13-24) zeigen wir, dass sich Senfgas bedeutend schneller durch die für biologische Systeme exemplarische Dipalmitoylphosphatidylcholin-Membran ziehen lässt als Heptan. Wir weisen mittels Gleichgewichtssimulationen nach, dass dies damit zu tun hat, dass sich Senfgasmoleküle in der Membran bedeutend flexibler bewegen als Heptanmoleküle. Letztere richten sich mit den Schwänzen der Lipide aus und nehmen dort eine bevorzugte Position mit langen Retentionszeiten ein. So ist eine Reorientierung des Senfgasmoleküls auch zwischen den Lipidschwänzen möglich, während Heptanmoleküle dazu in die Region zwischen den Monoschichten diffundieren müssen. Mittels Nichtgleichgewichtssimulationen quantifizieren wir diesen Prozess, indem wir die kompletten Boxdurchgänge der Moleküle vergleichen und aufzeigen, in welchen Regionen die Moleküle während der induzierten Durchgänge am längsten verweilt haben.

A comparison of sulfur mustard and heptane penetrating a dipalmitoylphosphatidylcholine bilayer membrane

Thomas J. Müller*, Florian Müller-Plathe

Theoretische Physikalische Chemie, Eduard-Zintl-Institut für Anorganische und Physikalische Chemie, Technische Universität Darmstadt, Petersenstrasse 20, 64287 Darmstadt, Germany

ARTICLE INFO

Article history:
Received 28 August 2008
Received in revised form 6 December 2008
Accepted 28 January 2009
Available online xxx

Keywords:
Sulfur mustard
Mustard gas
DPPC
Penetration
Diffusion
Molecular dynamics

ABSTRACT

In the present molecular dynamics simulations we study the chemical warfare agent sulfur mustard (bis(2-chloroethyl) sulfide) and the alkane heptane inserted into a dipalmitoylphosphatidylcholine (DPPC) bilayer, a generic model for a biological membrane. We investigate the diffusion, the orientation, the preferred positioning, and the end-to-end distance of the solutes within the membrane as well as the corresponding coupling times. We compare results of equilibrium simulations and simulation at different external forces, which drag the solutes through the membrane. These properties lead to a general comparison of the rotational and translational behaviors of the two solutes during the penetration of the membrane. We show that sulfur mustard, due to its atomic charge polarization, its bigger flexibility and its smaller molecular volume, is the faster moving molecule within the membrane. In last consequence, we show that this leads to different limits for the transport mechanism as observed in these simulations. For heptane the hindrance to penetrate into the membrane is significantly higher than for sulfur mustard. In contrast to heptane molecules, which spend the most of the time penetrating the tail groups, sulfur mustard needs more time to escape the tail group–head group interface of the membrane.

1. Introduction

Although French, German and British chemists were working with sulfur mustard (bis(2-chloroethyl) sulfide, CAS number 505-60-2) in the 19th century [1], the oily liquid became famous in the 20th century under the names mustard gas and yperite as a persistent chemical warfare agent which was first used by the Germans to win a tactical victory against English troops in the battle near Ypres in 1917 during World War I. The warfare agent caused many deaths but far more painful casualties for which it became famous [2]. During the 20th century sulfur mustard was used in military conflicts by many nations around the world. The most recent documented usage of sulfur mustard was in 1988 against the Kurds in Iraq. Currently several nations still have old stocks of sulfur mustard [3]. The most recent official declaration of previously unreported stockpiles was made by Libya in 2004 [1].

At room temperature sulfur mustard is a oily fluid. Due to impurities weaponized sulfur mustard is brownish (yellow to black) with a slight odour of garlic, mustard and rubber. Pure $C_4H_8C_{12}S$ is a colorless viscous liquid with a melting point at 14 °C. Sulfur mustard is barely soluble in water while it has a high solubility in organic solvents like acetone and ether, fats and oils. [4,5] Exposure to sulfur mustard causes skin and eye injuries and can also damage the respiratory system. Since sulfur mustard is a potent alkylating agent, it causes vesication of epidermal surfaces (blisters). At high dose exposure, it is genotoxic, mutagenic and carcinogenic. This toxicity is related to the ability of sulfur mustard to spontaneously form onium compounds which react with electron rich sulfhydril (–SH) and amino (–NH_2) groups of proteins, nucleic acids and other tissue macromolecules [6].

The severe impact of sulfur mustard on the human health comprise the majority of the work published in peer-reviewed literature. Detection, description of poisoning effects and treatment are a major part of the contributions. Physicochemical contributions, however, are quite sparse. Recently, Shukla et al. performed quantum calculations on the reaction path of nitrogen mustard derivates on DNA [7]. While the reaction schemes for reactions within the cell have been studied in detail, there is, to our best knowledge, no study about the transport mechanisms. The dependence of the toxicity on the intake path (oral, inhalation, dermal and eye) is well known but how the molecules get into the cells, where they attack DNA, is not reported. General knowledge about the membrane penetration of sulfur mustard is also important for the decontamination process, since often emulsions or more recently microemulsions [8] are used as decontamination agents.

This work starts investigating the transport process at a basic level. To act as an alkylating agent, the molecule has to travel across several membranes to get to the DNA. Since membranes are

---

* Corresponding author. Tel.: +49 6151 16 5289; fax: +49 6151 16 6526.
E-mail address: t.mueller@theo.chemie.tu-darmstadt.de (T.J. Müller).

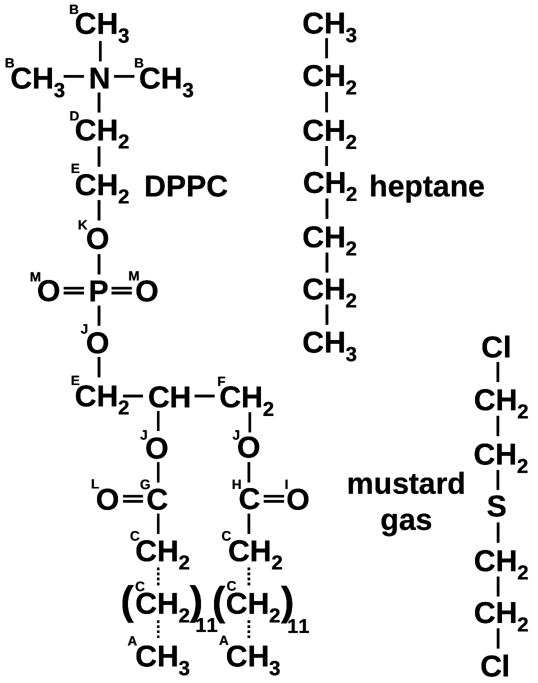

Fig. 1. Schematic specification and naming convention of the simulated molecules.

generally barriers to transport processes, we investigate in this computer simulation some aspects of the physicochemical behavior of sulfur mustard molecules in a model dipalmitoylphosphatidylcholine (DPPC) bilayer membrane, like their orientation, their preferred localization, and the forces required to move them. For reference, we compare these results to the structurally comparable *n*-heptane molecules in the same DPPC membrane (cf. Fig. 1).

For this type of study computer simulations, in our case molecular dynamics, provide several advantages. They are not only hazardless to execute, but also allow the necessary detailed insight into the system at the atomistic level. Computer simulations are a well established and often used method to study small molecules within membranes. Next to water, which is one of the most investigated molecules [9–11], because it is also of importance as the solvent of biological membrane systems, other relevant biological molecules like different sugars [12–14], helical structures [15], or anaesthetics [16] are topics of recent research. Computer simulations are often used to characterize the interactions between small molecules and biological membranes [17,18] and gas permeability with and without channels [19].

The present work is aimed at a qualitative understanding of the microscopic structures and processes only, as for the most part, there are no experimental values of sufficient accuracy to compare with. The understanding of motion patterns is important. A secondary goal is the investigation and elucidation of qualitative differences between the semi-hydrophobic sulfur mustard, which contains a few hetero atoms and the completely hydrophobic *n*-heptane. Using a united atoms approach for this study both molecules consist of seven atoms and are also comparable in size. But the force field description of the two molecules differ significantly in their partial charges (which sulfur mustard has and heptane has not). As we are at present not after quantitative transport coefficients, we use off-the-shelf force field parameters without further optimization, which are deemed good enough for both objectives.

2. Method

The simulation package which was chosen for this investigation is YASP, which was initially written by Müller-Plathe [20] and has recently been parallelized by Tarmyshov and Müller-Plathe [21].

The motion of the atoms in this program is based on a potential built of six different parts [22]:

$$V_{\mathrm{tot}} = V_{\mathrm{LJ}} + V_{\mathrm{Coulomb}} + V_{\mathrm{angle}} + V_{\mathrm{torsion}} + V_{\mathrm{hd}} + (V_{\mathrm{bond}}) \tag{1}$$

the non-bonded potentials were based on Lennard–Jones interaction V_{LJ} (applying the Lorentz-Berthelot mixing rules [23]) and the Coulomb interaction of partial charges V_{Coulomb}. The truncation error induced by using a cutoff radius was reduced applying a reaction field correction. Of the bonded potentials we used the harmonic angle potential V_{angle}, the harmonic dihedrals potential V_{hd}, and the cosine based torsion potential V_{torsion} while we did not use the harmonic bond potential but fixed the distances between bonded atoms using the SHAKE algorithm [24].

To change from simulations at constant number of particles, constant volume and constant energy (NVE) to simulations at constant temperature (NVT) a Berendsen thermostat was applied to couple the system temperature to an external bath. To perform simulations at constant pressure (NPT) instead of constant volume we use additionally a Berendsen manostat [25].

In addition to equilibrium simulations, YASP also allows the user to apply constant external forces F to selected atoms. This method has previously been applied to study the gas sorption and transport of small gas molecules in polyisobutylene [26]. Here it is applied to study the transport of heptane and sulfur mustard in an inhomogeneous system. The external forces are balanced in a way to conserve the total linear momentum and to avoid a drift of the system. The system responds with a flux of molecules J (which depends on the simulation box volume V, and the velocity of the particles v_i) to the applied external force (here applied in the z direction). From this flux the diffusion coefficient D can be calculated, knowing the Boltzmann constant k_{B}, the number density ρ of the penetrant molecules, the temperature T, and the external force F_z [22,27]:

$$J = \frac{1}{V}\sum_{i}(-1)^{i} v_i \tag{2}$$

$$D_{zz} = \frac{k_{\mathrm{B}}T}{\rho F_z}\langle J(t \to \infty)\rangle \tag{3}$$

This description will be compared to the diffusion coefficient calculated from the mean square displacement in equilibrium simulations using the Einstein relation:

$$D = \frac{1}{2\dim} \lim_{t\to\infty} \frac{d}{dt}\langle|\mathbf{r}(t) - \mathbf{r}(0)|^2\rangle \tag{4}$$

In this expression t is the time, $\mathbf{r}$ are the coordinates of the atoms and, when treating small molecules, the molecule's center of mass. Finally, dim is the number of spatial dimension accessible to the diffusing particle. While in homogeneous bulk the particle can diffuse in all three dimensions (dim = 3), it is inhibited in a bilayer to wander in the z direction (dim = 2).

We are looking at three different properties of the solutes in this paper: the position of a molecule, which was always characterized by the central atom (S in sulfur mustard, and CH_2 at position 4 in heptane), the end-to-end distance (ee), and the angle of the molecule to the z axis (the axis perpendicular to the membrane), which is calculated from the end-to-end vector and the z axis. For calculating distributions, the first two properties do not need any further modification. The orientation angle to the axis is different, since projecting the total orientation onto the z axis neglects the orientation in x and y directions. There are more possible orientations perpendicular to the z axis, than along it. To correct this effect of the

Table 1
Parameterization of the DPPC membrane.

Atom/group	Code[a]	Mass m [g mol^{-1}][b]	LJ epsilon ε [kJ mol^{-1}][b]	LJ sigma σ [nm][b]	Charge q [e][b]
CH_3	A	15.035	0.8672	0.3748	0
	B	15.035	0.8672	0.3748	0.4
CH_2	C	14.027	0.4105	0.407	0
	D	14.027	0.4105	0.407	0.3
	E	14.027	0.4105	0.407	0.4
	F	14.027	0.4105	0.407	0.5
CH		13.019	0.09489	0.5019	0.3
C	G	12.011	0.4059	0.3361	0.7
	H	12.011	0.4059	0.3361	0.8
N		14.0067	0.8768	0.2976	−0.5
P		30.9738	2.4467	0.3386	1.7
O	I	15.9994	1.1011	0.2871	−0.6
	J	15.9994	1.1011	0.2871	−0.7
	K	15.9994	1.1011	0.2871	−0.8
	L	15.9994	1.725	0.2626	−0.7
	M	15.9994	1.725	0.2626	−0.8
Bond[c]	Bond length b [nm]	Torsion	Multiplicity	Phase shift τ [°]	k_{torsion} [kJ mol^{-1}]
CH_x–N[d]	0.147	CH_2–CH_2–CH_2–CH_x[d]	3	0	11.84
CH_2–CH_x[d]	0.153	C–CH_2–CH_2–CH_2	3	0	11.84
CH_x–O[d]	0.143	CH_3–N–CH_2–CH_2	3	0	7.54
P–O	0.161	N–CH_2–CH_2–O	3	0	11.72
P=O	0.148	CH_x–CH_2–O–P[d]	3	0	7.54
C–O	0.133	CH_2–O–P–O	3	0	2.1
C=O	0.123	O–CH_2–CH–CH_2	3	0	11.84
C–CH_2	0.148	C–O–C–CH_2	2	180	33.4
		CH_x–CH_x–O–C[d]	3	0	7.54
		O–C–CH_2–CH_2	6	0	2
Angle	Angle α [°]	k_{angle} [kJ mol^{-1} rad^{-2}]	Harmonic dihedral	Phase shift τ [[°]]	k_{dih} [kJ mol^{-1} rad^{-2}]
CH_2–N–CH_2	109.5	420	O–C–O(I,L)–CH_2	0	0.51
Y–CH_2–CH_2[e]	111	530			
CH_2–O–P	120	530			
O–C–CH_2	113	545			
O=C–CH_2	125	750			
O–C=O	122	700			
CH_x–O–C[d]	117	635			
CH_2–CH–O,CH_2	109.5	520			
O–P=O	109.6	450			
O–P–O	103	420			
O=P=O	120	780			

[a] Different parameterization of the same atom/atom groups at different positions corresponding to Fig. 1.

[b] For non-bonded interactions first, second, and third neighbor interactions have set to 0.

[c] All bonds have been constrained to their average value using the SHAKE algorithm with a maximum allowed number of 500 cycles and a tolerance of 10^{-6}.

[d] CH_x is CH, CH_2, or CH_3.

[e] Y is N, C, CH_2 or O.

metric, the net orientation is divided by the sine of the orientation angle.

To quantify the molecular dynamical behavior of the solutes (angles to the z axis, end-to-end distances (the length of the end-to-end vector), and the z coordinate of the molecules, which defines their position along the membrane normal), the autocorrelation functions $A(t)$ for these properties have been evaluated:

$$A(t) = \frac{\langle (a(0) - \langle a \rangle)(a(t) - \langle a \rangle) \rangle}{(\sigma(a))^2} \tag{5}$$

In this notation a symbolizes the quantity in question, $a(t)$ the specific value of this quantity at time t and σ its variance. The autocorrelation functions have been least-squares fitted to an exponential:

$$A(t) = e^{-t/\tau_{\mathrm{corr}}} \tag{6}$$

The fitting parameters τ_{corr} are reported as the corresponding correlation times.

3. Computational details

3.1. Force fields

Since the goal of this work is not to calculate hard numbers, but to see tendencies and principles as a first step to understand the transport of sulfur mustard-like molecules, we forwent a new parameterization of a new lipid force field and translated the existing united atom bilayer force field GROMOS96 45A3 A [28] into the YASP functional form. This leads to the parameters reported in Table 1.

The definition of the potentials in GROMOS and in YASP is similar, so that we expected the behavior of our membrane to be comparable to the GROMOS one. Nevertheless there are two differences. While the GROMOS implementation works with flexible bonds the YASP adoption works with constrained bonds which where fixed to their average value using the SHAKE algorithm. The calculation of the electrostatic interactions in YASP uses a single atomic cutoff plus a reaction-field

Table 2
Force field parameters of sulfur mustard and heptane.

	n-Heptane	Sulfur mustard
Mass [$\mathrm{g\,mol^{-1}}$]	$m_{\mathrm{CH_3}} = 15.023475$ $m_{\mathrm{CH_2}} = 14.01565$	$m_{\mathrm{Cl}} = 35.453$ $m_{\mathrm{CH_2}} = 14.01565$ $m_{\mathrm{S}} = 32.06$
ε [$\mathrm{kJ\,mol^{-1}}$][a]	$\varepsilon_{\mathrm{CH_3}} = 0.914$ $\varepsilon_{\mathrm{CH_2}} = 0.54$	$\varepsilon_{\mathrm{Cl}} = 1.25556$ $\varepsilon_{\mathrm{CH_2}} = 0.40587$ $\varepsilon_{\mathrm{S}} = 1.90587$
σ [nm][a]	$\sigma_{\mathrm{CH_3}} = 0.391$ $\sigma_{\mathrm{CH_2}} = 0.393$	$\sigma_{\mathrm{Cl}} = 0.346982$ $\sigma_{\mathrm{CH_2}} = 0.33611$ $\sigma_{\mathrm{S}} = 0.3330768$
Partial charge [e][a]	$q_{\mathrm{CH_3}} = 0$ $q_{\mathrm{CH_2}} = 0$	$q_{\mathrm{Cl}} = -0.174487$ $q_{\mathrm{CH_2}} = 0.140655$[b] $q_{\mathrm{CH_2}} = 0.164474$[c] $q_{\mathrm{S}} = -0.261284$
Bond length [nm]	$b_{\mathrm{CH_x-CH_x}} = 0.153$[d]	$b_{\mathrm{Cl-CH_2}} = 0.1767$ $b_{\mathrm{CH_2-CH_2}} = 0.1541$ $b_{\mathrm{CH_2-S}} = 0.181$
Angle [°]	$\alpha_{\mathrm{CH_x-CH_x-CH_x}} = 109.47$[d]	$\alpha_{\mathrm{CH_x-CH_x-CH_x}} = 109.47$
k_{angle} [$\mathrm{kJ\,mol^{-1}\,rad^{-2}}$]	$k_{\mathrm{CH_x-CH_x-CH_x}} = 520$[d]	$k_{\mathrm{Cl-CH_2-CH_2}} = 484$ $k_{\mathrm{CH_2-CH_2-S}} = 545$ $k_{\mathrm{CH_2-S-CH_2}} = 475$
k_{torsion} [$\mathrm{kJ\,mol^{-1}\,rad^{-2}}$][e]	$k_{\mathrm{CH_x-CH_2-CH_2-CH_2}} = 11$[d] $m = 1, \tau = 0$	$k_{\mathrm{Cl-CH_2-CH_2-S}} = 5.92$ $m = 1, \tau = 180$
	$k_{\mathrm{CH_x-CH_2-CH_2-CH_2}} = 6.5$[d] $m = 2, \tau = 0$	$k_{\mathrm{CH_2-CH_2-S-CH_2}} = 5.92$ $m = 1, \tau = 180$
	$k_{\mathrm{CH_x-CH_2-CH_2-CH_2}} = 9.6$[d] $m = 3, \tau = 0$	

[a] Intramolecular 1–2, 1–3 and 1–4 interactions have been omitted totally.
[b] CH_2 next to the chlorine atom (at positions 2 and 6).
[c] CH_2 next to the sulfur atom (at positions 3 and 5).
[d] CH_x may be CH_2 or CH_3.
[e] In order to reduce any ambiguous influences, which do not come from the non-bonded forces, in the non-equilibrium part of this study, all torsions have been reduced to zero.

correction instead of charge groups which GROMOS takes into account.

The parameterization of the united atom force field for sulfur mustard (Table 2) was derived from several sources. The non-bonded Lennard–Jones interactions were transferred form the GROMOS96 force field [29], while bond lengths between atoms were taken from the CRC handbook [30]. The point charges on the atoms have been derived using a density-functional calculation (B3LYP) executed with the Gaussian 03 program version B.01 [31] using a 6-311G(2d,2p) basis set. In order to estimate average partial charges for the parameterization of the sulfur mustard force field we averaged the atomic partial charges derived by the built in CHELP algorithm of the all-trans conformation and of the gauche conformation of the 2–3 bond of the molecule. The geometry of the molecule was defined by the average values for bonds and angles derived above. To change form an all atom model to the united atoms model we included the charges of aliphatic hydrogen atoms into their parent carbons. The equilibrium bond angles and the associated force constants for angular vibration were again transferred from GROMOS96 [29].

3.2. *Simulation setup*

For this study, several equilibrium and non-equilibrium simulations have been performed. This section deals first with the setup of the equilibrium simulations, followed by the setup of the non-equilibrium simulations.

3.2.1. *Pure sulfur mustard*

900 sulfur mustard molecules have been equally distributed on a grid in a cubic box with a side length of 7.741 nm. The equilibration was performed with a cutoff of 0.8 nm, a neighbor list with a cutoff of 1.0 nm which was updated every 15 time steps, and a time step of 2 fs. The simulation was performed at constant NVT conditions enforced using a Berendsen thermostat with a target temperature of $T_{\mathrm{targ}} = 300\,\mathrm{K}$ and a temperature coupling time of $\tau_T = 0.2$ ps. After 10,000 time steps, the temperature already reached the target temperature and fluctuated during the next 10,000 time steps with a standard deviation of 3 K. Switching to constant pressure (NpT) simulations using a Berendsen manostat with a target pressure $p_{\mathrm{targ}} = 101.3$ kPa and a pressure coupling time of $\tau_p = 3$ ps was followed by another equilibration of 10,000 time steps. The subsequent production ran with a less pressure-constrained system (in order to avoid artifacts from too small coupling constants τ_p was set to 5 ps in the production runs of all systems) for a total time of 6 ns while writing out trajectory data every 1 ps.

3.2.2. *Pure heptane*

400 molecules were equally distributed on a grid in a cubic box with side length 7.741 nm. The equilibration was also first performed for 10,000 time steps using a constant volume, constant temperature simulation ($T_{\mathrm{targ}} = 300\,\mathrm{K}$, $\tau_T = 0.2$ ps) with a cutoff of 0.8 nm, a neighbor list with a cutoff of 1.0 nm which was updated every 15 time steps, a time step of 2 fs. Another equilibration simulation for 10,000 time steps at constant temperature and pressure ($p_{\mathrm{targ}} = 101.3$ kPa and $\tau_p = 1.5$ ps) was finally followed by the evaluation simulation which was performed for 6 ns keeping the same parameter setup except the pressure coupling constant which was increased to $\tau_p = 5$ ps. Every 1 ps, coordinates, velocities, and intermediately evaluated values were written into files.

3.2.3. *Sulfur mustard and heptane in water*

The initial startup configuration for these simulations was an equilibrated water box consisting of 1500 extended simple point charge (SPC/E) [32] water molecules. We introduced one heptane molecule into this box and equilibrated it using a cutoff of 1.2 nm, a neighbor list with a cutoff of 1.4 nm and an update frequency of every 5 time steps. The reaction field dielectric constant was set to 72 (the value for water). Temperature was controlled by a Berendsen thermostat ($T_{\mathrm{targ}} = 325\,\mathrm{K}$, $\tau_T = 0.2$ ps) and pressure by a Berendsen manostat with $p_{\mathrm{targ}} = 101.3$ kPa and $\tau_p = 1.0$ ps. Spurious drift was removed from the system every 1000 time steps, while the trajectories and calculated data were written out every 1 ps for sulfur mustard and every 0.4 ps for heptane. Using a time step of 2 fs, the equilibration was performed for 1 ns guaranteeing a constant total energy and a constant density.

Switching the force field parameters of the heptane molecule to those of sulfur mustard and performing another equilibration with the same parameters just mentioned led to the starting coordinates for the water/sulfur mustard system.

The production runs for both systems were performed with the same parameterization as in the equilibration. They ran for a total simulation time of 15 ns.

3.2.4. *DPPC bilayer*

The bilayer was constructed from two DPPC monolayers and 3655 SPC/E water molecules. A monolayer was built from 64 all-trans DPPC molecules arranged on an equally spaced 8 × 8 grid (molecules oriented perpendicular to the *xy* plane) with total side length $l = 6.25$ nm. To produce the starting box, the two layers were positioned tail against tail and the cuboid box was filled with 3655 SPC/E water molecules. They were again put on a grid, so that the dimension of the whole box became 6.25 nm × 6.25 nm × 8.74 nm. This structure was first relaxed with several very short simulations (1000 time steps) at constant volume and constant energy: The initial temperature was 325 K, the cutoff was 0.8 nm using a reaction field dielectric $\varepsilon = 54$ [28], the neighbor list cutoff was 1.0 nm, and the neighbor list was updated every 15 time steps. The time step was stepwise increased from 10^{-13} to 10^{-4} ps. After each run, the velocities of the atoms were reinitialized for the next run from a Boltzmann distribution at the target temperature. This procedure was repeated with a time step of 0.2 fs including the Berendsen thermostat with $T_{\text{targ}} = 325$ K and $\tau_T = 0.2$ ps until the temperature sank below 400 K. The temperature relaxation was finished with a simulation of 10,000 time steps with a time step of 2 fs. Then the system was shifted to constant pressure calculations additionally using independent Berendsen pressure coupling for each Cartesian direction (compressibility $\kappa = 2.77 \times 10^{-7}$ kPa^{-1}). In a first run of 1000 time steps of 2 fs, the system was forced to compact in z direction ($p_{x,\text{targ}} = p_{y,\text{targ}} = 101.3$ kPa with $\tau_{p,x} = \tau_{p,y} = 500$ ps and $p_{z,\text{targ}} = 1101.3$ kPa with $\tau_{p,z} = 5$ ps). At the end of this calculation we removed the atomic velocities again. The following longer simulation (10,000 time steps) with the same parameterization was followed by one with $p_{x,\text{targ}} = p_{y,\text{targ}} = 101.3$ kPa with $\tau_{p,x} = \tau_{p,y} = 50$ ps and $p_{z,\text{targ}} = 601.3$ kPa with $\tau_{p,z} = 5$ ps. Finally an equilibration of 2.2 ns followed with equal parameters for all directions ($p_{x,\text{targ}} = p_{y,\text{targ}} = p_{z,\text{targ}} = 101.3$ kPa with $\tau_{p,x} = \tau_{p,y} = \tau_{p,z} = 0.5$ ps).

3.2.5. *Inserting small molecules in the membrane system*

The solutes have been inserted into the equilibrated membrane box using a slow growth type procedure. In order to obtain a starting configuration for the simulations with solutes within the membrane, five heptane molecules were equally distributed in the *xy* plane in the middle of the membrane and oriented perpendicular to the *z*-axis. For the simulations with the solute molecules outside the membrane and for the non-equilibrium simulations two heptane molecules have been inserted correspondingly in the middle of the water phase.

The insertion procedure was always the same. We performed a series of consecutive simulations at constant temperature and constant volume which had the following simulation parameters in common: a cutoff of 0.8 nm, a neighbor list cutoff of 1.0 nm, which was updated every 15 time steps, and parameters for the Berendsen thermostat, $T_{\text{targ}} = 325$ K and $\tau_T = 0.2$ ps. During a total simulation time of 110 ps with increasing simulation time step from 0.2 to 2 fs, the non-bonded interactions (Lennard–Jones and Coulomb interactions) of the solutes were stepwise increased from zero to their full values reported in Table 1. This growth period was followed by another equilibration simulation of 8 ns.

Preliminary studies showed that sulfur mustard molecules have the tendency to aggregate with each other within the membrane—an effect which is beyond the scope of this work. Therefore, we reduced the number of solutes using the procedure described above to obtain systems with only one molecule for the sulfur mustard equilibrium simulations and with two molecules for all non-equilibrium simulations.

The insertion/growth procedure described above has always been performed with the heptane molecules. To generate starting configurations for systems containing sulfur mustard, we just changed the LJ parameters and partial charges of the corresponding heptane simulation into the ones of sulfur mustard. Then, keeping the same simulation setup as described above, another equilibration of 300,000 time steps (6 ns) was performed for this system.

The production runs used the parameterization already shown: $r_{\text{cutoff}} = 0.8$ nm, a neighbor list updated every 15 time steps with a cutoff of 1.0 nm, $T_{\text{targ}} = 325$ K, $\tau_T = 0.2$ ps, $p_{\text{targ}} = 101.3$ kPa, $\tau_p = 0.5$ ps, and a time step of 2 fs. For evaluation purpose the coordinates and velocities were written into a trajectory file every 1000 time steps.

3.2.6. *Equilibrium simulations of sulfur mustard and heptane in the DPPC bilayer system*

The four different systems (sulfur mustard and heptane each in the water phase and in the tail region of the DPPC system) were simulated with the same parameters: cutoff radius $r_{\text{cutoff}} = 1.2$ nm with a reaction field dielectric $\varepsilon = 54$, neighbor list cutoff 1.4 nm (updated every 15 time steps), $T_{\text{targ}} = 325$ K with $\tau_T = 0.2$ ps, diagonal pressure control ($\kappa_x = \kappa_y = \kappa_z = 2.77 \times 10^{-7}$ kPa^{-1} and $p_{x,\text{targ}} = p_{y,\text{targ}} = p_{z,\text{targ}} = 101.3$ kPa with $\tau_{p,x} = \tau_{p,y} = \tau_{p,z} = 0.5$ ps), and a time step of 2 fs. Results and trajectories were written into files every 1000 time steps.

3.2.7. *Non-equilibrium simulations of sulfur mustard and heptane in the DPPC bilayer*

The non-equilibrium simulations were performed with the same simulation parameters as employed in the corresponding equilibrium simulations. As starting configurations, we used the output of the simulations with two molecules of sulfur mustard or heptane in the water phase of the DPPC system. In addition to the system parameters mentioned above we applied in each time step an external force in the $+z$ direction to one of the two solute molecules and in the $-z$ direction to the other. The symmetrical force is necessary to prevent a net drift of the system. The total force on each molecule was distributed equally among all its atoms.

With both systems we ran simulations at total external forces (per one molecule) of 10, 20, 30, 50, 100, 120, 150 and 200 kJ mol^{-1} nm^{-1} (equal to 16.6, 33.2, 49.8, 83.0, 166.1, 199.3, 249.1, 332.1 pN). Generally, these simulations were performed for a total simulation time of at least 20 ns. Exceptions as well as the exact simulation times are reported in Section 4.

To check the influence of charges and size of the atoms, we also simulated two hypothetical molecules: a molecule of sulfur mustard constrained to have a polarity identical to that of heptane (zero partial charges), and a molecule of heptane constrained to have a polarity identical to that of sulfur mustard. With each of these parameterizations we performed simulations with a total external force per molecule of 10, 50, 100 and 200 kJ mol^{-1} nm^{-1}.

4. Results and discussion

4.1. *Characterization of the membrane system*

In Fig. 2 a density profile of the DPPC membrane in equilibrium without any solute is displayed. We also show the partial densities of specific atom types. Depending on the application of different criteria, the membrane thickness d_{mem} differs. The average distance between the density peaks yields a membrane thickness of

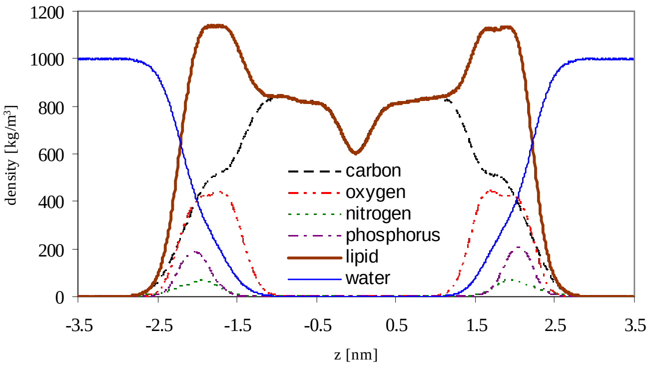

Fig. 2. Characterizing the membrane: density profiles of different atom types. On the basis of these profiles different membrane thicknesses d can be defined: $d = 4.43$ nm between the points of equal densities of water and lipid, $d = 4.079$ nm between the maxima of the phosphorus position.

Table 3
Calculated tracer diffusion coefficients D of the molecules in equilibrium simulations.

System and temperature	D (heptane) [10^{-6} cm^2/s]	D (sulfur mustard) [10^{-6} cm^2/s]	D (water) [10^{-6} cm^2/s]	D (DPPC in bilayer)[a] [10^{-6} cm^2/s]
Pure system, 300 K	17.2 ± 0.6	15.9 ± 1.0	23.6 ± 1.2	–
Solute in water, 300 K	18.5 ± 3.4	18.7 ± 2.7	23.6 ± 1.2	–
Pure system, 325 K	24.7 ± 2.3	21.4 ± 2.1	35.5 ± 2.1	0.179 ± 0.017
Solute in bilayer, 325 K	0.135 ± 0.005	2.15 ± 0.63	–	–

[a] Lateral diffusion, only in 2 dimensions.

$d_{\mathrm{mem}} = 3.771$ nm, the difference of the phosphorus maxima leads to $d_{\mathrm{mem}} = 4.079$ nm, and the one of nitrogen to $d = 3.69$ nm. All these lengths are comparable to experimentally measured thicknesses: either $d_{\mathrm{mem}} = 3.6$ nm using atomic force microscopy (AFM) cross section at 50 °C by Leonenko et al. [33] or $d_{\mathrm{mem}} = 3.87$ nm using X-ray diffraction by Tristam-Nagle et al. [34].

Another benchmark to test the lipid force field is the area per head-group A which is obtained by dividing the area of the xy plane (with box lengths L_x and L_y) by the number of lipids in a monolayer:

$$A = \frac{L_x L_y}{64}. \tag{7}$$

As Nagle and Tristram-Nagle show in their review article about membranes [35] the values measured for this property vary substantially. On the basis of that paper the authors of the GROMOS lipid force field [16], which we adopted, optimized their parameters for an area per lipid of $A = 0.61$ nm^2 (reported results range from $A = 0.57$ to 0.64 nm^2). We observed an area per head group for this force field between 0.59 and 0.60 nm^2. We consider this a sufficient agreement with the original force field, since the two calculations differ not only in the treatment of torsions but also in charge groups (which we do not use). The consequence of the smaller area per head-group is a denser system, which has to be penetrated by the solutes.

Since the motions of the solutes also depend on the motion of the environment, the diffusion constant of the lipid is the last benchmark to compare to the literature. The lateral diffusion in the x and the y direction only (in Eq. (4) the dimension is dim = 2) leads to a calculated diffusion coefficient of $D_{\mathrm{lat}} = (1.79 \pm 0.17) \times 10^{-8}$ cm^2/s. This can be compared to the diffusion coefficient $D_{\mathrm{lat}} = 1 \times 10^{-8}$ cm^2/s measured by quasi-elastic neutron scattering (QENS) at $T = 333$ K [36,37] and $D_{\mathrm{lat}} = 1.3 \times 10^{-8}$ cm^2/s measured by fluorescence recovery after photobleaching (FRAP) [38] at $T = 323$ K. Thus, although the density in the system is in the upper part of the reported values, the diffusion of the lipids is in the right order, but marginally faster.

4.2. Characterization of the solute molecules

For the pure heptane system equilibrium simulations at 300 and at 325 K lead to system densities of 718 ± 2 and 703 ± 2 kg/m^3. These densities are 6–7% larger than the experimental ones (0.67955 kg/m^3 at 298.15 K [39]) and therefore considered good enough for the following comparison. The diffusion coefficients of this and all other equilibrium systems are summarized in Table 3. The mean square displacements leading to these results are plotted in Fig. 3. For pure heptane, increasing the temperature by 25 K leads to an increase of the diffusion coefficient by more than 40%. A correlation of the end-to-end distance at 300 K leads to a correlation time τ_{ee}(heptane) of less than 1 ps and the analysis of the angle with the z axis, which in this case is an arbitrary axis, yields a correlation time τ_{angle}(heptane) = 36 ps.

The dynamical properties have also been calculated for a single heptane molecule in water (the error bars, all error bars in this article are standard deviations, for the solutes in water are bigger due to poorer statistics). The diffusion coefficients of neat heptane and heptane in water are the same within the error bars. The distribution of the end-to-end distances shows a pronounced peak at 0.74 nm, it relaxes with a correlation time of τ_{ee}(heptane in water) of less than 1 ps. The uncorrected angle to z axis profile shows the typical cosine shape of a fully sampled spherical property projected onto an axis; the corresponding correlation time is τ_{angle}(heptane in water) = 30 ps, indicating a slightly faster rotation in water than in the pure heptane system.

The simulation of pure sulfur mustard leads to a density of $\rho = (1383 \pm 3)$ kg/m^3 at 300 K and $\rho = (1340 \pm 2)$ kg/m^3 at 325 K. Compared to the density $\rho = 1270$ kg/m^3 at $T = 298.15$ K reported in the literature [4,40] the simulated system is 9% denser. The deviation of these results of this force field from the experimental value is of the same size and in the same direction as the ones for the membrane and heptane. Comparing the force field parameters for bond lengths and bond angles to results of ab initio calculations by Glukhovtsev et al. [41] we find the force field bond lengths up to 1.5% longer than the ab initio ones and the angle at the sulfur atom is bigger by 0.9% in the force field. But the thus expected lower density is overcompensated by the force field parameters for the charges and the Lennard–Jones parameters ε and σ.

The dynamical properties of the model were again tested with the diffusion coefficient (Table 3) which is about 10% smaller than that of heptane. The end-to-end distance correlation times τ_{ee}(sulfur mustard), which is 3 ps at 300 K and at 2 ps at 325 K and the axis to angle correlation time τ_{angle}(sulfur mustard) = 17 ps at 300 K supports the interpretation that sulfur mustard is a much more flexible molecule compared to heptane.

The higher flexibility of sulfur mustard in comparison to the one of heptane can also be explained by the choice of the force field parameters. In agreement with ab initio calculation of Butterfloss and Hermans [42] and the force field parameterization procedure of Wolfe et al. [43] we set the torsion barrier around the C–S bonds in the middle of the sulfur mustard molecule lower than the torsion barrier around the corresponding C–C bond in heptane. Less torsion restriction for sulfur mustard does not only lead to faster rotation around the central bonds than in heptane but also to a larger range of (non-equilibrium) conformations it can adopt.

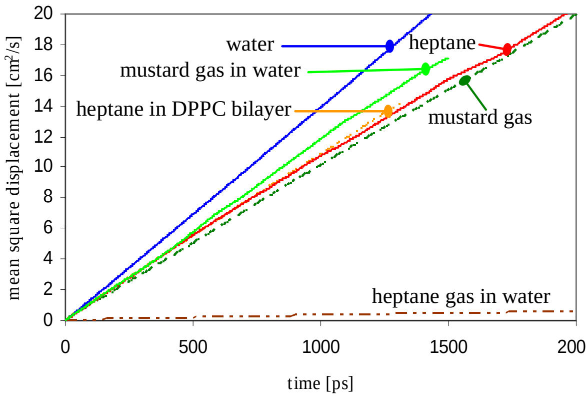

Fig. 3. The mean square displacements of selected molecules in different environments. In this resolution the graphs for heptane in DPPC bilayer, sulfur mustard in DPPC bilayer and the bilayer itself fall on top of each other.

Like in the heptane case, putting one sulfur mustard molecule into water shifts the diffusion coefficient towards the one of water. Within error bars it is still the same as for heptane in water. The correlation times at 300 K on the other hand hint a slowing down of the internal dynamics τ_{ee}(sulfur mustard in water) = 9 ps but also on a speed up of the rotational dynamics τ_{angle}(sulfur mustard) = 12 ps compared to the heptane case. The similar diffusion coefficient in spite of longer internal correlations indicates that the diffusion is mainly determined by water. Under the given accuracy, differences in the force field parameterization between the molecules do not have any significant influence on the diffusion coefficients.

4.3. Equilibrium behavior of the solutes in the membrane

When the solutes are inserted into the membrane, their available space gets confined. In this section, we compare the distributions (averaged, static properties) and the corresponding correlation times (dynamic properties) of the average z position within the membrane of the solute's central atom. Furthermore, we analyze the end-to-end distance of the solute and the angle of the end-to-end vector with the membrane normal (z axis) of sulfur mustard and heptane.

Fig. 4 shows the distribution of the z position of sulfur mustard molecules, defined by the central sulfur atoms, within the membrane. While in the case of only one solute the molecule samples the whole width of the membrane's tail region in the simulation time of 12 ns, this is not realized for five molecules. Here one can observe the effect on the distribution of the clustering of two molecules in the middle of the membrane. The fact that two molecules cluster for more then 2 ns in the middle of the membrane broadens the peaks in the center of the plot. To avoid such clustering effects we continued the sulfur mustard observation with only one molecule accepting the loss of statistics. The z position distribution is broad with a preferred residence in the middle of the tail region. There is, however, also a significant probability to find the molecule in the center of the membrane where the tails from opposite layers touch.

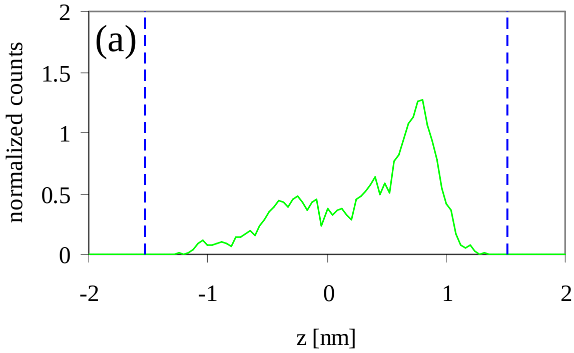

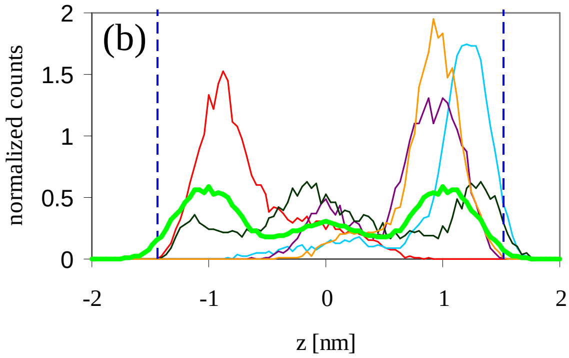

Fig. 4. Distribution of the central sulfur atom of one (in plot a) and five (in plot b) sulfur mustard molecules during simulations of 12 ns (plot a) and 19 ns (plot b). The vertical dashed lines indicate the average position of the innermost phosphorus atom. The thick line in the second plot is the average of the five atoms and of the two monolayers.

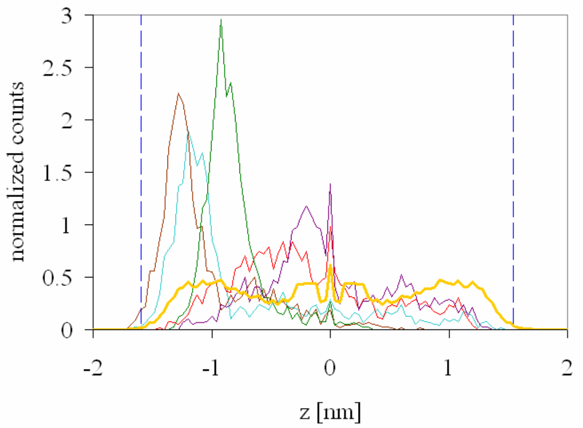

Fig. 5. Distribution on the central CH_2 groups of five heptane molecules during a simulation of 40 ns. The thick line is the average of the five heptane molecules.

For heptane (Fig. 5), no clustering was observed. But the z position distributions of the alkane molecules show other special features. First, during at least 65% of the simulation time of 40 ns, three of the five inserted molecules kept their average positions in the tail region, but nearer to the head group region than sulfur mustard. This leads to the three pronounced peaks on the left side of the profile. The other two, faster moving, molecules with broader distributions stay closer to the center of the membrane. For both we identify a pronounced sharp peak exactly in the middle of the membrane which comes from the molecules staying at the tail–tail interface for up to 10 ns.

The orientation along the z axis is measured by the angle between that axis and the end-to-end vector of the solute. Division of the raw distribution by the sine of the angle removes the metric-tensor bias and leads to the graphs in Fig. 6. For sulfur mustard, we see maxima near 0° and 180° corresponding to a parallel and an anti-parallel orientation to the z-axis. Although the most favorable orientation is an alignment with the lipid tails, there is still a count of one sixth of the maximum for orientations perpendicular to the z-axis.

In comparison, the heptane molecules exhibit a more confined orientation distribution. They show even more alignment than sulfur mustard molecules, and the amount of parallelly oriented molecules is lower. We note, not shown, that there is also a reduced rotational mobility: Two of the five molecules even do not change the net orientation (cross the 90° mark) at all. These facts indicate that the heptane molecules are caged between the lipid tails with only little space to wiggle around. Both their compatibility with the lipid tails and their larger inherent stiffness (as compared to sulfur mustard) might contribute to the reduced reorientation dynamics.

In Fig. 7 we combine the information of the position of a solute and its orientation into a contour plot. Both molecules are similar in that their intensity maxima are in the corners of the diagram, i.e. the most likely situation is the molecule being embedded among the lipid tails and oriented parallel to them. There are, however, important differences. In the sulfur mustard diagram there is a straight horizontal path connecting the two maxima at constant z = 0.75 nm. This means that sulfur mustard molecules can rotate in place while remaining in the lipid tail region. For heptane, there is

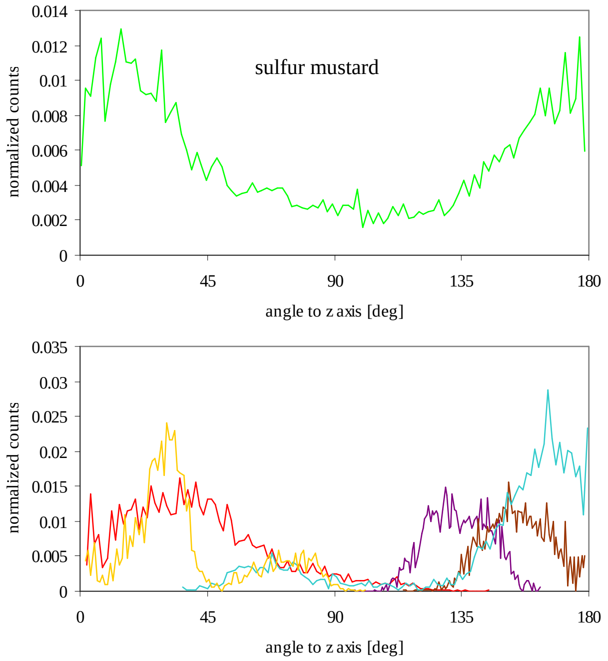

Fig. 6. Orientation of the inserted molecules within the membrane: The orientation of the sulfur mustard molecules (upper figure) over 12 ns show an equilibrated behavior, sampling the orientation parallel and anti-parallel to the *z* axis with equivalent weight. In contrast the heptane molecules show a very limited sampling of the rotational space over the simulation time of 40 ns. Three molecules even did not change the sign of their orientation with respect to the *z* axis.

a much stronger dependence between orientation and position. A heptane molecule can really only (reluctantly) adopt a perpendicular orientation at the membrane center, where opposite lipid tails touch and where the density is lower (cf. Fig. 1). A possible explanation is the lower stiffness of sulfur mustard, which would allow the molecules to reorient via an intermediate folded state, whereas the heptane molecule must rotate in a straight, extended configuration and therefore requires more free volume.

4.4. Non-equilibrium simulations of forced permeation by the solutes

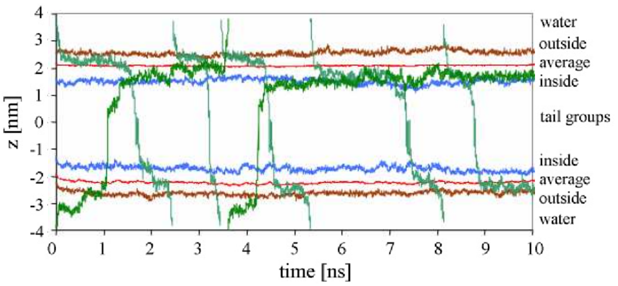

Fig. 8. Tracking the position of sulfur mustard molecules (sulfur atom). This example was taken from the simulation with an external force of 50 kJ mol^{-1} nm^{-1}. The black lines show the *z* coordinate of the central sulfur atom. The grey lines correspond to the *z* positions of specific head groups measured by the position of the phosphorus atoms; i.e. the position of the head group most exposed to the water phase (bright grey), the average position of all head groups (grey), and the *z* position of the innermost head group of the membrane (dark grey).

The application of an external force drags the two sulfur mustard or heptane molecules through the system. In Fig. 8 we visualized this dragging process for an external force of 50 kJ mol^{-1} nm^{-1} (83 pN) applied to one sulfur mustard molecule in the +*z* direction (upwards) and the same force on the other sulfur mustard molecule in the −*z* direction (downwards). We also introduce four different spatial regions important for the following discussion. The water region is the space between the outermost (the most exposed to the water region) phosphorus atoms of the two monolayers (recall that the box is periodic). The tail region is the space between the innermost phosphorus atoms of the two monolayers. The two head group areas are defined as the space between the outermost and the innermost phosphorus atoms of the same monolayer. These two regions are treated separately. The head-in group refers to the head group through which the solute penetrates form the water region into the tail region. The head-out group is the head group through which the solute leaves the membrane and diffuses into the water region.

For the calculation of cycles and residence times, sampling starts at the moment when the solute crosses the first region interface and ends when the solute crosses a region interface for the last time in that simulation run. This choice allowed us to take into account only completely traversed regions.

We tried several drag forces between 10 and 200 kJ mol^{-1} nm^{-1}. For heptane simulations up to and including an external force of 30 kJ mol^{-1} nm^{-1}, we did not observe any region crossing events. For sulfur mustard, however, we have seen at least one crossing between regions during each simulation, even for

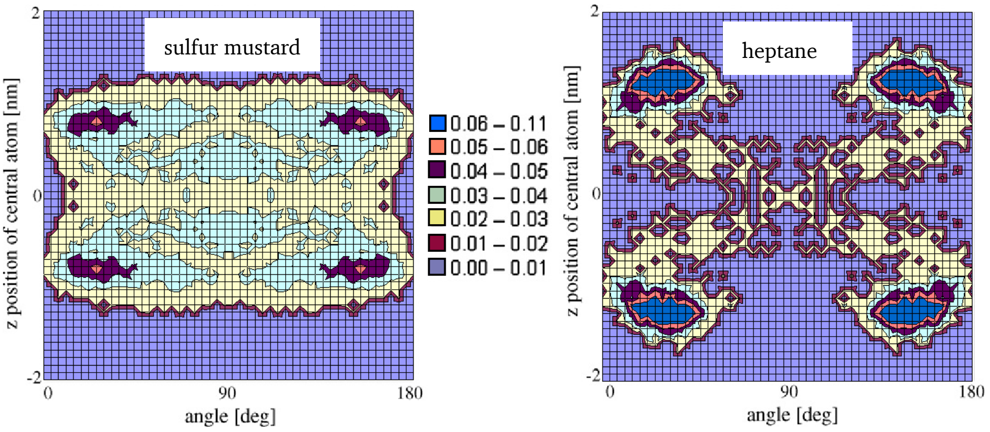

Fig. 7. Correlation of the orientation and the position in *z* direction of the solutes. In case of sulfur mustard, the solute travels across the whole membrane and may have any orientation at any position in the membrane. The average position peaks of heptane molecules, which keep their *z* position for a much longer time than the sulfur mustard, are very pronounced. And there is a clear path obvious under which circumstances the molecule is allowed to change its orientation.

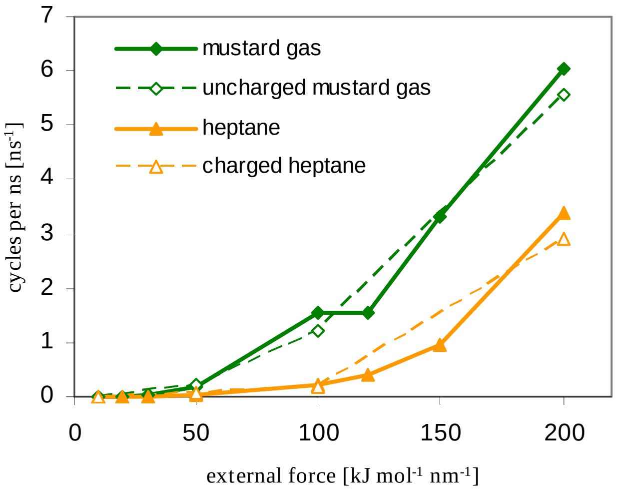

Fig. 9. Number of membrane penetration cycles per one sulfur mustard molecule (squares) or one heptane molecule (triangles) during 1 ns as a function of the external force acting on the molecules. While at forces smaller than the threshold of 50 kJ mol^{-1} nm^{-1} no complete membrane penetration was traceable, the molecules started to break through the membrane at higher external forces. Sulfur mustard is the faster of the two molecules. Also included are unphysically modified molecules in which the patterns of partial charges have been modified.

$F = 10$ kJ mol^{-1} nm^{-1}. Increasing the external force, a full cycle (a molecule traversing the entire z dimension of the box and arriving at the periodic image of region border it crossed first) was first observed for sulfur mustard at 30 kJ mol^{-1} nm^{-1}. Both sulfur mustard molecules moved through all regions within the total simulation time of 23.2 ns. In the case of heptane with a larger external force of 50 kJ mol^{-1} nm^{-1}, 1.5 cycles were obtained during a total simulation time of 28 ns.

Fig. 9 shows the permeation rate of different solutes at different external forces as the solutes average number of cycles per nanosecond. Below an external force of 50 kJ mol^{-1} nm^{-1} one can interpret results only qualitatively. At forces above 50 kJ mol^{-1} nm^{-1} sulfur mustard molecules are observed to cross the membranes at rates which are significantly higher than those of heptane. Both molecules exhibit a superlinear increase in the number of cycles as a function of the external force. The heptane curve appears to be shifted by 50 kJ mol^{-1} nm^{-1} to higher forces. This leads to a relative increase between the number of cycles of sulfur mustard with respect to that of heptane: about a factor of 3.7 at 50 kJ mol^{-1} nm^{-1}, 5.9 at 100 kJ mol^{-1} nm^{-1}, and 2.0 at 200 kJ mol^{-1} nm^{-1}.

For the force range applied, Fig. 9 clearly shows a non-linear relation between the magnitude of the external force and the resulting permeation rate. The calculations are outside the linear-response regime, and it is not possible to reliably extrapolate them to an external force of 0, which would be the natural (equilibrium) permeation rate of the two compounds. At forces small enough to be in the linear regime, there are no transition events on the timescale of the simulation. Notwithstanding, the simulations can help to identify the solute features most important for permeation. To this end, we have introduced unphysical modifications to the two molecules. We have constructed an uncharged sulfur mustard with all partial charges set to zero and all other force field parameters unchanged, as well as a charged heptane with the heptane force field parameters augmented by the charges from the sulfur mustard force field on the corresponding positions in the chain.

Charged and uncharged molecules of the same type perform (within error bars) the same number permeation events per nanosecond. Only for the strongest applied external force of 200 kJ mol^{-1} nm^{-1} we can see differences in the percent region between the charged and the uncharged molecules. Since except the atomic partial charges all parameters are the same and the charge is of minor importance, the different permeation rates of heptane and sulfur mustard are explained by density or free-volume considerations. The smaller molar volume (derived from the densities of the pure systems equilibrium simulations) of sulfur mustard (114 cm^3/mol for our model compared to 139 cm^3/mol for our heptane model, both at 300 K) leads to a faster penetration of the membrane.

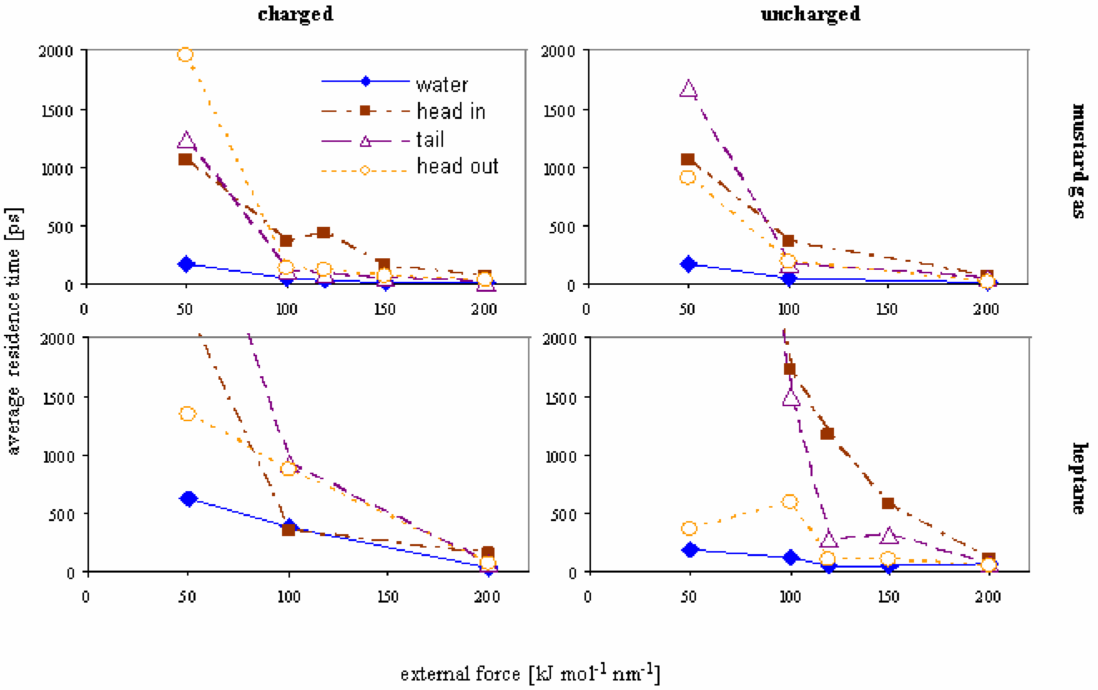

Fig. 10. Residence time of the solute molecules within the different compartments of the bilayer. The overall shorter residence times of sulfur mustard compared to the ones of heptane match with the general picture of more cycles per nanosecond, when an external force is applied. The unphysical solutes show that the partial charges on the beads help to penetrate the head group area.

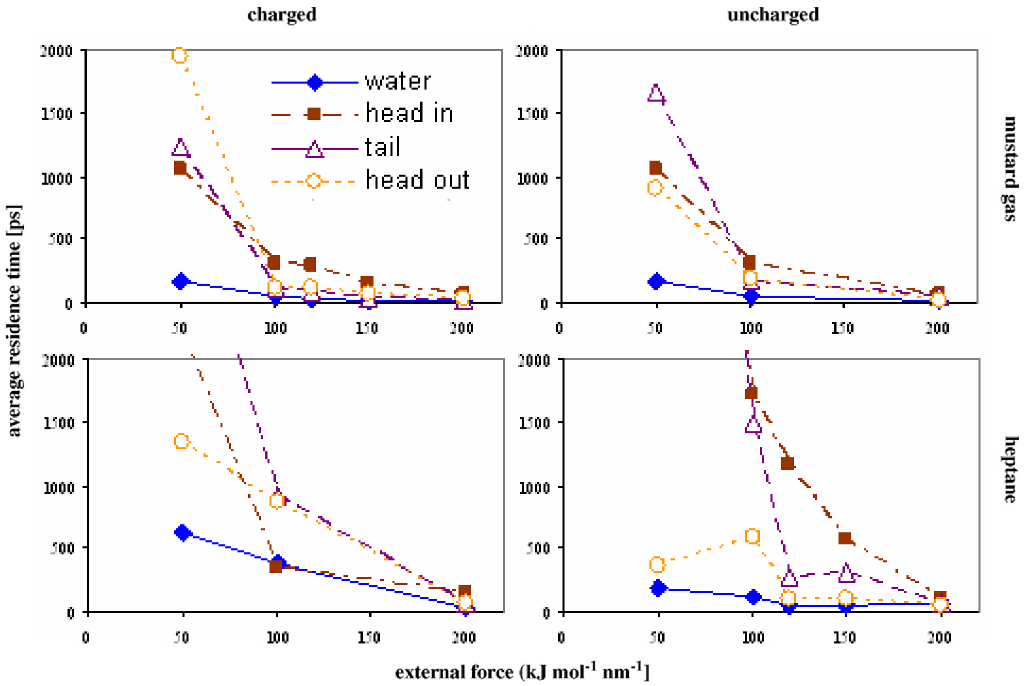

Fig. 11. Relative residence times of different solutes in the different regions of the membrane. The times are scaled so that the longest residence time becomes 1.

The average residence time of different molecules in the four regions of the membrane is shown in Fig. 10. Note that especially for the data at 50 kJ mol^{-1} nm^{-1} the statistics are limited. The shortest residence times of the solutes in all simulations are found in the water region, with its average thickness of $d_{\mathrm{water}} = 1.67$ nm. The residence times for all solutes are comparable, except for the charged heptane where they are approximately twice as big.

With different external forces, different regions become more important as obstacles for the solutes. Fig. 11 shows this in more detail. For each value of the external force, the longest residence time of all regions was normalized to 1 and all other residence times were scaled with the same factor. As we already observed in Fig. 10, the influence of the water phase is the weakest one but in the limit of high forces we find a relative increase of the importance of this region.

In these plots the importance of finding a way into the membrane, to penetrate the first head group (the "head-in" region with an average thickness of $d_{\mathrm{head\text{-}in}} = 1.23$ nm denotes the head-group region encountered by a solute entering the membrane from the water phase) becomes apparent, especially at big external forces. At small external forces the influence of other regions may take over. We can also see that this loss of importance of the head-in region is more pronounced for charged molecules than for the uncharged ones.

The most important observation lies in the comparison of the influence of the tail ($d_{\mathrm{tail}} = 2.86$ nm) and the head-out region ($d_{\mathrm{head\text{-}out}} = d_{\mathrm{head\text{-}in}} = 1.23$ nm), i.e. the head group region encountered when the solute leaves the membrane. Both residence times keep their relative order for all external forces in each subplot. For most molecules the tail region is always a stronger impediment to permeation than the head-out region. The exception is real, charged mustard for which the opposite is true. These molecules need more time to leave the membrane than to travel through its tail region. This coincides with the results of the equilibrium simulations which also indicated a higher mobility of the sulfur mustard within the membrane.

As an estimate for the diffusion coefficients perpendicular to the membrane D_{zz} in the different regions, we apply Eqs. (2) and (3) to runs with the best statistics, namely the runs with an external force of 200 kJ mol^{-1} nm^{-1}. For heptane we calculate $D_{zz}(\mathrm{water}) = 2.91 \times 10^{-6}$ cm^2/s, $D_{zz}(\mathrm{head\text{-}in}) = 1.39 \times 10^{-6}$ cm^2/s, $D_{zz}(\mathrm{tail}) = 5.49 \times 10^{-6}$ cm^2/s, and $D_{zz}(\mathrm{head\text{-}out}) = 3.48 \times 10^{-6}$ cm^2/s. For sulfur mustard the diffusion coefficients across the membrane regions are: $D_{zz}(\mathrm{water}) = 9.81 \times 10^{-6}$ cm^2/s, $D_{zz}(\mathrm{head\text{-}in}) = 2.11 \times 10^{-6}$ cm^2/s, $D_{zz}(\mathrm{tail}) = 1.58 \times 10^{-5}$ cm^2/s, and $D_{zz}(\mathrm{head\text{-}out}) = 5.40 \times 10^{-6}$ cm^2/s. The comparison of the diffusion coefficients of the molecules in water with the values obtained in equilibrium simulations (cf. Table 3) shows that the diffusion constant in the non-equilibrium simulations is smaller by a factor of 2 for sulfur mustard and 6.5 for heptane. Given that this estimation is based on equations for homogeneous systems, the agreement of the results is satisfactory. Three possible explanations can be found for the deviations in the diffusion coefficients. First, the inhomogeneity of the system through which the molecules have to travel causes regions of fast and slow diffusion. Especially when escaping from a region with slow diffusion, the molecule will take some time to reach the new net drift velocity in the new environment. This is a finite-size effect. Second, the distribution of the times required to penetrate a region is not symmetric. In simulations with high external forces the different penetration times of the many penetration cycles lead to a pronounced penetration time distribution. We observed in this distribution a long tail for longer penetration times and a short one for shorter penetration times (not shown here). This would be compatible with an approximate Poisson distribution of the residence times. The average residence time therefore tends to overestimate the most probable residence time. Both problems, which have a tendency to underestimate the diffusion constant, are expected to lose influence with decreasing external forces—for the price of poorer statistics. Third, it has to be kept in mind that, while a "diffusion coefficient" can be defined and calculated as a ratio of particle flux and external force, we are deep in the non-linear-response regime and the apparent diffusion coefficient can depend on the external force, see the discussion above.

The estimated diffusion coefficients nevertheless allow some insight in the transport of the solutes. We observe for both heptane and sulfur mustard a faster diffusion through the tail region (along the z axis) than in the xy plane. Even the penetration into the membrane at this external force shows a higher diffusion coefficient than the lateral diffusion coefficients of the solutes within the membrane. These numbers indicate again that the penetration processes at such extremely high external forces are fundamentally different from those at smaller or even vanishing external forces.

5. Conclusions

We demonstrated differences in the motion patterns of sulfur mustard and heptane molecules as they diffuse within and through DPPC bilayers. We showed that the way of penetration of the membrane by solutes must be different for the different molecules and at different external forces.

Sulfur mustard was observed to be the more flexible of the two species. It diffuses and reorients faster than heptane in the tail region of the membrane. Although the tail groups dictate the main orientation of both molecules their influence is smaller for sulfur mustard. This is also mirrored by the fact that, under an external driving force, the residence time of sulfur mustard in the tail region is shorter than the time the molecule needs to escape from the membrane through the head group region. The dynamical characteristics of sulfur mustard are due to a concerted effect of the partial charges and the smaller molecular volume. Only one of the two effects is not enough to reverse the order of the residence times as it is observed for heptane. For all these reasons we deduce that the obstacle to mustard penetration through a DPPC membrane is the head-group region encountered upon trying to leave the membrane into the water phase.

The behavior of heptane is different in many ways. It is much more confined by the tail groups while within the membrane. Its orientation is restrained and the diffusion is restricted by the cage formed by the lipid tails. This effect is so strong that even when an external force drags the molecule through the membrane, the residence time in the tail region dominates the one in the exit head-group region. This behavior is opposite of what is found for sulfur mustard. This observation is in agreement with the fact that heptane is soluble in apolar solvents but not in polar media (i.e. water and the head-groups). These results suggest that the tail groups are the limiting factor for heptane to penetrate the DPPC membrane.

Even though that the solubility of sulfur mustard in water is low (0.92 g/100 g H_2O at 22 °C [4]), it is still higher than that of heptane (2.7 ppm at 25 °C [44]). Our results support this general statement and show their consequences for the penetration of biological membranes.

Finally we have shown that in dragging solutes through the system by applying an external force, the barriers for the penetration process change their influence. At high forces (we tested up to 200 kJ mol^{-1} nm^{-1}), the solutes spend the most time trying to enter the membrane through the head group region. This process entails reorientation at the surface and finding or drilling a hole to slip through the network of membrane head groups. Reducing the external forces decreases the influence of this process. When forcing the molecules to stay close to the interface, they – in the course of time – find a gap in the constantly moving head-group layer and penetrate it. This process, compared to the brute force hole drilling at high external forces, is slower in absolute values, but faster in comparison of the residence times in the different regions of the membrane.

The present simulations are a first step in understanding the penetration process of sulfur mustard. Further investigations must aim for an improvement of the sulfur mustard force field. Especially optimizing the Lennard–Jones parameters (i.e. using the simplex algorithm as demonstrated lately for another molecules containing seven atoms [45]) to achieve better agreement with the density and a reparameterization of the force constants for angles and torsions, is important to increase the accuracy of the results. Results of longer simulations at external forces of less then 50 kJ mol^{-1} nm^{-1} may allow an extrapolation of the residence times to even lower forces. Since membranes are a patchwork of many components, comparisons of the behavior of sulfur mustard in membranes with different lipids can show preferred layers to penetrate.

Concluding, sulfur mustard and heptane are not only different in their chemical reactivity, but also in their physicochemical properties like diffusion and rotation. While these properties are still comparable in water, they become much more different in the heterogeneous and ordered environment of a membrane. Both the molecular volume (molar volume divided by Avogadro constant) and the charge distribution of the molecules have a determining influence on the permeation rate.

Acknowledgements

We thank Volker Weiss for many critical discussions, Michael Böhm for a not less critical reading of the manuscript and the Deutsche Forschungsgemeinschaft for financial support.

References

[1] R.J. Duchowic, J.A. Vilensky, Mustard gas: it's pre-World War I history, J. Chem. Educ. 84 (2007) 948–994.
[2] J.C. Harris, Gassed, Arch. Gen. Psychiatry 62 (2005) 15–18.
[3] OPC Conference of the States Parties C-12/6: Report of the OPCW on the Implementation of the Convention of the Prohibition of the Development, Production, Stockpiling and Use of Chemical Weapons and on Their Destruction in 2006, Declaration under Article III.
[4] J.A.F. Comption, Military Chemical and Biological Agents: Chemical and Toxicological Properties, The Telford Press, Caldwell, New Jersey, 1987.
[5] D.W. Riegle Jr., A.M. D'Amato, "The Riegle Report, U.S. Chemical and Biological Warfare-Related Dual Use Exports to Iraq and their Possible Impact on the Health Consequences of the Gulf War", United States Senate, 103d Congress, 2d Session, 1994.
[6] J. Borak, F.R. Sidell, Agents of chemical warfare: sulfur mustard, Ann. Emerg. Med. 21 (1992) 303–308.
[7] P.K. Shukla, P.C. Mishra, S. Suhai, Reactions of DNA bases with the anticancer nitrogen mustard mechlorethamine: a quantum chemical study, Chem. Phys. Lett. 449 (2007) 323–328.
[8] S. Wellert, H. Imhof, M. Dolle, H.J. Altmann, A. Richardt, T. Hellweg, Colloid Polym. Sci. 286 (2008) 417–426.
[9] H.J.C. Berendsen, S.-J. Marrink, Molecular dynamics of water transport through membranes: water from solvent to solute, Pure Appl. Chem. 65 (1993) 2513–2520.
[10] S.-J. Marrink, H.J.C. Berendsen, Simulation of water transport through a lipid membrane, J. Phys. Chem. 98 (1994) 4155–4168.
[11] B.L. de Groot, H. Grubmüller, Water permeation across biological membranes: mechanism and dynamics of Aquaporin-1 and GlpF, Science 294 (2001) 2353–2357.
[12] Amadeu K. Sum, Roland Faller, Juan J. de Pablo, Molecular simulation study of phospholipid bilayers and insights of the interactions with disaccharides, Biophys. J. 85 (2003) 2830–2844.
[13] C.S. Pereira, P.H. Hünenberger, Interaction of the sugars trehalose, maltose and glucose with a phospholipid bilayer: a comparative molecular dynamics study, J. Phys. Chem. B 110 (2006) 15572–15581.
[14] C.S. Pereira, R.D. Lins, I. Chandrasekhar, L.C.G. Freitas, P.H. Hünenberger, Interaction of the disaccharide trehalose with a phospholipid bilayer: a molecular dynamics study, Biophys. J. 86 (2004) 2273–2285.
[15] D.P. Tieleman, M.S.P. Sansom, H.J.C. Berendsen, Alamethicin helices in a bilayer and in solution: molecular dynamics simulations, Biophys. J. 76 (1999) 40–49.
[16] M. Pickholz, L. Saiz, M.L. Klein, Concentration effects of volatile anesthetics on the properties of model membrane: a coarse grain approach, Biophys. J. 88 (2005) 1524–1534.
[17] B.W. Lee, R. Faller, A.K. Sum, I. Vattulainen, M. Patra, M. Karttunen, Structural effects of small molecules on phospholipid bilayers investigated by molecular simulations, Fluid Phase Equilib. 225 (2004) 63–68.
[18] J.L. MacCallum, D.P. Tieleman, Interactions between small molecules and lipid bilayers, Curr. Top. Memb. 60 (2008) 227–256.

[19] Y. Wang, J. Cohen, W.F. Boron, K. Schulten, E. Tajkhorshid, Exploring gas permeability of cellular membranes and membrane channels with molecular dynamics, J. Struct. Biol. 157 (2007) 534–544.
[20] F. Müller-Plathe, YASP: a molecular simulation package, Comput. Phys. Commun. 78 (1993) 77–94.
[21] K. Tarmyshov, F. Müller-Plathe, Parallelizing a molecular dynamics algorithm on a multiprocessor workstation using OpenMP, J. Chem. Inf. Model. 45 (2005) 1943–1952.
[22] F. Müller-Plathe, Reversion the perturbation in nonequilibrium molecular dynamics: an easy ways to calculate the shear viscosity of fluids, Phys. Rev. E 59 (1999) 4894–4899.
[23] M.P. Allen, D.J. Tildesley, Computer Simulation of Liquids, Clarendon, Oxford, 1987.
[24] J.-P. Ryckaert, G. Ciccotti, H.J.C. Berendsen, Numerical integration of the Cartesian equations of motion of a system with constraints: molecular dynamics of alkanes, J. Comput. Phys. 23 (1977) 327–341.
[25] H.J.C. Berendsen, J.P.M. Postma, W.F. van Gunsteren, A. DiNola, J.R. Haak, Molecular dynamics with coupling to an external bath, J. Chem. Phys. 81 (1984) 3684–3690.
[26] F. Müller-Plathe, S.C. Rogers, W.F. van Gunsteren, Gas sorbtion and transport in polybutylene: equilibrium and nonequilibrium molecular dynamics simulations, J. Chem. Phys. 98 (1993) 9895–9904.
[27] D.J. Evans, J.P. Moriss, Statistical Mechanics of Nonequilibrium Liquids, Academic Press, London, 1990.
[28] I. Chandrasekhar, M. Kastenholz, R.D. Lins, C. Oostenbrink, L.D. Schuler, D.P. Tielemann, W.F. van Gunsteren, A consistent potential energy parameter set for lipids: dipalmitoylphosphatidulcholine as a benchmark of the GROMOS96 45A3 force field, Eur. Biophys. J. 32 (2003) 67–77.
[29] W.F. van Gunsteren, S.R. Billeter, A.A. Eising, P.H. Hünenberger, P. Krüger, A.E. Mark, W.R.P. Scott, I.G. Tironi, Biomolecular Simulation: The GROMOS96 Manual and User Guide, VDF, Zürich, 1996.
[30] CRC Handbook of Chemistry and Physics, 73rd ed., CRC Press, London, 1992–1993.
[31] M.J. Frisch, G.W. Trucks, H.B. Schlegel, G.E. Scuseria, M.A. Robb, J.R. Cheeseman, J.A. Montgomery Jr., T. Vreven, K.N. Kudin, J.C. Burant, J.M. Millam, S.S. Iyengar, J. Tomasi, V. Barone, B. Mennucci, M. Cossi, G. Scalmani, N. Rega, G.A. Petersson, H. Nakatsuji, M. Hada, M. Ehara, K. Toyota, R. Fukuda, J. Hasegawa, M. Ishida, T. Nakajima, Y. Honda, O. Kitao, H. Nakai, M. Klene, X. Li, J.E. Knox, H.P. Hratchian, J.B. Cross, C. Adamo, J. Jaramillo, R. Gomperts, R.E. Stratmann, O. Yazyev, A.J. Austin, R. Cammi, C. Pomelli, J.W. Ochterski, P.Y. Ayala, K. Morokuma, G.A. Voth, P. Salvador, J.J. Dannenberg, V.G. Zakrzewski, S. Dapprich, A.D. Daniels, M.C. Strain, O. Farkas, D.K. Malick, A.D. Rabuck, K. Raghavachari, J.B. Foresman, J.V. Ortiz, Q. Cui, A.G. Baboul, S. Clifford, J. Cioslowski, B.B. Stefanov, G. Liu, A. Liashenko, P. Piskorz, I. Komaromi, R.L. Martin, D.J. Fox, T. Keith, M.A. Al-Laham, C.Y. Peng, A. Nanayakkara, M. Challacombe, P.M.W. Gill, B. Johnson, W. Chen, M.W. Wong, C. Gonzalez, J.A. Pople, Gaussian 03 Revision B. 01, Gaussian, Inc., Pittsburgh, PA, 2003.
[32] H.J.C. Berendsen, J.R. Grigera, T.P. Straatsma, The missing term in the effective pair potentials, J. Phys. Chem. 91 (1987) 6269–6271.
[33] Z.V. Leonenko, E. Finot, H. Ma, T.E.S. Dahms, D.T. Cramb, Investigation of temperature-induced phase transition in DOPC and DPPC phospholipid bilayers using temperature controlled scanning force microscopy, Biophys J. 86 (3783) (2004) 3783–3793.
[34] S. Tristram-Nagle, T. Moore, H.I. Petrache, J.F. Nagle, Specific volumes of lipids in fully hydrated bilayer dispersions, Biochim. Biophys. Acta 938 (1988) 135–142.
[35] J.F. Nagle, S. Tristram-Nagle, Structure of bilayers, Structure of lipid bilayers, Biochim. Biophys. Acta 1469 (2000) 159–195.
[36] S. König, W. Pfeiffer, T. Bayerl, D. Richter, E.J. Sackmann, Molecular dynamics of lipid bilayers studied by incoherent quasi-elastic neutron scattering, J. Phys. II France 2 (1992) 1589–1616.
[37] R. Lipowski, E. Sackmann, Structure and Dynamics of Membranes, Elsevier, Amsterdam, 1995.
[38] P.F.F. Almeida, W.L.C. Vaz, T.E. Thompson, Lateral diffusion in the liquid phases of dimyristoylphosphatidylcholine/cholesterol lipid bilayers: a free volume analysis, Biochemistry 31 (1992) 6739–6747.
[39] J. Vijande, J.J. Piñeiro, J. García, J.L. Valencia, J.L. Legido, Density and surface tension variation with temperature for heptane + 1-alkanol, J. Chem. Eng. Data 51 (2006) 1778–1782.
[40] Report on Carcinogens, 11th ed., U.S. Department of Health and Human Services, Public Health Service, National Toxicology Program, 2005.
[41] M. Glukhovtsev, R.D. Bach, C.J. Nagel, A high-level computational study of the thermochemistry and thermal decomposition of sulfur mustard (2,2′-dichlorethyl sulfide): chemical warfare agent, J. Phys. Chem. A 102 (1998) 3438–3446.
[42] G.L. Butterfoss, J. Hermans, Boltzmann-type distribution of side-chain conformation in proteins, Protein Sci. 12 (2003) 2719–2731.
[43] S. Wolfe, D.F. Weaver, K. Yang, MMPEP: development and evaluation of peptide parameters for Allinger's MMP2(85) programme, including calculations of crambin and insulin, Can. J. Chem. 66 (1988) 2687–2702.
[44] C. Tsonopoulos, Thermodynamic analysis of the mutual solubilities of normal alkanes and water, Fluid Phase Equilib. 156 (1999) 21–33.
[45] T.J. Müller, S. Roy, W. Zhao, A. Maaß, D. Reith, Economic simplex optimisation for broad range property prediction: strengths and weaknesses of an automated approach for tailoring of parameters, Fluid Phase Equilib. 274 (2008) 27–35.

4.2. Impulstransport: Scherviskosität von DPPC Membranen

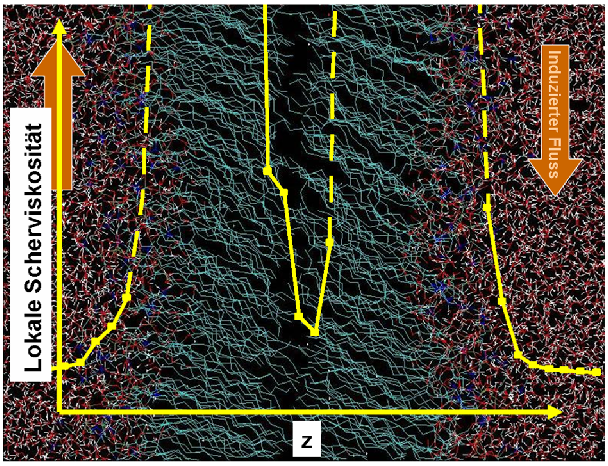

Abb. 4: Das Profil der lokalen Scherviskosität durch eine Dipalmitoylphosphatidylcholin-membran.

Eine der Konsequenzen des in den siebziger Jahren von Singer und Nicolson eingeführten Flüssig-Mosaik-Modells [33] zur Beschreibung von Membranen ist, dass Membranen heutzutage bis zu einem gewissen Grad als zweidimensionale Flüssigkeiten verstanden werden. Konsequenzen daraus sind nicht nur die Diffusion von einzelnen Lipidmolekülen im Netzwerk einer Monoschicht, sondern auch die strukturelle Adaption an äussere Kräfte; z.B. beim Biegen der Membran, wenn sie in eine Pipette gesaugt wird [34]. Ebenfalls reagiert die Membran auf Schereinflüsse, so dass im Experiment [35-37] und in Berechnungen [38,39] versucht wurde, Scherviskositäten verschiedener Membranen zu bestimmen. Die Ergebnisse unterscheiden sich aber um Grössenordnungen. Mit einer neuen Berechnungsmethode und einem genaueren Modell wird die folgende Untersuchung die Diskrepanz zwischen Messwerten und theoretisch berechneten Werten für die Scherviskosität vermindern.

Zwei Verbesserungen wurden im Vergleich zu schon bestehenden Untersuchungen von Shkupila et. al. [38] eingeführt:

Zum einen verwenden wir eine genauere und dementsprechend rechenintensivere Beschreibung des Membransystems. Während zuvor die Lipidmoleküle durch wenige Superatome angenähert wurden („coarse grained“ Ansatz), vereinfachen wir das System nur indem wir die Wasserstoffatome mit Kohlenstoffatomen zusammenfassen („united atoms“ Ansatz). Die gewonnene Genauigkeit des Modells führt zu mehr Freiheitsgraden der Lipide und mehr Verschlaufung der einzelnen Schwanzgruppen.

Zum anderen kommt in unserem Falle die „reverse non-equilibrium molecular dynamics“ Methode zum Einsatz. [40] Da im Gegensatz zu anderen Algorithmen bei dieser Methode der Impulsfluss durch das System induziert wird (und deshalb genau bekannt ist), kann der daraus entstehende Geschwindigkeitsgradient räumlich aufgelöst werden. Dies erlaubt schließlich die Definition einer lokalen Scherviskosität, die wiederum eine räumliche Auflösung der Viskosität in der Membran erlaubt.

Mit diesen Neuerungen können wir zeigen, dass die theoretisch berechneten Resultate, in die Richtung der experimentell ermittelten korrigiert werden können. Die Details dieser Studie wurden im Journal ChemPhysChem 10 (2009) 2305-2315 veröffentlicht.

Determining the Local Shear Viscosity of a Lipid Bilayer System by Reverse Non-Equilibrium Molecular Dynamics Simulations

Thomas J. Müller* and Florian Müller-Plathe[a]

The parallel shear viscosity of a dipalmitoylphosphatidylcholine (DPPC) bilayer system is studied by reverse non-equilibrium molecular dynamics simulations (RNEMD) with two different united-atom force fields. The results are related to diffusion coefficients and structural distributions obtained by equilibrium molecular simulations. We investigate technical issues of the algorithm in the bilayer setup, namely, the dependence of the velocity profiles on the imposed flux and the influence of the thermostat on the calculated shear viscosity. We introduce the concept of local shear viscosity and investigate its dependence on the slip velocity of the monolayers and the particle density at the headgroup–water interface and the tail–tail interface. With this we demonstrate that the lipid bilayer is more viscous than the surrounding water phase, and that slip takes place near the headgroup region and in the centre of the bilayer where the alkyl tails meet. We also quantify the apparent increase in viscosity of the water molecules entangled at the water–headgroup interface.

1. Introduction

Through the last century, the model of biological membranes changed several times. One of the major changes was the concept of the fluid mosaic model introduced by Singer and Nicolson in the early seventies.[1] Up to that point, biological membranes were just considered locally flat, self-assembled aggregates of amphiphilic molecules where each molecule consists of a hydrophilic headgroup and a hydrophobic tail group.[2] Since this structure is only held together by weak nonbonded interactions, the Singer–Nicolson model assigns to the lipid-bilayer component of membranes a certain degree of fluidity. This picture of a two-dimensional fluid in a three-dimensional solvent matrix explains why membranes are so susceptible to external forces, such as deformations of vesicles sucked into a pipette.[3] In spite of this fluidity, which implies a certain degree of randomness, the many-body nature of the molecular assembly of the membrane ensures local order and structure development. In view of this model, experimental[4–6] and theoretical investigations[7] have been carried out on the rheological properties of membranes.

One of the tools for these investigations is molecular dynamics. Although the calculations are limited in system size and accessible time scale by the computational resources and in accuracy by the force field used to describe the system,[8] they can offer insight into membrane structure and dynamic properties, which are very difficult or impossible to obtain experimentally. Shearing and the associated viscosity coefficients are such properties because interlayer shearing and intralayer shearing (Figure 1) intermix with each other, and because experimentally simultaneously occurring dynamical processes such as bending, stretching, and relaxation lead to even more uncertainty.[4,9]

Recently, Shkulipa et al.[7,10] studied shear effects with different coarse-grained models. They specified the characteristics of the shear flow using Lees-Edwards boundary conditions.[11,12] They found that the surface viscosity and the interlayer friction of the coarse-grained model were too large, by two to three orders of magnitude. In contrast, we apply reverse non-equilibrium molecular dynamics simulation to a dipalmitoylphosphatidylcholine (DPPC) bilayer to study the effects of shear in molecular detail. For other systems, such as polymers and ionic liquids, it has also been found that coarse-grained models may easily lead to a too high molecular mobility and, hence, an underestimation of the viscosity.[13,14] Therefore, in this work an atomistic model has been employed.

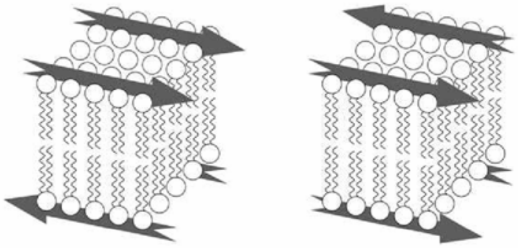

Figure 1. Scheme of inter- (left) and intra- (right) monolayer shearing. Interlayer shearing results from a parallel flow of lipids within a monolayer whereas intralayer shearing results from a perpendicular flow within the monolayers.

---

[a] *T. J. Müller, Prof. Dr. F. Müller-Plathe*
Theoretische Physikalische Chemie
Eduard-Zintl-Institut für Anorganische und Physikalische Chemie
Technische Universität Darmstadt
Petersenstrasse 20, 64287 Darmstadt (Germany)
Fax: (+49)6151 166526
E-mail: t.mueller@theo.chemie.tu-darmstadt.de

2. Methods

In the limit of linear response theory, the shear viscosity η is the proportionality constant between an applied shear field and a resulting flux of transverse linear momentum [resisting force per area, Eq. (1)]:

$$j_z(p_x) = -\eta \frac{\partial v_x}{\partial z} \tag{1}$$

The momentum flux $j_z(p_x)$ is defined as the amount of x component of the momentum p_x transported in the z direction per time unit, whereas the shear rate is the gradient $\partial v_x/\partial z$ in the z direction of the x component of the mean flow velocity.

To calculate the shear viscosity, the so-called reverse non-equilibrium molecular dynamics method[15] has been applied, which is described here only briefly (for details see references [15, 16]):

- Divide virtually the simulation box along the z axis into n slabs of equal thickness.
- Run a molecular dynamics (MD) simulation. Every m simulation steps look in the first slab (number 1) for the atom with the largest (positive) p_x component and in the central slab (number $n/2+1$) for the atom with the lowest (most negative) p_x component. Exchange these p_x components if the two atoms have the same mass.
- During the MD simulation, this non-equilibrium procedure will build up a steady-state velocity gradient, which can be evaluated. The momentum flux is calculated by summing up the exchanged momentum and dividing it by the simulation time t and the xy area of the box defined by L_x (the box length in the x direction) and L_y (the box length in the y direction), as shown in Equation (2):

$$j_z(p_x) = \sum_{\text{exchanges}} \frac{p_{x,\text{middle}} - p_{x,\text{first}}}{2tL_xL_y} \tag{2}$$

Herein, the molecular exchange algorithm has been used, which exchanges the centre-of-mass velocities of water molecules.[16] As momentum is conserved, the physical momentum transport (friction in the membrane) has to equal the unphysical transport (momentum swaps) in the steady state.

Treating an inhomogeneous system with several different media needs additional attention. The viscosity can be locally varying, whereas the overall imposed momentum flux on the system is known and the same everywhere. This leads to a velocity gradient, which varies along the z direction. Therefore, the apparent local shear viscosities (e.g. in the water phase, in the head group region, in the center of the membrane) can be separately obtained and compared. The η_i, the viscosities of each of the subparts of the system, are obtained in one single simulation from the overall imposed flux $j_z(p_x)$ and the locally observed gradient $(\partial v_x/\partial z)_i$ in the subsystem [Eq (3)]:

$$\eta_i = -j_z(p_x)/\left(\frac{\partial v_x}{\partial z}\right)_i \tag{3}$$

It should also be noted that the RNEMD algorithm conserves the total energy of the system.[15] In contrast to other NEMD methods, it does not require a cooling thermostat. Thermostats may, however be necessary for other reasons, such as to counterbalance the heating due to cutoff noise. For this reason, we study their effect on the apparent shear viscosity. A previous study on the viscosities of molecular fluids showed that the Berendsen thermostat and manostat with common settings of their control parameters had no significant influence on the calculated viscosities.[17]

3. Computational Details

All simulations were performed with the MD package YASP.[18] Within it, the RNEMD algorithm has been implemented and extensively tested for model (Lennard-Jones) fluids[15] and molecular fluids.[16] YASP works with the leap frog algorithm as the integrator, uses orthorhombic boundary conditions, and Berendsen thermostat and manostat for temperature and pressure control. Bond constraints were enforced by the SHAKE algorithm.[11] A reaction-field approximation has been used for the electrostatic interactions.

As force field parameters for the phospholipids, the GROMOS 96 parameter set 45A3[19] has been chosen. This united-atom force field was developed starting from alkanes and was also tested on a DPPC[20] bilayer. It parameterizes the hydrogen atom within the carbon atoms leading to CH, CH_2 and CH_3 superatoms. All other atoms are treated explicitly. It was shown that by choosing the right simulation parameters (e.g the reaction field of this system is $\varepsilon_{RF}=54$, see ref. [20]), the headgroup area, the chain-order parameters, and the lateral diffusion coefficient were in accordance with the experimental data. Since the GROMOS package and the YASP package have almost the same potential description, force field parameters are directly transferable. Only the term of the dihedral angle torsion energy is not divided by the factor of 2 in the GROMOS force field, while YASP does this scaling [Eq. (4)]:

$$V_{\text{Torsions}} = \Sigma_{\text{Torsions}}(k_\phi/2)[1-\cos p(\tau-\tau_0)] \tag{4}$$

To investigate the impact of the torsion potential on the shear viscosity and possibly linked properties such as density and diffusion coefficients, two different subsets of the GROMOS force field have been studied:

- In force field 1, all the force constants were copied form GROMOS 45A3 and transformed into YASP units. This introduces torsional barriers which are too low by a factor of 2. Some of the technical comparisons, consistency check, and setup simulations were done with this force field and are reported here.
- In force field 2, this error has been corrected and the torsions have the correct barrier heights. All final results were

calculated with this force field. The full tables of all interaction parameters can be found in ref. [21].

For water, the simple point charge (SPC/E) model[22] has been chosen because it was the water model the transferred lipid force field was parameterized with.

3.1. Equilibrium Simulations

3.1.1. *Preparation*

The simulation box was built from scratch. In a first step, the bilayer was formed by arranging eight by eight all-*trans* DPPC molecules side by side on the *xy* plane at the experimentally expected area-per-headgroup ratio. This monolayer was mirrored with respect to the *xy* plane and added to the first one with a distance between the tail ends of 0.2 nm. On top and on bottom of this bilayer two water layers with 1827 and 1828 water molecules, positioned on an almost filled 20×20×5 grid, were placed with a distance of approximately 0.2 nm to the lipid bilayer.

The preparation runs were performed with force field 1. The system was allowed to compact in a first series of short constant-pressure runs. The cutoff was set to 0.8 nm, the neighbor list cutoff to 0.9 nm, and an initial and target temperature 325 K with a coupling time of 0.2 ps. During these ten runs, the number of time steps per run was increased from 10 to 1000, while the step size itself was increased from 2×10^{-7} to 2×10^{-3} ps. The target pressure for the diagonal pressure control was always set to 101.3 kPa and the coupling time to 0.5 ps. The literature value of the system compressibility[20] (of 2.77×10^{-7} kPa^{-1} in each direction) was partially reduced by a factor of up to ten to dampen volume fluctuations and prevent resulting SHAKE failures. After every run, all velocities were re-initialized according to the target temperature. The reaction field dielectric constant was set to one for this set of preparatory simulations.

After another simulation of 120 ps with a reaction-field dielectric constant of one, but a neighbor list cutoff of 1.0 nm, the dielectric field constant was increased to 54, the reference value for the lipid force field.[19] With these changes, the preparation phase was over and the actual equilibration started.

3.1.2. *Equilibration of the System with Force Field 1*

Over the first 3 ns, the total energy and the box size decreased by 0.23 and 1 %, respectively. During the following 3 ns, they only decreased by 0.002 % and 0.18 %, respectively. Since both values changed less than 0.1 % over the next 2 ns of simulation time, the system was considered equilibrated.

For the production runs, the cutoff radii were adjusted again. The full set of simulation parameters for the production run was the following: the cutoff radius was set to 1.2 nm, the neighbor list had a cutoff of 1.4 nm and was updated every 15 steps. A time step equaled 2 fs. The target temperature of 325 K was coupled with a temperature coupling time of 0.2 ps while the diagonal pressure control (separate coupling for the box lengths L_x, L_y, L_z) target pressure was 101.3 kPa with a compressibility of 2.77×10^{-7} kPa^{-1} and a coupling constant of 0.5 ps in each direction. The reaction field dielectric constant was 54.

3.1.3. *Equilibration of the System with Force Field 2*

The equilibration started form the coordinates obtained after the first 2 ns of the equilibration of the system with force field 1. Further 1000000 time steps with a step size of 2 fs were performed for a total simulation time of 2 ns. The control parameters were set in the same way as those for force field 1, except that for computational speed the cutoff was set to 0.8 nm with a neighbor list cutoff of 1.0 nm. The total energy, density, and area per headgroup fluctuated around their mean values. No drift in these properties was observable. Thus, the equilibration was considered finished.

3.2. Non-Equilibrium Simulations

Since the reverse non-equilibrium molecular dynamics (RNEMD) algorithm exchanges velocities in two slabs, there are several consequences. One is the necessity of two membranes in a simulation box. The reason for this is the periodicity of the system and the fact, that only the velocities between two similar particles can be exchanged. These should be water molecules. There must be two water phases (separated from each other by two membranes) to make the system symmetric, so that in steady state the momentum fluxes in both directions are equal (see Figure 2).

3.2.1. *Preparation*

To build this system, an equilibrated frame of the equilibrium system described in Section 3.1.3 was duplicated, shifted by one box length in *z* direction and merged with the original

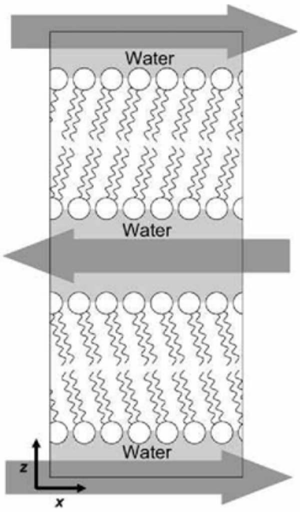

Figure 2. Scheme of simulation for reverse non-equilibrium molecular dynamics. The *z* axis was defined perpendicular to the membrane plane. The shear flow was applied along the *x* direction.

box. A very short equilibrium simulation of 22 ps with a step size of 2 fs followed to check that the system was still equilibrated. The cutoff radius was 0.9 nm while the neighbor list cutoff was set to 1.0 nm with an update rate of 15 time steps. The temperature was coupled to 325 K with a coupling constant of 0.2 ps. The simulation was conducted at constant *NVT* conditions.

After this equilibration, RNEMD was started. The master simulation, which ran for more than 7.3 ns, had the following parameters: The cutoff radius was set to 0.9 nm, while the neighbor list had a cutoff of 1.1 nm and was updated every 15 steps. The time step was 2 fs. With a coupling time of 0.2 ps, the temperature was held at 325 K. The reaction field dielectric constant was set to 54. The additional parameters for the non-equilibrium part were the exchange rate for a single momentum exchange, every 150 time steps (every 0.3 ps), and the write-out rate for the profiles (mean center of mass within each slab, mean flow velocity in each slab, temperature in each slab, and density in each slab) and the instantaneously calculated values (flux, gradient, viscosity)—both of which were set to 151 time steps to avoid systematic errors. The number of slabs was 20 for the master simulation or 80, when more resolution was desired, see below. The steady state is considered established in the first 1 ns of this run.

Velocity profiles of preliminary tests of consecutive 1 ns runs (results not shown here) indicate that while the shape of the profile is conserved the split velocity is fluctuating. This property follows no trend but exhibits a stochastic distribution. We see no indication for potential transients. Therefore the only requirement to get the correct velocity profile is to sample for a long enough time.

3.2.2. *Simulations with Force Field 1*

To investigate the influence of the different simulation parameters on the final result, a series of preliminary experiments has been designed. These simulations varied some of the parameters.

In a first series, different exchange intervals for every 50 (0.1), 100 (0.2), 150 (0.3), and 250 (0.5 ps) are applied, which also cause different periods for writing out the profiles and values: 51, 101, 151 and 251.

The second series varies the coupling time for the thermostat from 0.1 ps over 0.2, 0.4, and 0.8 ps to 1.6 ps. This series is carried out at an exchange interval of every 100 time steps, which induces write out periods for values and profiles of 101 time steps (write-out every 101 time steps).

The last series tests the influence of the manostat. These simulations are carried out under isothermal-isobaric conditions (NPT), by applying a diagonal pressure control with target pressure of 101.3 kPa, a compressibility of 2.77×10^{-7} kPa^{-1}, and a coupling constant of 0.5 ps in all directions. Analogously to the first series, exchange periods of 50, 100, 150 and 250 time steps have been simulated.

All three series take the last output frame of the equilibrium part of the master simulation as a starting point. The time to reach the steady state of all these runs is 1 ns before a 2 ns production run is executed.

3.2.3. *Simulations with Force Field 2*

For the dependence of the system under constant NVT conditions on the coupling parameters, simulations with force field 2 were performed. They were started from the final output coordinates of the RNEMD runs with force field 1 under the same simulation conditions as mentioned above. Five consecutive blocks of 1 ns each were calculated leading to a total simulation time of 5 ns of which the first 2 ns were considered necessary for reaching the steady state, so the production run lasted 3 ns.

4. Results and Discussion

4.1. Characterization of the Equilibrium Properties of the System

4.1.1. *Area per Lipid*

To establish benchmarks for the properties of the system, equilibrium MD simulations were performed. The major criterion for equilibration was a stable mean area per headgroup, which was directly calculated by dividing the product of the box length in the *x* (L_x) and *y* (L_y) directions by the number of lipid molecules per monolayer [Eq. (5)]:

$$A = L_x L_y / 64 \tag{5}$$

Figure 3 shows the variation of the area per head group for the simulation with force field 2. This leads to an estimate for the area per headgroup of 0.585($\pm$0.006) nm^2 for this simulation.

Several runs for the different force fields with different cutoff radii were executed. The results are summarized in Table 1; they were obtained from production runs with a duration of 3 to 5 ns. In comparison with the range of experimentally report-

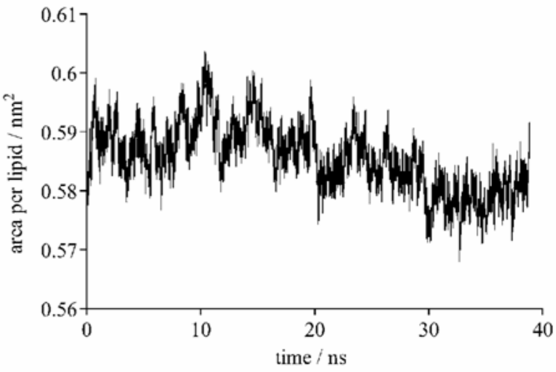

Figure 3. Area per headgroup of the membrane during the MD simulation. The area per lipid during the simulation with force field 2 has a mean value of 0.585 nm$^2\pm$0.006 nm^2. Simulations with force field 1 under the same simulation conditions showed an area per lipid of 0.568 nm$^2\pm$0.002 nm^2. The area per lipid for the simulations with force field 2 lies within the reported boundaries of the experimental values.[23]

Table 1. Dependence of the area per lipid on cutoff and force field.

Simulation	Area per lipid [nm^2]	Force field	Cutoff [nm][a]
1	0.536 ± 0.008	1	1.0
2[b]	0.547 ± 0.003	1	1.0
3	0.568 ± 0.002	1	0.8
4	0.564 ± 0.006	2	1.2
5	0.573 ± 0.006	2	1.0
6	0.585 ± 0.006	2	0.8

[a] The cutoff for building the neighbor list was always 0.2 nm greater than the interaction cutoff. [b] This simulation was started under the same conditions as simulation 1. The only difference was that the velocities in the input file were reassigned according to the target temperature.

ed data,[23] which starts at 0.57 nm^2 and ends at 0.64 nm^2, the results of force field 1 are too small, while the results of force field 2 lie within the reported boundaries. The influence of doubling the force constants for torsion potential thus leads to an increase in the area per lipid of 3 to 5%.

A comparison of the simulations with respect to the cutoff radius shows a steady increase of the area per lipid with decreasing cutoff radius. As discussed by Anézo et al.,[24] there is a non-negligible influence of the long range forces within membrane systems. Both force fields show the closest area per lipid value to the GROMOS reference value of 0.61 nm at the smallest tested cutoff radius of 0.8 nm.

But even at 0.8 nm, the area per lipid value found with force field 2 deviates by 5% from the reported one. This discrepancy is probably due to the differences of the treatment of electrostatics: GROMOS uses a charge group model for treating cutoff radii,[25] while YASP just uses atomic cutoffs together with a reaction field correction.

4.1.2. *Membrane Density Profile*

Another structural characteristic is the distribution of atoms within the membrane. Figure 4 shows the density distribution across the bilayer averaged over the whole simulation with force field 2 (Figure 4a mass density, Figure 4b particle density or atoms per slab). Special atomic groups are identifiable so that the thickness of the membrane, the distance between the peaks of the characteristic headgroups (phosphorus, nitrogen), can be estimated to be 3.83 nm. This length is comparable to the values of 3.6 nm measured by AFM cross-section at 50 °C by Leoneko and co-workers[26] and 3.87 nm measured by X-ray diffraction for the head-to-head distance by Tristram-Nagle and co-workers.[27] These values correspond to a fluid phase.

For the gel phase (experimentally observed at 20 °C) a head-to-head distance of 4.42 nm was measured by X-ray diffraction. The result of the head-to-head distance in the simulation with force field 1 is 4.37 nm. This finding is in agreement with the results from the area per headgroup. The system is denser packed in the *xy* plane than with force field 2 and this packing leads to an elongation in the perpendicular *z* direction.

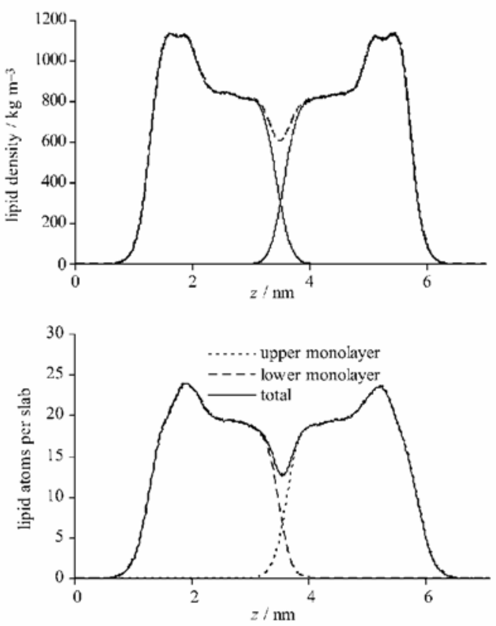

Figure 4. Density and particle density profile of the membrane. A) In the density profile of the bilayer system obtained from simulation with force field 2, certain features of the monolayers (——) can be identified. The outer subpeaks of the big double peaks at 1.65 and 5.45 nm belong to the phosphate groups whereas the inner two belong to the carbonyl groups in the tails. The total density (----) between the layers drops to 615 kg m^{-3} although the layers interfere with each other over a distance of 1 nm. This region is of the size of four hydrocarbon groups in each layer. B) Number of atoms per slab of 0.01418 nm thickness.

4.1.3. *Self-Diffusion*

Within Einstein diffusion limits, the translational diffusion coefficient of particles in a system with dimensionality *d* can be calculated from their mean square displacement [Eq. (6)]:

$$D = \lim_{t \to \infty} \frac{1}{2dt} \langle |\delta r(t)|^2 \rangle \tag{6}$$

The mean square displacement $\langle |\delta r(t)|^2 \rangle$ is defined by Equation (7):

$$\langle |\delta r(t)| \rangle = \langle |r(t) - r(0)|^2 \rangle \tag{7}$$

where $r(t)$ denotes the position of a particle at time t. For lipids bilayers, $d = 2$: The lateral diffusion coefficient D_t^{lat} and $r(t)$ only depends on the in-plane coordinates $x(t)$ and $y(t)$. To calculate the diffusion coefficients D_{xx} and D_{yy} along one of the in-plane axes [only depending on $x(t)$ or $y(t)$], the dimensionality becomes $d = 1$.

Figure 5 depicts the mean-square displacements of the lipids in all three spatial directions for the simulation after equilibration. The displacement in *z* direction goes to saturation as expected and is not considered any further. To calculate the diffusion coefficient from the mean-square displacement, the slope of the displacement is evaluated from 0.7 to 4.3 ns of a total of 20 ns to ensure sufficient statistics and Einsteinian behavior. This leads to direction-specific diffusion coefficients

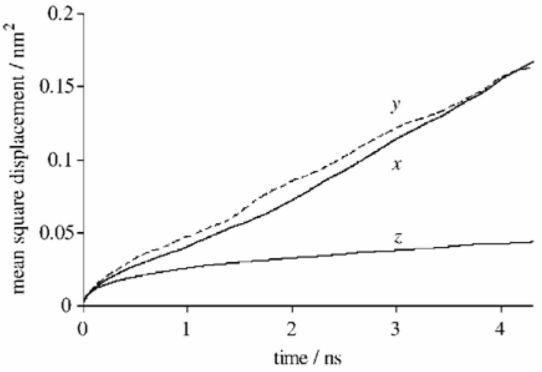

Figure 5. Mean square displacement in the different axial directions of all phosphorus atoms in the headgroups of the DPPC molecules in the equilibrium simulations carried out with force field 2. The results for times longer than 4.3 ns are not statistically well defined and are thus not plotted. Neglecting also the non-Einstein regime below 0.7 ns leads to diffusion coefficients of $D_{xx}=1.91\times10^{-7}$ cm^{2}s and $D_{yy}=1.79\times10^{-7}$ cm^{2}s within the lipid plane and an apparent diffusion coefficient $D_{zz}=2.77\times10^{-8}$ cm^{2}s perpendicular to it. Diffusion in the *z* direction is clearly non-Einsteinian.

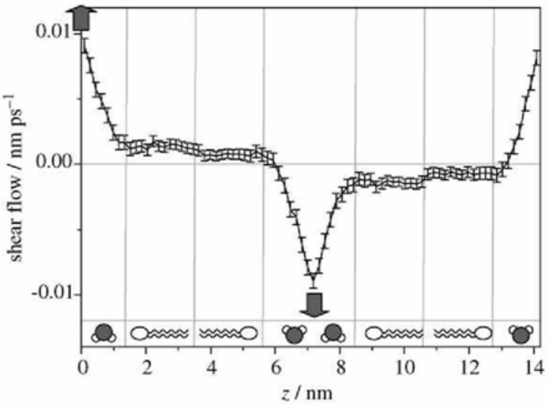

Figure 6. Average velocities in the shear direction of all the atoms in one slab. The different parts of the velocity profile in RNEMD simulations with force field 2 and an exchange period of 0.4 ps at a resolution of 80 slabs in the *z* direction are mapped to the mean distributions of different species in the *z* direction of the system (indicated schematically at the bottom of the figure; for an assignment to slabs, see Table 2).The error bars correspond to the standard deviation of the *z* component of the velocities of all the atoms in a slab over the whole simulation.

for the system with force field 2: $D_{xx}=1.91\times10^{-7}$ cm^{2}s^{-1}, $D_{yy}=1.79\times10^{-7}$ cm^{2}s^{-1}, and an average lateral diffusion coefficient of $D_t^{\mathrm{lat}}=1.85\times10^{-7}$ cm^{2}s^{-1}. The same procedure for force field 1 leads to $D_{xx}=3.6\times10^{-8}$ cm^{2}s^{-1}, $D_{yy}=7.8\times10^{-8}$ cm^{2}s^{-1}, and an average lateral diffusion coefficient of $D_t^{\mathrm{lat}}=5.7\times10^{-8}$ cm^{2}s^{-1}. Two characteristics can be pointed out: 1) For the more dense system of force field 1, the simulation time of 20 ns is not long enough to get the same diffusion coefficient in both planar directions. 2) The diffusion coefficient is three times as large when doubling the torsion force constant, most likely due to the lower lateral packing (larger headgroup per surface area).

The range of reported experimental data varies for this temperature between 10×10^{-8} cm^{2}s^{-1} in QENS experiments[29,30] at $T=333$ K and 13×10^{-8} cm^{2}s^{-1} in FRAP experiments[31] at $T=323$ K. While D_t^{lat} of force field 2 is a factor of 1.5–2 larger than the experimental data, D_t^{lat} of force field 1 is a factor of 2–2.5 smaller.

4.2. Non-Equilibrium Molecular Dynamics Simulations: Shear

4.2.1. Consistency Checks and Preliminary Results

Velocity Profiles: Applying reverse non-equilibrium molecular dynamics simulations, the system builds up a profile of the flow velocity. This makes it possible to assess the flow properties in different regions of the water–membrane system. A simplified picture in the literature[10] divides the membrane into four different regions. The upper water phase with the velocity profile showing a constant slope and the upper lipid layer with all the same velocity. After a jump in velocity there is the lower lipid layer at constant velocity and the lower water phase with a constant velocity gradient again.

Figure 6 maps the average flow velocities in a simulation of 5 ns with force field 2 at an exchange period of 100 time steps (corresponding to 0.4 ps) and a resolution of 80 slabs along the *z* axis of the system. Since for periodic boundary conditions, the simulations need a system of two water phases separated by two lipid bilayers, the velocity profile shows all above regions twice. In addition, the profile shows another two regions of interest: the water-lipid interface and the lipid-lipid interface at the tails ends. The assignment of the various regions to slabs is given in Table 2.

Table 2. Assigning the slabs to membrane regions.

Region	Resolution 20 slabs[a]		Resolution 80 slabs	
	Slabs	[nm]	Slabs	[nm]
water phase[b]	1 to 2	0 to 1.42	1 to 3	0 to 0.53
water–lipid interface[a]			4 to 9	0.53 to 1.59
upper monolayer (A)	3 to 5	1.42 to 3.55	10 to 18	1.59 to 3.19
lipid–lipid interface (A)[a]			19 to 22	3.19 to 3.90
lower monolayer (A)	6 to 8	3.55 to 5.67	23 to 31	3.90 to 5.49
lipid–water interface[a]			32 to 37	5.49 to 6.56
water phase[b]	9 to 12	5.67 to 8.51	38 to 43	6.56 to 7.62
lipid–water interface[a]			44 to 49	7.62 to 8.68
upper monolayer (B)	13 to 15	8.51 to 10.64	50 to 58	8.68 to 10.28
lipid–lipid interface (B)[a]			59 to 62	10.28 to 10.99
lower monolayer (B)	16 to 18	10.64 to 12.76	63 to 71	10.99 to 12.58
lipid–water interface[a]			72 to 77	12.58 to 13.64
water phase	19 to 20	12.76 to 14.18	78 to 80	13.64 to 14.18

[a] The lower resolution does not resolve the interfaces. [b] The exchange slabs are always inside the water phase: 1 and 11 at a resolution of 20 slabs and 1 and 41 at a resolution of 80 slabs.

The two membranes, that is, the two halves of the simulation box, have to be symmetric in their properties. This is indeed found for the velocity profiles in Figure 6. In the following, the properties of the two membranes have been averaged [multiplying the velocities of the second half (slabs 41 to 80) by −1 and shifting it by half of the box length in the −*z* direction], to improve the statistics.

All consistency checks have been performed with a resolution of 20 slabs in the *z* axis (Table 2). This leads to an improved statistics at the expense of resolution, since four times as many atoms are averaged per slab for the mean velocity profiles. Among the key quantities discussed in the following is firstly the velocity gradient inside the water phase, which is directly related to the viscosity of water (of 0.55 cP at 327 K[32]) by Equation (3). It is estimated by fitting to those water slabs, in which no velocity exchange is performed. Secondly, there is the velocity gradient inside one of the pure lipid monolayers. In an infinitely long simulation this would be zero, as on average all atoms of a lipid move with the same velocity. In a finite simulation, it will not be exactly zero, but it should be much smaller than the velocity gradient inside the water phase. Here, the monolayer velocity gradient is estimated from a least-squares fit to the data points in each monolayer. In 20-slab resolution, there are only three slabs per monolayer; hence, the estimate can only serve as an orientation. The third quantity is the so-called velocity split. It is the velocity difference between the two monolayers. We calculate it as the velocity difference between all tail slabs of the right monolayer and all tail slabs of the left monolayer, as indicated in Table 2. This quantity has already been introduced as a measure for the internal membrane viscosity by Shkulipa et al.[10] These characteristic properties for the simulation of Figure 6 are listed in Table 3.

The Influence of Different Exchange Rates: Applying different velocity exchange periods causes the flux of transverse momentum to increase or decrease, which leads to different velocity profiles. Figure 7 shows the profiles for four different exchange periods tested with force field 1. The characteristic properties evaluated from these simulations are listed in Table 4. They lead to several observations. First, the absolute errors increase with increasing exchange period. The fact that a too infrequent exchange leads to a very flat velocity profile, where stochastic errors dominate over the mean value, is well known.[2] This is the reason why simulations at an exchange periods of 0.5 ps and 0.3 ps need a long time to accumulate enough statistics to extract significant data.

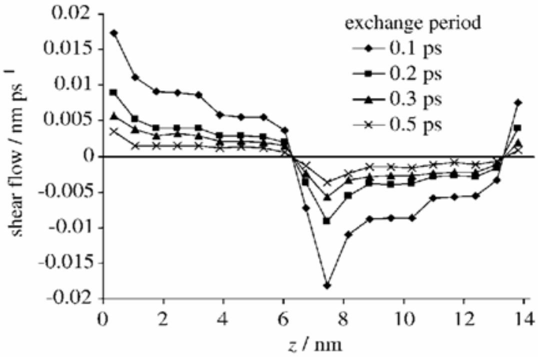

Figure 7. Comparison of different velocity exchange periods with force field 1 (*NVT* simulations, 20 slabs).

Table 4. Characteristics of non-equilibrium runs with different exchange periods for preliminary checks: force field 1, 20 slabs, constant *NVT* conditions.

Exchange period	Average momentum flux [u nm^{-1} ps^{-2}]	Monolayer velocity gradient [ps^{-1}]	Interlayer velocity split [nm ps^{-1}]	Interlayer friction coefficient [N s m^{-3}]	Water velocity gradient [ps^{-1}]	Water viscosity [cp]
0.1 ps	5.975 ± 0.002	$(2.17 \pm 0.29) \times 10^{-4}$	$(2.84 \pm 0.04) \times 10^{-3}$	6.99×10^{6}	$(1.55 \pm 0.01) \times 10^{-2}$	0.64
0.2 ps	3.010 ± 0.004	$(4.20 \pm 6.28) \times 10^{-5}$	$(1.00 \pm 0.12) \times 10^{-3}$	1.00×10^{7}	$(7.99 \pm 0.01) \times 10^{-3}$	0.63
0.3 ps	2.011 ± 0.002	$(8.63 \pm 6.65) \times 10^{-5}$	$(5.40 \pm 0.70) \times 10^{-4}$	1.24×10^{7}	$(6.76 \pm 1.74) \times 10^{-3}$	0.49
0.5 ps	1.211 ± 0.004	$(-4.80 \pm 6.25) \times 10^{-5}$	$(4.30 \pm 2.55) \times 10^{-4}$	9.35×10^{6}	$(5.21 \pm 3.94) \times 10^{-3}$	0.39

On the other side, simulations with a too short exchange period risk to produce velocity profiles, which are not linear anymore.[1] In our heterogeneous system, the linearity requirement only holds within the individual phases or regions. In this case, it is not possible anymore to calculate the shear viscosity by linear response theory. For SPC/E water, Bordat and Müller-Plathe[16] reported non-linearity effects with exchange periods of less then 0.2 ps time steps, resulting in an apparent lower viscosity of the simulated liquid.

These first checks (water velocity gradient vs momentum flux and interlayer velocity split vs momentum flux) showed linear behavior for exchange periods between 0.1 and 0.3 ps.

Effects of Variation of the Temperature Coupling Constant: The influence of a Berendsen thermostat on the RNEMD al-

Table 3. Characteristics of non-equilibrium runs with force field 2 under constant *NVT* conditions with a resolution of 80 slabs.

Exchange period	Average momentum flux [u nm^{-1} ps^{-2}]	Monolayer velocity gradient [ps^{-1}]	Interlayer velocity split [nm ps^{-1}]	Interlayer friction coefficient [N s m^{-3}]	Water velocity gradient [ps^{-1}]	Water viscosity [cp]
0.1 ps	5.162	$(6.69 \pm 8.10) \times 10^{-5}$	$(2.56 \pm 0.08) \times 10^{-3}$	6.70×10^{6}	$(1.63 \pm 0.06) \times 10^{-2}$	0.53
0.2 ps	2.609	$(-0.42 \pm 1.78) \times 10^{-4}$	$(9.59 \pm 1.19) \times 10^{-4}$	9.04×10^{6}	$(8.51 \pm 1.31) \times 10^{-3}$	0.51

gorithm was already studied for homogeneous fluids by Bordat and Müller-Plathe.[16] Depending on the system, the viscosity of a low-molecular-weight fluid is sensitive to changes in the coupling time. In a series of varying temperature coupling times with force field 2 and a resolution of 80 slabs, the viscosity of the water phase (Figure 8) has been investigated.

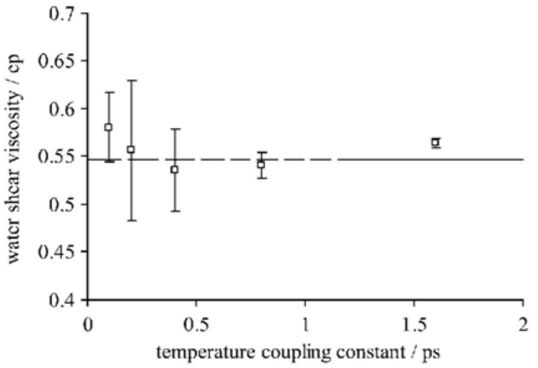

Figure 8. Shear viscosity of the water phase for varying-temperature coupling constants with force field 2. Each point was calculated from a simulation of 3 ns. The error bars were estimated from the standard deviations among the shear viscosities from three separate blocks of 1 ns each. The expected value from a linear interpolation of the experimental data[33] is marked by a dashed line (-----).

Table 5. Characteristics of non-equilibrium runs with different exchange periods for preliminary checks: force field 1, 20 slabs, constant *NPT* conditions.

Exchange period	Average momentum flux [u nm^{-1} ps^{-2}]	Monolayer velocity gradient [ps^{-1}]	Interlayer velocity split [nm ps^{-1}]	Interlayer friction coefficient [N s m^{-3}]	Water velocity gradient [ps^{-1}]	Water viscosity [cp]
0.1 ps	6.177 ± 0.027	$(-1.19 \pm 1.36) \times 10^{-4}$	$(1.87 \pm 0.264) \times 10^{-3}$	1.10×10^{7}	$(1.62 \pm 0.04) \times 10^{-2}$	0.63
0.2 ps	3.086 ± 0.014	$(5.23 \pm 8.80) \times 10^{-5}$	$(1.40 \pm 0.01) \times 10^{-3}$	7.32×10^{6}	$(8.28 \pm 1.62) \times 10^{-3}$	0.62
0.3 ps	2.072 ± 0.011	$(-0.98 \pm 3.20) \times 10^{-4}$	$(8.54 \pm 0.760) \times 10^{-4}$	8.06×10^{6}	$(5.22 \pm 0.11) \times 10^{-3}$	0.66
0.5 ps	1.256 ± 0.005	$(2.68 \pm 7.78) \times 10^{-5}$	$(2.90 \pm 1.53) \times 10^{-4}$	1.44×10^{7}	$(2.42 \pm 0.24) \times 10^{-3}$	0.86

The water phase serves as a check for the parameter settings. All calculated viscosities are marginally larger than the experimental values (≈0.53 cp).[33] Compared to simulations of bulk SPC/E water with a reaction field dielectric constant of 72 of Bordat and Müller-Plathe,[16] which extrapolates for 325 K to 0.45–0.5 cp, the values here are larger as well. A likely reason is that due to the low spatial resolution of the check runs, a part of the water–lipid interface lies within the evaluated slabs for the pure water. This leads to a systematic viscosity increase. Simulations with a higher resolution yield viscosities for the pure water phase of 0.48 ± 0.01 cp, which stands in perfect agreement with simulations at a reaction field dielectric constant of 72. This shows not only that the local viscosities can be recovered from anisotropic runs but also that the change in the reaction field dielectric constant to 54 is not significant for the viscosity.

Neglecting the systematic error, the plot shows a dependence of the local shear viscosity on the temperature coupling time in the range of only a few percent. This influence is smaller than errors from other sources such as the length of simulations and therefore the uncertainty in the gradients. Only at coupling times smaller then 0.2 ps and bigger than 0.8 ps the viscosity is increasing visibly. The influence of the temperature coupling time on the average velocity split of the lipid monolayers is less pronounced (not shown). For all coupling times between 0.1 and 1.6 ps, it is $(7.24 \pm 0.35) \times 10^{-4}$ nm ps^{-1}.

Constant-Pressure versus Constant-Volume Simulations: Changing the conditions from constant *NVT* to constant *NPT* influences the viscosity of the system as well. This has been tested for force field 1 at different exchange periods. Comparing the *NPT* data in Table 5 with the *NVT* data of Table 4, there are several points to make. The water velocity gradient for the *NPT* ensemble is steeper than for *NVT*. This leads to a viscosity of 0.63 cp. For small exchange periods (0.1 and 0.2 ps), the water shear viscosities of *NVT* and *NPT* runs deviate only by 0.01 cp. We have shown previously that the choice of ensemble as such has little influence on the shear viscosity of bulk water, as long as for both systems the macroscopic properties are the same (same temperature and density) and as long as the control parameters of the barostat are in a reasonable range.[17] Deviations at long exchange periods (0.3 and 0.5 ps) between *NVT* and *NPT* water shear viscosities origin in the growing influence of stochastic noise. Note that the viscosities calculated for the test systems are larger than those presented in Table 3, because (due to the lower resolution) the slab regions where the water phase exhibits a higher shear viscosity are also included in the calculations of Tables 4 and 5. This leads to viscosities around 0.63 cp (compared to 0.56 cp in Table 3 and 0.55 cp[32] in the experiments).

Expectedly, changing the simulation conditions has no effect on the velocity gradient in the lipid system. The values fluctuate around zero, within the error limit, by a comparable amount. However, the behavior of the velocity split between the monolayers at various momentum fluxes (imposed by different exchange periods) depends on the choice of the ensemble. Figure 9 summarizes the velocity splits obtained by different exchange rates. Corresponding velocity splits obtained at *NVT* and *NPT* conditions differ by up to 50% in an unsystematic way: At intermediate fluxes resulting from exchange periods of 0.2 ps 0.3 ps, the velocity splits at constant *NPT* conditions are about 0.0005 nm ps^{-1} larger than under constant *NVT* conditions, whereas at the highest and lowest fluxes the order is reversed. One should note, however, that in contrast to the ratio of a velocity gradient (in a single phase) to the momentum flux, the ratio of the velocity split to the momentum flux need not be constant, in either *NVT* or *NPT*. There is no theoretical requirement for linearity. On the contrary: At one momentum

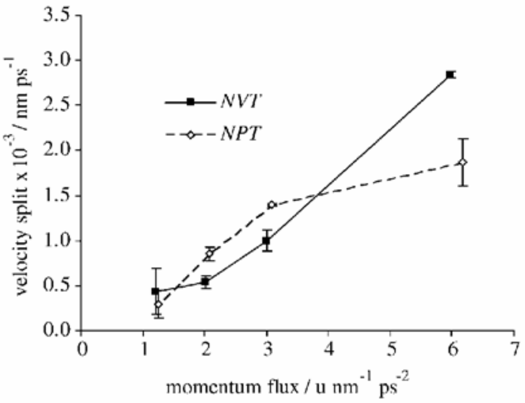

Figure 9. The velocity splits of monolayers obtained from simulations performed with *NPT* ensembles differ in the dependency on the exchange rate from those obtained using an *NVT* ensemble.

flux the monolayer–monolayer contact might be the favorite slipping plane of the system, whereas at another momentum flux slip might preferably take place in the water phase or at water–headgroup interface.

Comparison of the Force Fields: Since the two studied force fields only differ in the torsion potential of the lipids, the influence on the velocity profile, if any, was expected to be visible in the velocity split. In *NVT* runs with both force fields (80 slabs, 3 ns), the velocity split of force field 1 was 0.0010 ± 0.0003 nm ps^{-1}, whereas for force field 2 it was 0.00066 nm ps^{-1}. The results are close within the error bars, and much more sampling would be necessary to decide if there is any appreciable difference between them. While the different force fields cause many differences in the two different systems—among them we showed the effect on the area per headgroup and the diffusion coefficients—the effect on the velocity profile is smaller than the error bars. From their similarity we conclude that the consistency checks and comparisons obtained with force field 1 should also be valid for force field 2.

4.2.2. Local Viscosities of the DPPC Bilayer System at High Resolution

The shear velocity profiles which are obtained by force field 2 at a resolution of 80 slabs along the *z* axis are shown in Figure 10. The corresponding characteristic parameters are listed in Table 3.

The local viscosity is obtained through Equation (3) from the velocity gradient at a given data point, which in turn is calculated by a linear regression through the data point and its two neighbors (Figure 11). For several designated regions in the system, the calculated local viscosities can be found in Table 6.

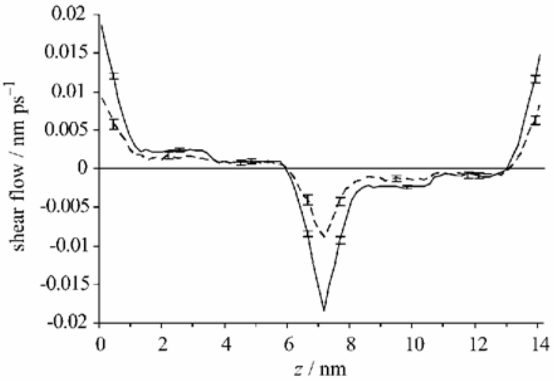

Figure 10. Comparison of the velocity profiles of the double bilayer system in an RNEMD simulation carried out with force field 2 and exchange periods of 50 [corresponding to 0.1 ps (——)] and 100 [corresponding to 0.2 ps (- - - -)]. Each simulation was performed for 5 ns. The error bars shown, one per region, have been derived from the standard deviation in one slab during these runs.

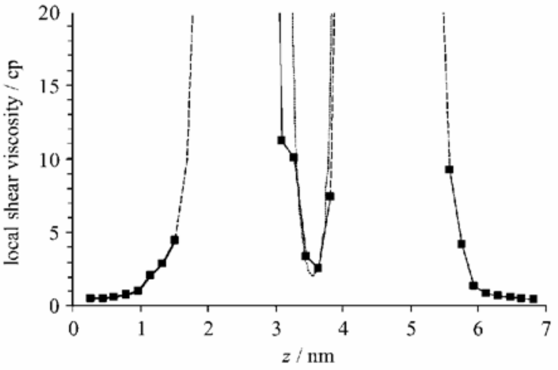

Figure 11. Local viscosities in a DPPC bilayer system. Using Equation (3) a local viscosity in every region of the membrane system can be defined. The gradients from Figure 12 for the RNEMD simulation with force field 2 at an exchange period of 0.2 ps have been converted into local viscosities. In the region of the alkane chains, the velocity gradient becomes essentially zero and the shear viscosity diverges (– – –). In the membrane centre ($z \approx 3.6$ nm), also the viscosity is shown (- - - - -), which has been calculated using average monolayer velocities weighted with local particle densities, see text. Both viscosities agree well.

The two interface regions shall be discussed in more detail. The water–lipid interface, which is defined by the slabs where a lipid density grows from 1 kg m^{-3} to more then 1000 kg m^{-3}, corresponds exactly to the slabs over which the local viscosity

Table 6. Local viscosities from runs with force field 2 under constant *NVT* conditions (80 slabs).

		Local shear viscosities [cp]			
Exchange period	Water phase	Beginning of lipid–water interface[b]	In the lipids		
			At head[a]	Aliphatic tail	At tail end
0.1 ps	0.49 ± 0.01	0.51 ± 0.01	2.29 ± 0.21	diverging	2.49 ± 0.08
0.2 ps	0.46 ± 0.03	0.50 ± 0.03	2.45 ± 0.46	diverging	2.96 ± 0.60

[a] The headgroup position was defined at the point where the lipid density is 500 kg m^{-3} (see Figure 4).
[b] The beginning of the interface was defined at a mean lipid density of < 1 kg m^{-3} (see Figure 4). The distance from the headgroup *z* position is 0.75 nm.

diverges from the value of pure water to infinity, the local viscosity within one monolayer. This increase in viscosity also strongly depends on the density of water molecules available. Since the lipids in steady state have to have the same velocity everywhere, the gradient is built up by the movement of the smaller and faster water molecules. The gradual increase of the local viscosity from the value of pure water to infinity signifies that water molecules stick to the interface. They are less mobile near the headgroups than in the bulk water. This means that at the water–lipid interface there is no slipping plane. The area of greatest slip (lowest viscosity) is inside the water phase.

Also the definition of the tail–tail interface region within the membrane by local density of the different monolayers corresponds exactly to the slabs where the local viscosity is finite again. Since the lipids move, on average, with the same velocity, there must be a slipping plane, or rather a slipping region where the tails of the two monolayers meet. This behavior is exactly found here. Since the resolution of the simulation is limited by the implemented algorithm, the exact shape of the local viscosity within the tail–tail region cannot be resolved directly. The average mutual velocity of all atoms in the same monolayer and the particle density profile (see Figure 4 b) allow deducing a much better resolved velocity profile for the tail–tail region, since the density profile is statistically much better defined than the velocity profile. Figure 12 shows the velocity profile calculated in this way. The viscosity profiles calculated by both methods are shown in Figure 11 as diamonds and short dashes, respectively. They are found to agree well. This allows for a distinct assignment of a local shear viscosity to the central slip plane of a lipid bilayer. For the DPPC bilayer system, this value is found to be 2.07 ± 0.01 cp. This compares to a disordered system of *n*-hexadecane at 25 °C[34] with 2.831 cp.

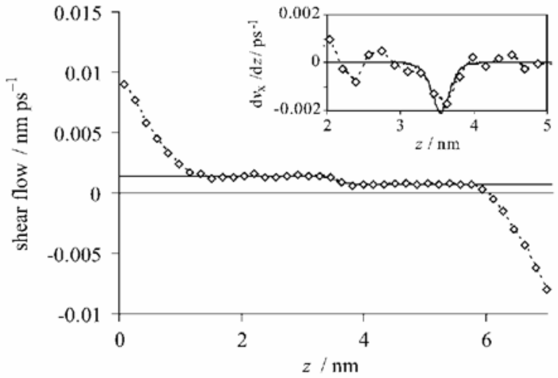

Figure 12. Velocity profile of an RNEMD simulation with an exchange occurring every 0.2 ps. The solid line (——) indicates the velocity profile calculated from the particle distribution and the average split velocity. In the inset, this profile is converted into a local viscosity profile with the solid line (——) converted correspondingly (only the tail region is shown).

The inset of Figure 12 also allows defining the width of the monolayer–monolayer slip region ΔL. It is approximately 1 nm between the points where the velocity gradients are zero. The effective width of the slip plane is important for comparing our results with experimental measurements. Experiments do not measure the interlayer viscosity but an interlayer friction coefficient ξ, which is defined as [Eq. (8)]:

$$\xi = \frac{F}{A\Delta v} \tag{8}$$

where F is the shear force applied to the membrane, A is the membrane surface area, and Δv is the interlayer velocity split. The ratio F/A equals the momentum flux $J_z(p_x)$. In other words, if Δv is replaced by (dv_x/dz), the interlayer friction coefficient is transformed into the interlayer viscosity. With the knowledge of ΔL, the derivative can be approximated as $(dv_x/dz) \approx (\Delta v/\Delta L)$, or [Eq. (9)]:

$$\eta = \Delta L \xi \tag{9}$$

In the experimental literature, values of ξ have been reported between 1×10^8 and 2×10^9 N s m^{-3}. After multiplying these values by $\Delta L \approx 10^{-9}$ m, they translate into viscosities of 100–2000 cp.[4,35,36] Our calculations yield shear viscosities which are in the same order of magnitude as those of Shkulipa et al.[10] Using the RNEMD method with our united-atoms force field rises the shear viscosity only by a factor of 1.5 compared to their coarse grained model. Although we reach shear viscosities closer to the experimental ones they still are one to two orders of magnitude below those of the experiments.

Finally, a comparison of the local viscosities of simulations performed with exchange periods of 0.1 and 0.2 ps is shown in Figure 13. The two profiles show only statistical deviations from each other. The viscosities are practically the same for both exchange rates, which indicates that the exchange rates are small enough so that they do not affect the linear response of the simulations in all the regions of this heterogeneous system.

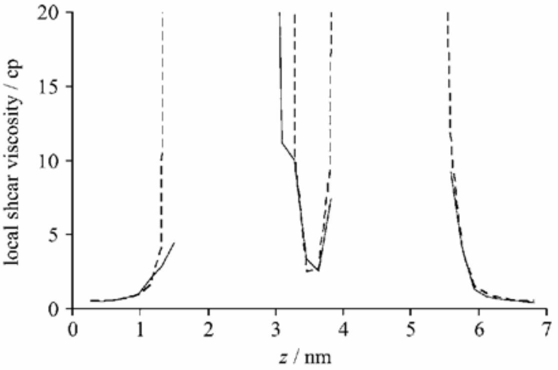

Figure 13. Comparison of the local viscosities of the runs with an exchange period of 0.2 ps (——) and the one with an exchange period of 0.1 ps (----).

5. Conclusions

The RNEMD method could be extended from homogeneous bulk fluids to the heterogeneous environment of lipid bilayer systems. Careful studies on exchange rates, cutoff distances, and thermostat parameters showed that there is a range of simulation parameters where useful viscosity data can be calculated for all regions of the system.

As the flux of transverse momentum is constant over the system, variations of the local shear viscosity manifest themselves in variations of the gradient of the shear flow velocity over the thickness of the membrane. The most important observations are: 1) The lowest viscosity is found in the region of bulk water, far from the lipid bilayer. All parts of the bilayer are higher in viscosity. 2) There is no slipping plane or slipping region near the head groups of the membrane. The viscosity in this region increases steadily form the value of bulk water to practical infinity. This indicates that water molecules are less mobile closer to the lipid headgroups. 3) The only region of slip inside the membrane is the centre where the alkane chains of both monolayers meet. In this region, approximately 1 nm wide, the apparent local shear viscosity takes approximately the value of bulk *n*-hexadecane, which is not unreasonable.

The shear viscosities calculated for these observations are one to two orders of magnitudes smaller than the experimental ones. A speedup in the slipping velocity may originate from the chosen united-atom model. Compared to a fully atomistic description, it lacks some inter-leaflet coupling effects at the molecular level. A second model-based influence may be found in the area per headgroup which is smaller than that of the originally published force field. Furthermore, the molecular dynamics method is limited by the current computational power to system dimensions of a few nanometers. Therefore, influences of long-wavelength undulation are suppressed by the periodic boundary conditions and will not contribute to the result of the simulation. It can also not be excluded that differences in the shear viscosities originate in the simulation setup (e.g. the resulting slip rate).

Although not matching exactly with the experimental values, we were able to show that the RNEMD method leads to the expected increase in shear viscosity in comparison to a corresponding coarse-grained force field.

Keywords: membranes · molecular dynamics · monolayers · non-equilibrium · shear viscosity

[1] S. Singer, G. L. Nicholson, *Science* **1972**, *175*, 720–731.
[2] O. G. Mouritsen, *Life—As a Matter of Fat*, Springer, Heidelberg, **2005**.
[3] E. Evans, V. Heinrich, *C. R. Phys.* **2003**, *4*, 265–274.
[4] E. Evans, A. Yeung, *Chem. Phys. Lipids* **1994**, *73*, 39–56.
[5] R. M. Raphael, R. E. Waugh, *Biophys. J.* **1996**, *71*, 1374–1388.
[6] Y. A. Chizmadzhev, D. A. Kumenko, P. I. Kuzmin, L. V. Chernomordik, J. Zimmerberg, F. Cohen, *Biophys. J.* **1999**, *76*, 2951–2965.
[7] W. K. den Otter, S. A. Shkulipa, *Biophys. J.* **2007**, *93*, 423–433.
[8] M. Patra, M. Karttunen, *J. Phys. Chem. B* **2004**, *108*, 4485–4494.
[9] A. Yeung, E. Evans, *J. Phys. II* **1995**, *5*, 1501–1523.
[10] S. A. Shkulipa, W. K. den Otter, W. J. Briels, *Biophys. J.* **2005**, *89*, 823–829.
[11] W. F. van Gunsteren, H. J. C. Berendsen, *Mol. Phys.* **1977**, *34*, 1311–1327.
[12] A. W. Lees, S. F. Edwards, *J. Phys. C* **1972**, *5*, 1921–1928.
[13] X. Y. Chen, P. Carbone, W. L. Cavalcanti, G. Milano, F. Müller-Plathe, *Macromolecules* **2007**, *40*, 8087–8095.
[14] H.-J. Qian, P. Carbone, X. Chen, H. A. Karimi-Varzaneh, C. C. Liew, F. Müller-Plathe, *Macromolecules* **2008**, *41*, 9919–9929.
[15] F. Müller-Plathe, *Phys. Rev. E* **1999**, *59*, 4894–4898.
[16] P. Bordat, F. Müller-Plathe, *J. Chem. Phys.* **2002**, *116*, 3362–3369.
[17] T. J. Müller, M. Al-Samman, F. Müller-Plathe, *J. Chem. Phys.* **2008**, *129*, 014102.
[18] F. Müller-Plathe, *Comput. Phys. Commun.* **1993**, *78*, 77–94.
[19] L. D. Schuler, X. Daura, W. F. van Gunsteren, *J. Comput. Chem.* **2001**, *22*, 1205–1218.
[20] I. Chandrasekhar, M. Kastenholz, R. D. Lins, C. Oostenbrink, L. D. Schuler, D. P. Tielemann, W. F. van Gunsteren, *Eur. Biophys. J.* **2003**, *32*, 67–77.
[21] T. J. Müller, F. Müller-Plathe, *J. Hazard. Mater.* **2009**, *168*, 13–24.
[22] E. Egberts. H. J. C. Berendsen, *J. Chem. Phys.* **1988**, *89*, 3718–3732.
[23] J. F. Nagle, S. Tristram-Nagle, *Biochim. Biophys. Acta Rev. Biomembr.* **2000**, *1469*, 159–195.
[24] C. Anézo, A. H. de Vries, H.-D. Höltje, D. P. Tielemann, S.-J. Marrink, *J. Phys. Chem. B* **2003**, *107*, 9424–9433.
[25] W. F. van Gunsteren, S. R. Billeter, A. A. Eisenring, P. H. Hünenberger, P. Krüger, A. E. Mark, W. R. P. Scott I. G. Tironi, *Biomolecular Simulation: The GROMOS96 Manual and User Guide*, vdf, Zuerich, **1996**.
[26] Z. V. Leonenko, E. Finot, H. Ma, T. E. S. Dahms, D. T. Cramb, *Biophys. J.* **2004**, *86*, 3783–3793.
[27] S. Tristram-Nagle, T. Moore, H. I. Petrache, J. F. Nagle, *Biochim. Biophys. Acta Biomembr.* **1988**, *938*, 135–142.
[28] J.-P. Hansen, I. R. McDonald, *Theory of Simple Liquids*, Academic Press, London, **1986**.
[29] S. König, W. Pfeiffer, T. Bayerl, D. Richter, E. J. Sackmann, *J. Phys. II* **1992**, 2, 1589- 1615.
[30] R. Lipowski, E. Sackmann, *Structure and Dynamics of Membranes*, Elsevier, Amsterdam, **1995**.
[31] P. F. F. Almeida, W. L. C. Vaz, T. E. Thompson, *Biochemistry* **1992**, *31*, 6739–6747.
[32] G. W. C. Kaye, T. H. Laby, *Tables of physical and chemical constants*, Longman, London, **1948**.
[33] D. R. Lide, *CRC Handbook of Chemistry and Physics, 82nd ed.*, CRC, Boca Raton, **2001**.
[34] Y. Marcus, *The Properties of Solvents*, Wiley, New York, **1998**.
[35] R. M. Raphael, R. E. Waugh, *Biophys. J.* **1996**, *71*, 1374–1388.
[36] Y. A. Chizmadzhev, D. A. Kumenko, P. I. Kuzmin, L. V. Chernomordik, J. Zimmerberg, F. Cohen, *Biophys. J.* **1999**, *76*, 2951–2965.

Received: March 2, 2009
Revised: July 2, 2009

4.3. Wärmetransport: Wärmeleitfähigkeit von DPPC Membranen

Der dritte Transportprozess durch Biomembranen, der im Rahmen dieser Dissertation untersucht wird, ist der Wärmetransport. Alle drei fundamentalen Wärmetransportarten (Wärmeleitung, Wärmestrahlung, Konvektion) sind in einem biologischen System wichtig: Konvektion zur Temperaturregelung im Körper, Wärmestrahlung der Sonne oder von Feuer als externe Wärmequelle für den Körper (resp. der umgekehrte Prozess der Wärmeabstrahlung) und die Wärmeleitfähigkeit beim Schwitzen, Frieren oder Verbrühen. Die hier durchgeführten Berechnungen konzentrieren sich auf das letzte Phänomen.

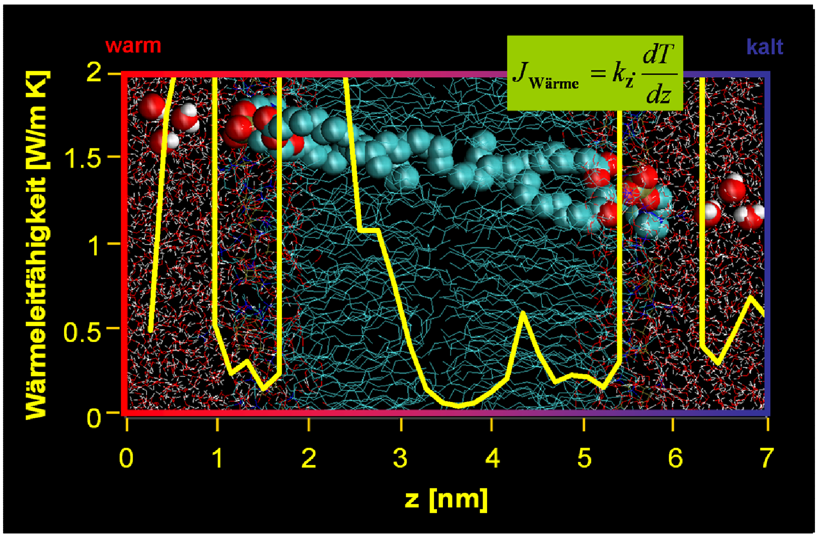

Abb. 5: Das scheinbare, lokale Wärmeleitfähigkeitsprofil durch eine Dipalmitoylphosphatidylcholinmembran

Was sich zunächst als einfache Abwandlung der im letzten Kapitel vorgestellen RNEMD Methode präsentiert (anstatt des Austauschs von Geschwindigkeitskomponenten in die Richtung einer kartesischen Koordinate wird zur Ermittlung der Wärmeleitfähigkeit die komplette Geschwindigkeit ausgetauscht), entpuppt sich bei genauerer Analyse als nicht ganz so trivial. Der Grund dafür liegt in der hohen Ordnung des berechneten zweilagigen Systems verborgen. Die RNEMD wurde schon in vielen Anwendungen von einzelnen kleinen Molekülen bis hier zu komplexen Polymerschmelzen erfolgreich angewendet. In allen Fällen sorgte die Homogenität des Systems dafür, dass Rundungsfehler in der Berechung der Kräfte zu einem homogenen Aufwärmen des Systems führten. Diese Wärme wurde dann vom Thermostaten gleichmäßig wieder aus dem System gezogen. Im Fall der Membran jedoch kommt es aufgrund von stellenweise fehlenden elektrostatischen Wechselwirkungen (die aliphatischen Schwanzgruppen der Lipidmoleküle besitzen keine Partialladung) dort zu keinen Rundungsfehlern. Dadurch kühlen sich die Schwanzgruppen netto ab, während sich die Wasserphase und die Kopfgruppenregion aufwärmen.

Dieser Effekt beeinflusst die Ergebnisse der RNEMD Simulationen. Dieses Kapitel zeigt nun detailliert auf, welche Einflüsse in welcher Größenordnung in solchen Rechnungen auftreten. Wir demonstrieren die Resultate in Abhängigkeit von verschiedenen äußeren Faktoren, wie unterschiedliche Druckbehandlung, verschiedene mittlere Temperaturen und verschiedene Wärmetransportraten. Diese Untersuchungen dienen als Basis für zukünftige Studien des Wärmetransportphänomens an geordneten Systemen (z.B. unter Verwendung von anderen Potentialen, die weniger sensibel auf Rundungsfehler reagieren). Sie erlauben eine Abschätzung der Pros und Kontras der beobachteten asymmetrischen Wärmeleitfähigkeit in Biomembranen und dienen als Grundlage für ein besseres Verständnis der RNEMD Methode.

Das Einreichen der hier präsentierten Texte als wissenschaftlicher Artikel für eine Sonderausgabe des International Journal of Quantum Chemistry wird in den Tagen nach Abgabe dieser Dissertation erfolgen.

Heat transport through a biological membrane – an asymmetric property? Technical issues of the reverse non-equilibrium molecular dynamics method

Thomas J. Müller*, Florian Müller-Plathe

Theoretische Physikalische Chemie,
Eduard-Zintl-Institut für Anorganische und Physikalische Chemie,
Technische Universität, Petersenstrasse 20, 64287 Darmstadt, Germany
Tel: 01651 / 16 23 98, Fax: 01651 / 16 65 26
* t.mueller@theo.chemie.tu-darmstadt.de

To investigate heat transport across a biological membrane we performed a series of reverse non-equilibrium molecular dynamics (RNEMD) simulations on a model dipalmitoylphosphatidylcholine (DPPC) bilayer system at the atomistic level. In a detailed analysis of the irritating initial results, we show how and to which extent the RNEMD method (in the special case of an ordered system like in bilayers) is influenced by simulation conditions. We prove that the interaction between the description of the long range forces and the thermostat can lead to significant changes in the apparent local thermal conductivity profile across the membrane. As this is the first case reported where the otherwise robust RNEMD results are not directly interpretable, we discuss not only the reasons but also several concepts to handle this effect. Note that this is not a flaw of the RNEMD method but of the simulation framework it is performed in. The complete understanding of the directly obtained results finally allows us to describe the heat flow across the membrane qualitatively. We prove that the tail-tail interface of the bilayer is the most hindering region for the heat flow and the dominating part for the overall thermal conductivity of the membrane. We finally demonstrate quantitatively that the local thermal conductivity in that region increases with increasing temperature.

I Introduction

All three fundamental heat transport mechanisms – heat conductivity, radiation, and convection – play an important role in biological systems. Heat exchange with the environment is an important feature of the human body. The constant core temperature of the human body of about 36.5°C is the result of many heat transport processes. Excess heat produced by cell respiration, by intake of sun radiation or by the environmental temperature is emitted by free convection, radiation, and evaporation. Basic physical considerations on the influence of convection and radiation [I] have stimulated several experimental measurements [II, III] and theoretical calculations [IV, V]. The effect of heat conduction is often neglected when evaporation (through perspiration) is not considered.

The cited studies concentrate on the macroscopic length scale. The effective transfer of heat from or into a cell has, to our best knowledge, not been studied in detail yet. On this scale, thermal conduction is the only heat-transport mechanism. There are studies of different caloric properties [VI] which also deal with the heat capacity of lipids and the associated change of transmembrane distributions [VII]. But these works focus on the lipid layer itself and not on the transmembrane direction.

To investigate the heat transport through the membrane an atomistic resolution is required. The velocity of each atom of the membrane has to be determined accurately in order to evaluate local temperatures. The methods of choice for such requirements are simulations of the molecular dynamics type. In those computational calculations velocities of all considered atoms are exactly known at any time in the simulation.

Investigations of the heat transport and the calculation of the thermal conductivity, the associated transport coefficient, have become standard procedures in molecular dynamics simulations. In 1999 the reverse non-equilibrium molecular dynamics (RNEMD) algorithm [VIII] - a new robust method - has been introduced and it showed soon its potential in applications. The initial studies of Lennard-Jones fluids were followed by studies of molecular liquids [IX, X] amorphous polymers [XI, XII], polymer crystals [XIII] and carbon nanotubes [XIV].

According to the definition of the thermal conductivity as a macroscopic property, all these investigations report just an average specific thermal conductivity of one homogeneous system. As we have already shown for the shear viscosity [XV] the RNEMD algorithm allows an exact calculation of the flux in the simulation box. Therefore even shear profiles, which due to heterogeneities are nonlinear across the system, can be converted into local viscosities. In analogy to that work we apply the RNEMD algorithm for the local thermal conductivity within the heterogeneous membrane-water assembly.

II Method

Molecular dynamics simulations provide a valuable tool to investigate a system at an atomistic level. For the purpose of this work the simulation package YASP [XVI, XVII] has been chosen because it is equipped with a RNEMD routine to compute thermal conductivities.

YASP is a molecular dynamics code developed by F. Müller-Plathe. The calculation of the potential contains different terms of standard form, from which the forces acting on the atoms are derived. Important for the later discussion is the treatment of electrostatic interactions in YASP. The two non-bonded potentials depend on the distance r_{ij} between interacting particles. For reasons of simplicity, in YASP only two-body interactions are considered which include a Lennard-Jones term defined by the parameters σ_{ij} and ε_{ij} and a Coulomb term which depends on the partial charges q_i of the two interacting particles, on the effective dielectric constant ε, and on the vacuum permittivity ε_0:

$$V_{nonbonded} = \sum_{i,j}\left(4\varepsilon_{ij}\left[\left(\frac{\sigma_{ij}}{r_{ij}}\right)^{12} - \left(\frac{\sigma_{ij}}{r_{ij}}\right)^{6}\right] + \frac{q_i q_j}{4\pi\varepsilon\varepsilon_0}\left(\frac{1}{r_{ij}} - \frac{\varepsilon_{RF}-1}{2\varepsilon_{RF}+1}\cdot\frac{r_{ij}^2}{r_{cutoff}^3}\right)\right) \qquad (1)$$

To handle long-range interaction forces a correction is introduced by the reaction field parameter ε_{RF} and the cutoff radius r_{cutoff}.

For the evaluation of the thermal conductivity of the system, the reverse non-equilibrium molecular dynamics scheme [XVIII] was applied. It has been described in detail, so a short overview is sufficient here. This method divides the simulation box along the axis, along which the thermal conductivity is to be evaluated, into n_{tot} virtual slabs of equal thickness. We chose the bilayer to be parallel to the xy plane. Thus we observe the thermal conductivity along the z axis which is oriented perpendicular to the bilayer. The virtual slabs are aligned parallel to the bilayer. The temperature T in each slab can be calculated by the equipartition theorem:

$$\left(\frac{3N}{2} - C\right)k_B T = \frac{1}{2}\left\langle \sum_{i=1}^{N} m_i v_i^2 \right\rangle. \qquad (2)$$

This links the temperature through the Boltzmann constant k_B, the number of atoms N in the slab, and the number of constraints C in the slab to the kinetic energy E_{kin} of all atoms in the slab. The kinetic energy $E_{kin,i}$ of an atom i is defined by its mass m_i and its velocity v_i which is calculated from the Cartesian components $v_{i,x}$ $v_{i,y}$, and $v_{i,z}$ of the velocity vector:

$$E_{kin,i} = \frac{1}{2} m_i v_i^2 = \frac{1}{2} m_i \left(v_{i,x}^2 + v_{i,y}^2 + v_{i,z}^2 \right) \tag{3}$$

Two of the slabs will be important for the RNEMD algorithm. The first slab ($n = 1$) will accumulate kinetic energy and is therefore labeled “hot slab”. The one in the middle ($n = n_{tot}/2+1$) will loose kinetic energy and is labeled “cold slab”.

When performing a standard molecular dynamics simulation, the RNEMD algorithm introduces after every w time steps an exchange step. Therefore w is called exchange period. In the exchange step the algorithm looks for the atom with the lowest kinetic energy in the hot slab and the one with the highest kinetic energy in the cold slab and exchanges their kinetic energies. Ensuring by the setup that the two atoms have the same mass, this exchange is achieved by interchanging all Cartesian velocity components of the two chosen atoms.

In this unphysical way an easy-to-calculate amount of kinetic energy is transferred from the cold slab to the hot slab in each exchange step. This results in a heating of the hot slab and the cooling of the cold slab. The system tries to equilibrate this gradient in a physical way: heat flow through the box from the hot to the cold slab. Due to the periodic boundary conditions applied in the simulations, the heat has two different ways to flow from the hot to the cold slab. In our setup it is the $+z$ and the $-z$ direction. To ensure that the heat flux in an ordered system is the same in both directions, the system has to be symmetric with respect to the exchange slabs. The symmetry is realized by using two lipid bilayers with two intervening water phases, in which the velocity exchange takes place.
Thus the heat flux $j_z(Q)$ induced by the exchange of the kinetic energies in one direction can be calculated by the difference of the energies involved in the exchange ($E_{kin,n/2+1}$ of the middle slab and $E_{kin,1}$ of the first slab), the time t, and the box dimensions L_x and L_y in the x and y direction:

$$j(Q) = \sum_{exchange} \frac{E_{kin,n/2+1} - E_{kin,1}}{2tL_x L_y} \tag{4}$$

Since the exchange continues to happen periodically, equilibrium will never be achieved. After an initial time a steady state will form, in which the physical heat flow equals through the system the unphysical flux imposed by the exchange. In the limit of linear response the heat flux $j_z(Q)$ and the resulting temperature gradient $\partial T/\partial z$ in the system are collinear and proportional to each other. The proportionality constant κ is the thermal conductivity.

$$j_z(Q) = -\kappa \frac{\partial T}{\partial z} \tag{5}$$

Note that due to energy conservation the steady-state flux is always constant and does not depend on the position along the z direction. In contrast, the temperature gradient only needs to be constant in a system which shows no heterogeneities in z direction. For a heterogeneous system such as the membrane assemblies discussed in this contribution, it needs not be constant. On the contrary, by evaluating the temperature gradient locally at a position i in the system a local thermal conductivity κ_i can be defined

$$j_z(Q) = -\kappa_i \left[\frac{\partial T}{\partial z} \right]_i \tag{6}$$

III Computational Details

As the RNEMD algorithm was already implemented in YASP and thoroughly tested, this simulation package was the program of choice. The force field for the DPPC bilayer was derived from the publication of the GROMOS A45 force field [XIX]. The general force fields of GROMOS [XX] and YASP contain the same potential terms. Thus the GROMOS force field was transferred to YASP parameterization. It has already been applied to study the penetration of small molecules through this lipid bilayer [XXI] and to determine the shear viscosity of this model membrane [XV]. It strengths and weaknesses have been discussed there.

The DPPC system was constructed by placing tail group against tail group of two DPPC monolayers of 64 lipid molecules in all-trans position arranged on a 8x8 quadratic grid with side length l = 6.25 nm. After adding 1827 water molecules on top of the bilayer and 1828 water molecules at the bottom, the system was equilibrated at constant pressure (anisotropic coupling) of p_{targ} = 101.3 kPa (with a pressure coupling time of τ_p= 0.5 ps) and constant temperature T_{targ} = 325 K (τ_T = 0.2 ps). The cutoff was set to 1.2 nm and a reaction field dielectric constant of ε = 54 was applied, while the neighbor list had a cutoff of 1.4 nm and was updated every 15 time steps. To avoid huge forces and to prevent the bond constraining SHAKE algorithm from failing, in the first 10 runs the number of time steps (10 to 1000) and the time step size ($2*10^{-7}$ ps to $2*10^{-3}$ ps) were increased gradually. The velocities of atoms were redistributed at the beginning of each simulation anew according to a Boltzmann distribution around T_{targ}. This procedure was followed by an equilibrium simulation run of 20 ns with a time step size t of 0.002 ps. The other parameters were kept fixed.

In all RNEMD simulations a Berendsen thermostat with various target temperatures T_{targ} (300 K, 325 K, 350 K, 375 K, and 400) and τ_T = 0.2 ps has been used. In explicitly labeled simulations, when enforcing constant pressure instead of constant volume, an anisotropic Berendsen manostat with p_{targ} = 101.3 kPa and τ_p = 0.5 ps in x, y, and z direction was applied. The cutoff distance of r_{cut} = 1.2 nm was always coupled with a neighbor list with a cutoff of r_{neigh} = 1.4 nm which was updated every 15 time steps. The reaction field parameter was ε = 54. The simulations with a step size of 2 fs covered a total simulation time of at least 6 ns (if longer, it is mentioned at the corresponding simulations). The RNEMD exchange has been applied every w = 100, w = 200, or w = 400 time steps and exchanged the center of mass velocities of water molecules. The number of slabs, and therefore the resolution of the RNEMD data, amounts to 80. While the RNEMD specific results were written out every 101 time steps, the trajectory itself was logged every 1000 time steps.

In the additional check simulations some simulation parameters deviate from the ones of the standard runs: In the calculations with the smaller cutoff r_{cut} = 0.8 nm (also reducing the neighbor list radius to r_{neigh} = 1.0 nm) a total time of 2 ns was simulated. The simulation which enlarged the time step from t = 2 fs to t = 4 fs ran for a total time of 4 ns. In a third test run of 2 ns the reaction field parameter ε has been changed to 10^5.

Supplementary Lennard-Jones (LJ) simulations have been performed with an argon-like uncharged parameter set: ε = $1.645 \cdot 10^{-21}$ J, and σ = 0.3405 m. The standard mass of such a LJ particle was m_{std} = 39.948 g mol^{-1}. In some of those simulations a fraction of the LJ particles were assigned double of the standard mass m_{2std} = 2 m_{std} = 79.896 g mol^{-1} (see below).

The initial LJ system was built by putting 5184 particles on an equally spaced 10x10x52 grid in a box with dimensions l_x = 3.425 nm l_y = 3.425 nm l_z = 20.55 nm. This resulted in an average density of the system of ρ = 1426.6 kg/m^3.To receive a multi phase system, the first 1296 molecules were labeled A, the next 1296 B, the following ones 1296 again A, and the last 1296 molecules again B. Only for molecules of the same type we allowed attractive (and repulsive) LJ interactions. Atoms with different labels only experienced repulsive pair forces.

The equilibration of the LJ system was performed at constant volume with a step size of 2 fs for a total simulation time of 100 ps. The cutoff radius was set to 0.8 nm with the corresponding cutoff r_{neigh} = 1.0 nm of the neighbor list which was updated every 15 time steps. The temperature was set to 167.72 K and controlled by a Berendsen thermostat with τ_T = 1.07817 ps. The temperature has been chosen according to the phase diagram of Scott et. al. [XXII] to assure that the LJ fluids form a symmetric immiscible two phase system. This has been checked and confirmed by density plots (not shown here).

Three different LJ systems have been investigated: One with m_A = m_B = m_{std}, one with m_A = 0.5 m_B = m_{std}, and one with 0.5 m_A = m_B = m_{std}. An additional equilibration of 100 ps was performed. All three systems were simulated at two different exchange periods w = 50 and w = 100. With a time step of 2 fs a total simulation time of 10 ns was performed (for the 0.5 $m_A = m_B = m_{std}$ system, the total simulation time was 5 ns). The cutoff of these simulations were 0.8 nm, with a neighbor list cutoff of 1.0 nm (neighbor list update ever 15 time steps). The temperature was coupled to T_{targ} = 167.72 K with τ_T = 1.07817 ps. The RNEMD algorithm had a resolution of 100 slabs and wrote out the RNEMD data every 101 time steps. A general trajectory output was not needed.

The evaluation of the data was the same for all simulations. In the first step, the temperature profiles calculated by YASP at every 101 time steps were time averaged. The mirror symmetry of the temperature profile with respect to the exchange slabs was then used to average again over the two heat transport pathways within the simulation system. This leads to the reported temperature profiles.

To convert the temperature profiles into local thermal conductivity profiles a local gradient had to be defined. For each slab we performed a linear regression of the temperature values of this and the two neighboring slabs. Mathematically this corresponds to fitting a parabola to the three points where we measure the slope of the tangent at the center point. The evaluated gradient was then converted using eq. 6 and the average imposed flux into a local thermal conductivity. Doing so for all data points (omitting the edges where no left and right neighboring slabs exist) leads to the reported local thermal conductivity profiles.

IV Results and Discussion

This section is divided into four parts. In a first phenomenological part we show the local thermal conductivity results. Then we interpret these results on the basis of other properties of the system. In the second part we work out the relation between the local thermal conductivity and the density profile and in the third part the influence of local heat sources and heat sinks. In the next part we estimate the impact of these factors. Finally we interpret the data biologically.

A) The phenomenon: When using the RNEMD algorithm to calculate the thermal conductivity of homogeneous systems, the response of the system generally results in a linear temperature profile. The temperature gradient and the imposed flux are directly related to the thermal conductivity of the homogeneous system.

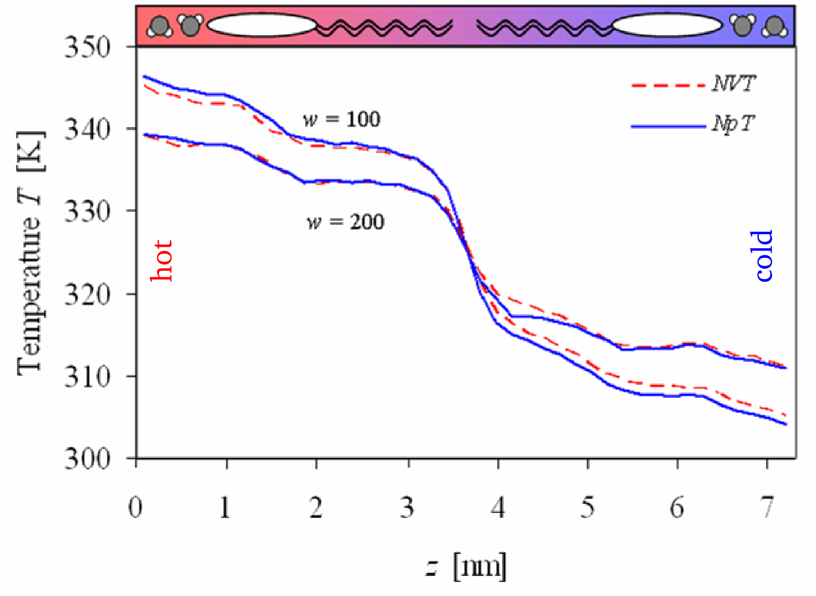

Fig. 1: Temperature profile across one solvated DPPC bilayer at an average temperature of 325 K under constant pressure (*NpT*) and constant volume (*NVT*) conditions with the exchange periods w = 100 time steps (larger gradient) and w = 200 time steps (smaller gradient). A constant heat flux causes regions with different temperature gradients. The general features of these regions are the same when simulating at constant volume or constant pressure and do not vanish when altering the heat flux.

Since a DPPC bilayer system along its perpendicular axis (in this work the z axis) is highly inhomogeneous, a curved temperature profile as reported in fig. 1 was not unexpected. We clearly see different regions of different linear gradients (indicating a medium with constant thermal conductivity), and as well curved ones. Macroscopically the thermal conductivity is therefore ill-defined and we have to concentrate on the local thermal conductivities in different regions.

A second look at the temperature profile however shows unexpected details. Although the water phase at the left (hot) and the right (cold) side of the plot tend to have similar gradients, the behavior of the gradient at the right differs from the one at the left side of the membrane. When having passed the water phase at the left side, the gradient becomes steeper and then flattens again. This is exactly the opposite when approaching the interlayer region from the right side. Here the profile is first flat while steeper afterwards. Approaching the center of the membrane, the gradients on the left and on the right side become similar again. The steep gradient indicates a low thermal conductivity between the two tail groups of the monolayers.

Fig. 1 also shows that the features of the temperature profile do not depend on the chosen simulation conditions. Whether a Berendsen manostat is applied (constant pressure simulations, *NpT*) or not (constant volume simulations, *NVT*) the features of all four profiles are the same. The temperature profiles of the *NVT* and *NpT* simulations at small exchange rates are identical within the error bars. But at higher exchange rates the gradient of the *NpT* run is steeper than the one of the *NVT* run which is consistent with the slightly enhanced flux which is recorded for *NpT*. This is the (small) effect of the introduction of a Berendsen manostat on the RNEMD algorithm. The enhanced flux and the proportionally to the heat flux enhanced gradient are a result of the different velocity distributions in the exchange slabs. The different velocity distribution is caused by the additional system scaling introduced by the manostat. In the exchange slab this leads to different velocities of the exchange atoms. Thus heat flux and gradient can change but the local thermal conductivity remains the same, as long as linear response is fulfilled. The influence of an additional manostat on the thermal conductivity has been shown to be negligible as long as the density is conserved [XXIII]. A comparison with a simulation under *NVE* conditions is not possible because the truncation errors of the electrostatic forces at the cutoff of the water molecules lead to a rapid increase of the total temperature. Therefore the recording of a stable temperature profile would not be possible.

The conversion of the temperature profile into a local thermal conductivity profile leads to fig. 2. This profile shows many features, which need an explanation:

- The global minimum of the profile is found in the middle of the simulation box. This region is the tail-tail-interface of the bilayer. But the minimum is shifted towards the cold side by more than 0.1 nm compared to what is expected from the equilibrium profile.

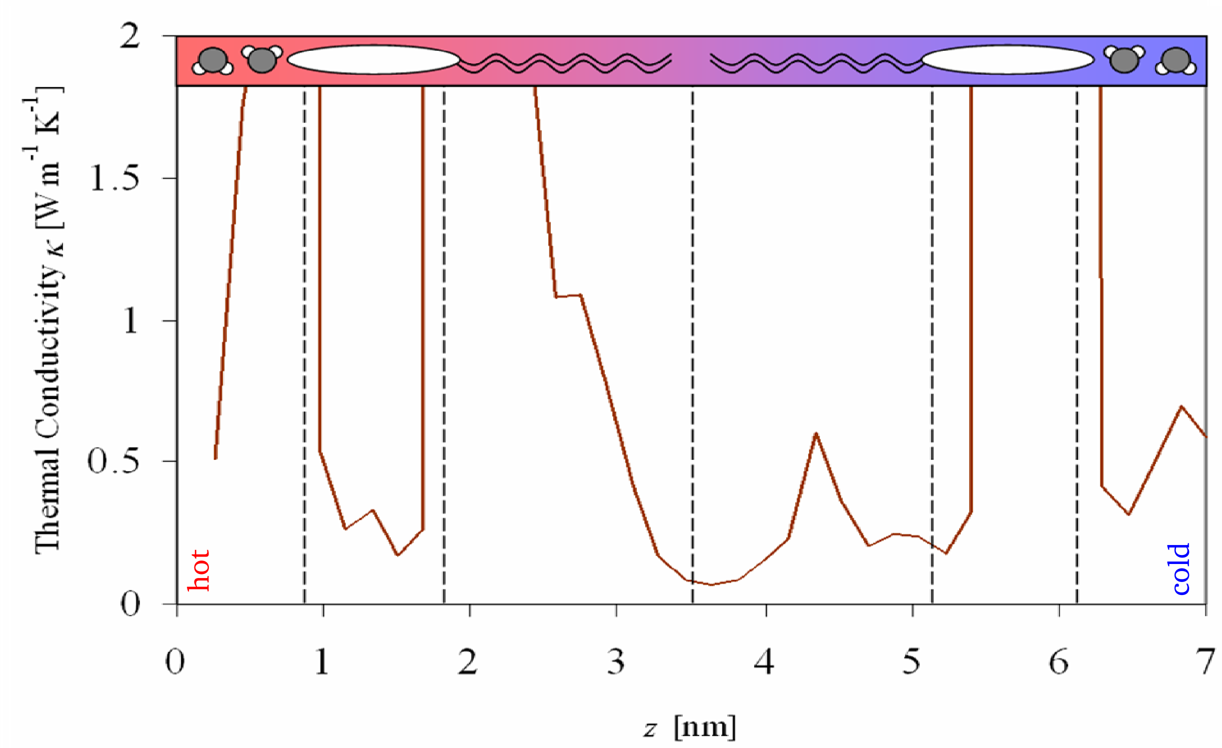

Fig. 2: The local thermal conductivity profile at an average temperature of T = 325 K with an exchange period w = 200. Applying the concept of local thermal conductivities leads to a structured profile across the membrane where we can assign the six regimes identified by density consideration. The dashed horizontal lines indicate the center of the system (line at 3.5 nm) and the average position of the innermost and the outpost head group molecule of the monolayers (determined by the phosphorus positions in equilibrium simulations).

- There are some symmetric trends in the profile as well as asymmetric ones. As expected, the water phases at the edges of the profile (far from the water-headgroup interface) show comparable thermal conductivities. In the middle of the membrane (at the tail-tail interface) a roughly symmetrical minimum can be found. But in the other regions of the profile, the behavior is asymmetric: in the water head-group interface we find a high thermal conductivity at the hot side of the system and a small one at the cold side. The same is true for the headgroup-tail interface and for the tail region. But at the headgroup region we observe exactly the opposite.

Note that high thermal conductivities lead to a low temperature gradient. The statistical uncertainty in the temperature profiles can then cause the temperature gradients to become apparently negative. Therefore for all the plots, negative thermal conductivities have been converted into arbitrarily large ones.

B) The influence of the density: As it is a well known fact that different densities of a system also change its thermal transport properties, the density profile is expected to explain some of the properties of the local thermal conductivity profile. We averaged both sides of the density profile of the full RNEMD simulation at T_{targ} = 325 K to get the profile through one double layer from the hot to the cold exchange slab (fig. 3). For the local densities, all atoms and their positions were counted, not the centers of mass of the molecules involved.

A comparison of the RNEMD density profile with the one from equilibrium simulations shows a general shift of all peaks towards the cold side. The overall density peaks are flatter and broader in the RNEMD profile. But it is not the lipid bilayer causing that change. With respect to the intersection point at 3.62 nm the two density profiles show mirror symmetry. They almost completely fall on top of each other within the line thickness of the plot. Only the two global maxima differ in their height (less than 5%) but this does not change the overall density profile of the RNEMD membrane. However the overall shape of the membrane density profile is different from what is has been at equilibrium conditions. Especially the head-group region becomes broader which can be explained by more flexible head groups. This also agrees with the water density profile indicating that more water can penetrate into the head group.

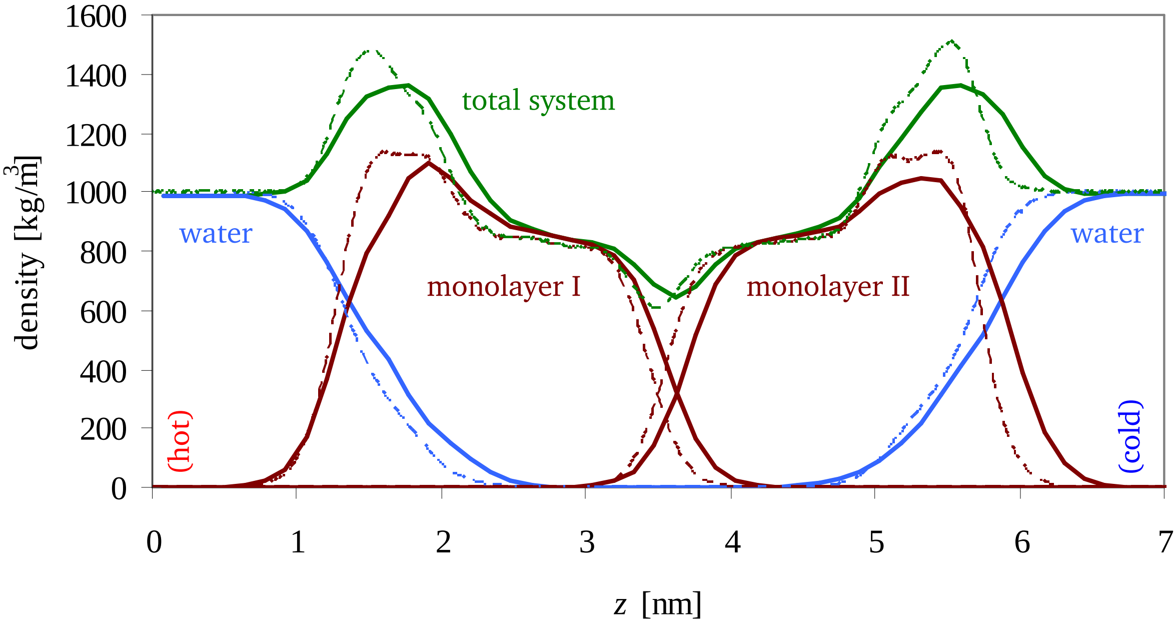

Fig. 3. The density profile of water molecules (blue), lipid molecules (brown), and the total density (green) across the system in equilibrium (dashed lines, [XXI]) and non-equilibrium (solid lines) simulations at an average temperature of 325 K. Applying a maximum temperature difference of 30 K to the system leads to significant structural changes in the lipid system. Expansion in the hot area and contraction in the cold one leads to an overall shift of the characteristic maxima peaks towards the cold side in the RNEMD profile compared to the equilibrium one. This results also in the deeper penetration of water molecules into the lipid bilayer.

Tab. 1: The assignment of the different regions in the simulation box

Region	**Equilibrium simulation [nm]**	**RNEMD simulation [nm]**
Water (hot region [*])	0 – 0.53	0-0.50
Water-lipid-interface	0.53 – 1.59	0.50 – 1.77
Lipid layer I	1.59 – 3.19	1.77 – 3.21
Lipid-lipid-interface	3.19 – 3.90	3.21 – 4.04
Lipid layer II	3.90 – 5.49	4.04 - 5.46
Water-lipid interface	5.49 – 6.56	5.46 – 6.73
Water (cold region [a])	6.56 – 7.1	6.73 -7.1

[*] hot and cold region are only distinguishable in RNEMD simulations.

Most of the deviation in the overall density profile and the apparent shift of the lipid profile is caused by the water phase. The higher temperature in the hot water phase leads to a general decrease of the water density by 1%. Thus, the expansion of the water on the hot side (on the cold side the density remains unchanged) leads to a total shift of the membrane and therefore to the previously observed shift of the minimum of the thermal conductivity. This shift influences the defined boundaries for the discussion of the membrane and the interfaces. They are summarized in tab. 1.

All these density-dependent observations proof structural changes to the membrane compared to the equilibrium simulations. But these changes are symmetrical with respect to the center of the membrane. While we can explain the shifting of the center of the profile with the shifting of the density profile we still have to explain the non-symmetrical thermal conductivity profile in the presence of a symmetrical density profile.

An asymmetrical thermal conductivity profile could be due to the presence of a thermal rectifier. Thermal rectification at well defined interfaces has introduced the concept of Kapitza thermal resistance [XXIV]. Recent studies on thermal rectification in nanosized systems explain the mechanics of heat flow in mass gradients [XXV]. We have performed additional calculations with a Lennard-Jones fluid to estimate the influence of possible thermal rectification by mass gradients in the DPPC system. Fig. 4 shows the density profiles across the four layers of the Lennard-Jones system (two layers of type

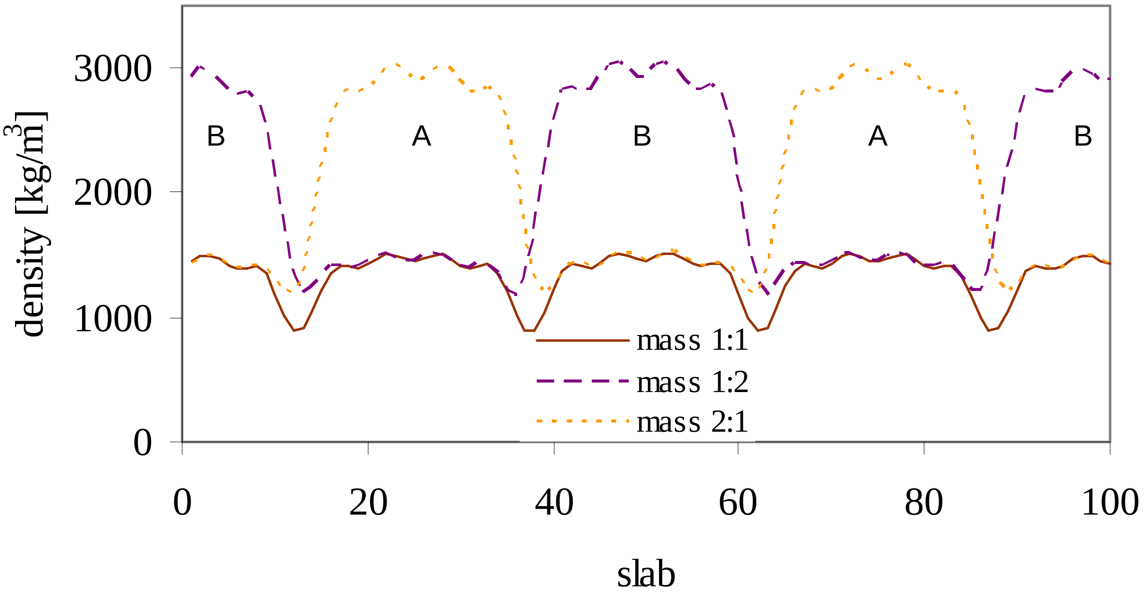

Fig. 4: Density profile of the test system of Lennard-Jones particles. The profiles of the ABAB structured system where A and B have the same mass (solid line), B has twice the mass of A (dahsed line), and A has twice the mass of B (dotted line) is the same within the resolution of this plot for RNEMD run with an exchange period of $w = 100$ and an exchange period of $w = 50$. The maximum over all deviation of the profiles for the different exchange periods is 1%. At the interfaces differences of up to 3.5% have been detected.

A and two layers of type B). Fig. 5 summarizes the local gradient in the temperature profiles (the inverse to the thermal conductivity) which can be directly compared. Note that the fluxes are the same (within 1.5%) in all systems.

At the interface, where the density is reduced, all setups exhibit a reduced heat flow. This agrees with the phonon theory which assumes that heat is mainly transported by collisions (fewer particles => fewer transport channels for the heat transport). There is a significant difference in the heat flow between a system with a uniform mass distribution and a system with a non-uniform one (more than 18 %) indicating that heat is much better transported across the interface if particles have similar masses. But the temperature gradients of the two non-uniform systems do not differ beyond the limit of statistical fluctuations. The theory mentioned above expects an enhanced thermal conductivity of the B = 2A system over the A = 2B one because heavy masses evoke low frequency vibrations which are dominant for the heat transport. Such an enhancement can not be observed here. This is not surprising since the systems in the article cited always contained a much higher mass difference than it was implemented in this setup. Here such an average effect is just too weak to be detectable.

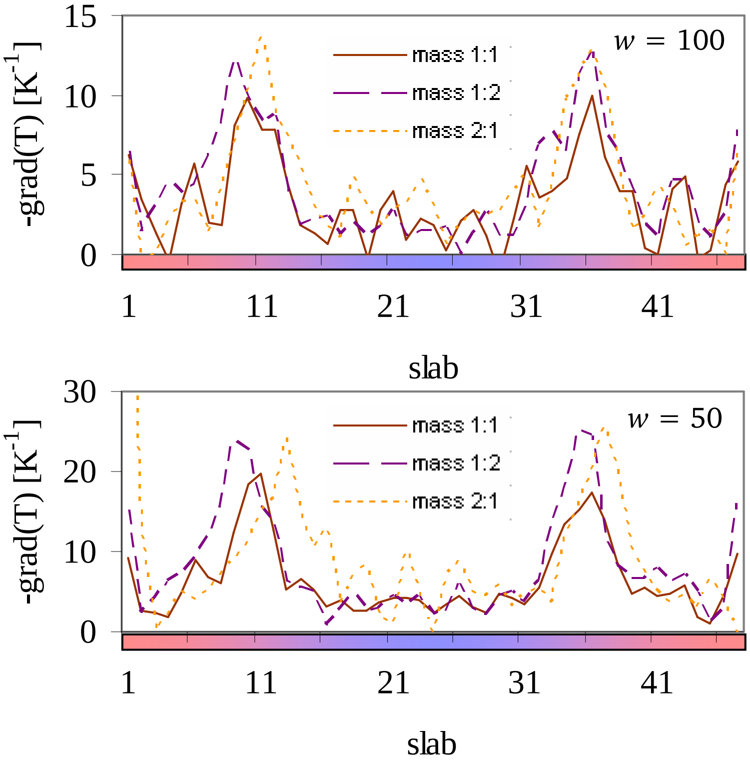

Fig. 5: Local thermal conductivities of Lennard Jones fluids at exchange periods of $w = 50$ and $w = 100$. In both cases three different ABAB systems have been studied. At the interfaces, the reference system with A and B at the same mass (solid line) shows at both exchange rates a reduced thermal conductivity compared to the two other system where B has twice the mass of A (dashed line) or A has twice the mass of B (dotted line).

These calculations showed that mass differences (and thus density differences) influence the local thermal conductivity. This supports the assumption of an asymmetrical thermal conductivity profile in the system. Thermal rectification at the density conditions of the DPPC bilayer system, however, are (if existent) very small and will not be detectable by the present RNEMD simulations. There must be another explanation for the asymmetry in the local thermal conductivity profile.

Nota bene, in the DPPC system not only mass densities but also particle densities are important. More particles provide more degrees of freedom to transport heat. In this way, water creeping into the membrane might bring some of its high thermal conductivity with it. Due to the asymmetry of the local thermal conductivity profile this type of analysis is not possible with the presented method.

C) Influence of the simulation setup: In order to quantify the effect of the asymmetry and to find its source we performed a series of different check simulations which varied simulation specific parameters.

Different average temperatures T_{targ} at different exchange rates are compared in fig. 6. It is obvious that an enhancement of the average temperature does not make the asymmetry vanish. It even does not change it in a significant way. Among the features which are conserved over the whole temperature range we emphasize the following three:

- The characteristic minimum in the middle of the bilayer, which was already discussed above, is conserved. It is the same at all temperatures and at all exchange rates. This indicates that this feature is dominant and robust.

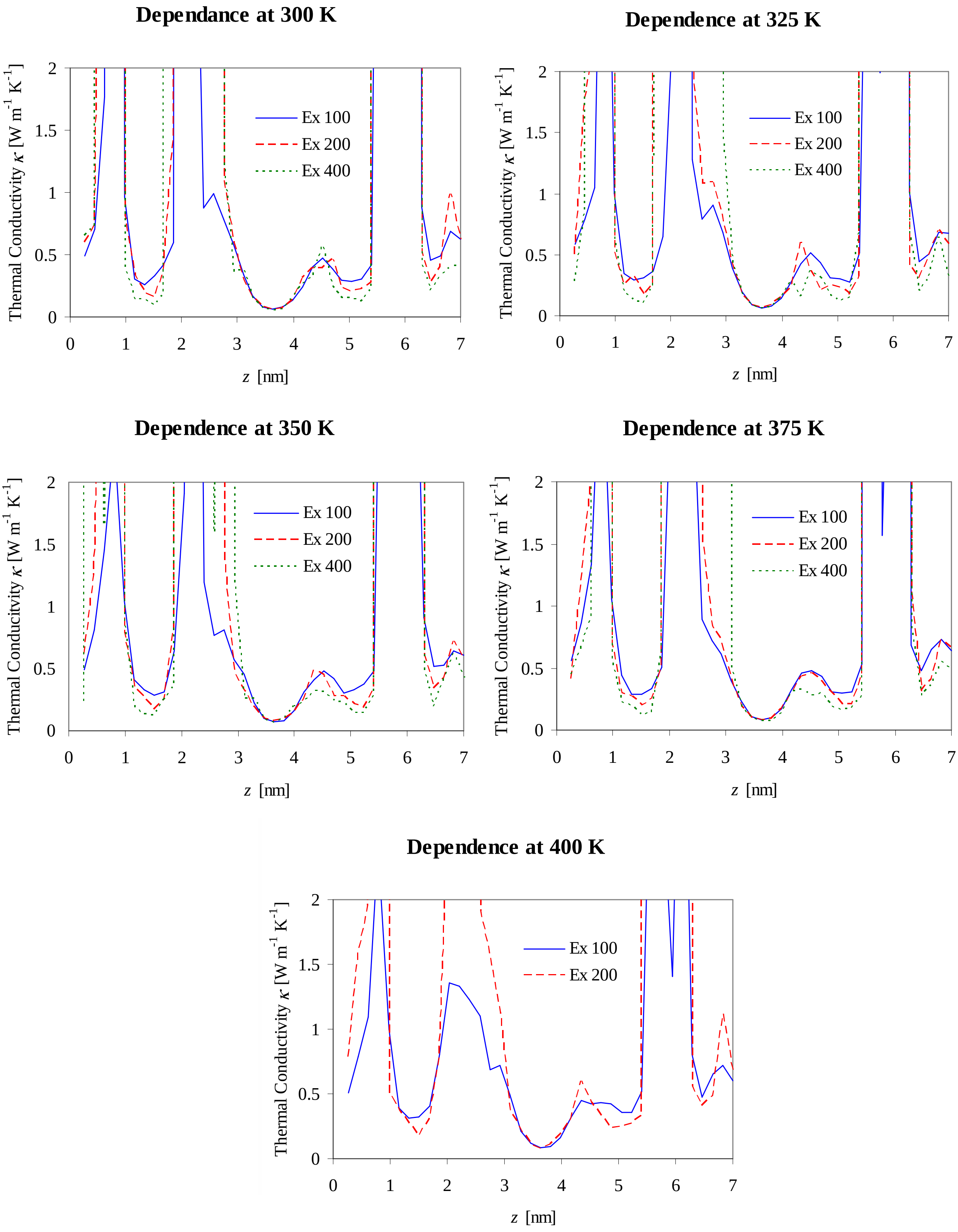

Fig. 6: Local thermal conductivity profiles of a DPPC bilayer at different average system temperatures (T = 300 K, T = 325 K, T = 350 K, T = 375 K, and T = 400 K) and at different exchange periods (w = 100, w = 200, and w = 400). The variation of the average temperature in the system as well as the variation of the exchange period (and thus a variation of the slop of the temperature gradient) does not influence the overall asymmetry significantly.

- The peak at about 4.5 nm with a maximum thermal conductivity of about 0.5 W m^{-1} K^{-1} is also a stable feature throughout all the studied temperatures. This peak can be assigned to the middle of the aliphatic lipid tail on the cold side. The high thermal conductivity is explained by the fact that heat transfer by vibrations is faster in the middle of a chain of atoms than at the ends. When having a closer look at the tail region of the other monolayer (at roughly 2.6 nm) there is a sub-structure (shoulder) hidden below the peak which suggests that this feature also exists at the hot side monolayer. But there is as a much stronger effect dominating the graphs so that a quantitative analysis of the peak is not possible.
- Concentrating on the ordering of the peaks at different exchange rates for each temperature, we discover two trends. Except for the middle of the bilayer we observe: The higher the exchange rate is, the smaller are the local thermal conductivities at the minima of the profiles (z = 1.3 nm, z = 5 nm) and the higher the exchange rates are, the faster they grow for the observed maxima (z = 0.8 nm, z = 2.2 nm, z = 5.9 nm). This fact is not in accordance with the theory of RNEMD which assumes that as long as the system responds linearly to the imposed flux, the observed thermal conductivities must be identical. The RNEMD studies in the literature show, that exchange rates of 100 to 400 in atomistic fluid models near room temperature never had been a problem for a linear response. On top of this, and most importantly, we observe the same thermal conductivities at the center of the membrane for all three exchange rates.

This last point needs further explanation. We have already seen (fig. 1) that smaller exchange periods cause higher temperature differences between the exchange slabs (ca. 40 K at w = 100; ca. 27 K at w = 200; ca. 10 K at w = 400). A direct consequence of this is that results at higher exchange rates and thus smaller gradients are more sensitive to statistical fluctuations and external influences. The first point was averaged out by long enough simulation times. The second one still remains to be investigated.

An increase of the time step in the simulation serves as test of the influence of integration errors. The larger the time step the larger is the distance which an atom travels before the forces are reevaluated. This serves as a test to see whether accidental huge forces in the system lead to the observed local thermal conductivity profile. We doubled the step size decreasing the exchange rate (measured in time steps) accordingly to insure a constant exchange rate per time. The resulting thermal conductivity profiles are shown in fig. 7.

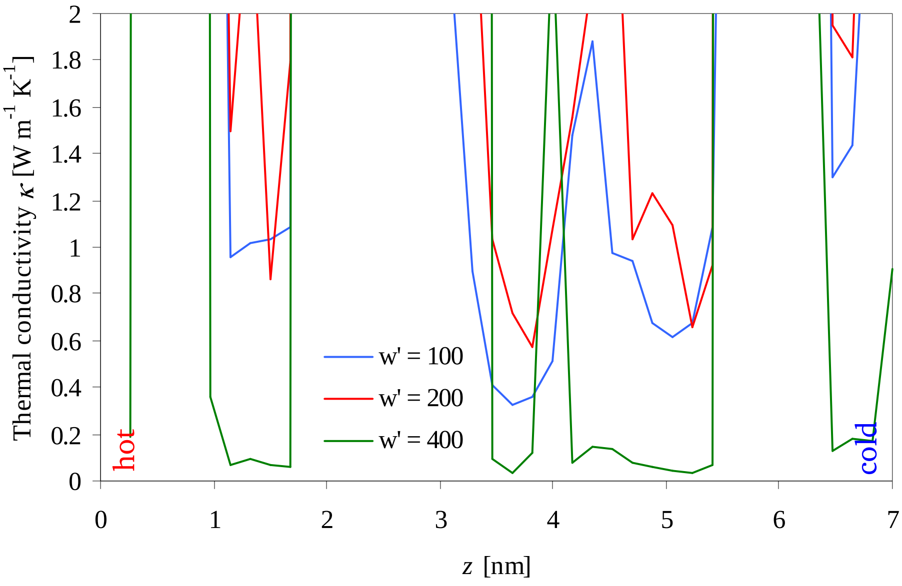

Fig. 7: Local thermal conductivities from test simulations with the time step (t = 0.004 ns) twice as large as in the original simulations. Therefore to compare exchanges with the same time period in between w'= 100 has to be compared with w = 200 and w' = 200 with w = 400. Doubling the time step leads to significant changes in the minima of the local thermal conductivity profiles. But the overall shape an especially the asymmetry of the profiles are also conserved in this case.

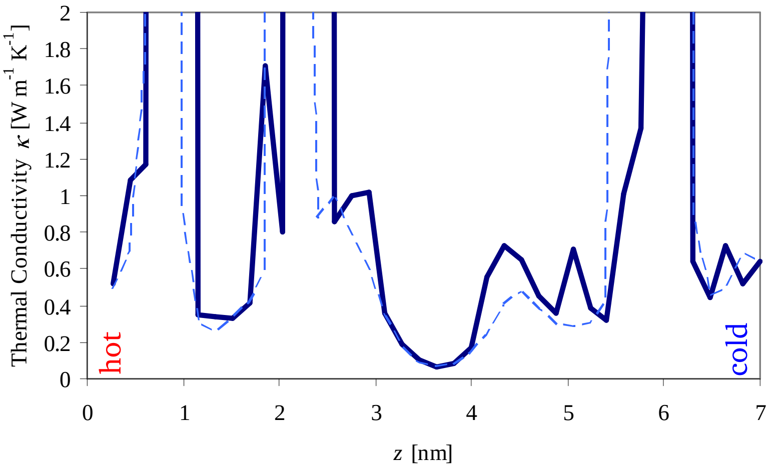

Fig. 8: Local thermal conductivities (solid thick line), treating the electrostatic interactions by conducting boundaries, i.e. a virtually infinite reaction field parameter ($_{RF}$ = 100000, T_{targ} = 300 K, w = 100). This profile differs from the one at standard conditions ($_{RF}$ = 54; dashed line). The local maxima next to the center of the membrane are shifted toward the middle of lipid bilayer indicating a structural change due to the changed force field parameter. The typical ordering of the maxima and minima however is conserved. Thus the reaction field parameter is also not the key to understanding the asymmetry of the local thermal conductivity profile.

Indeed we recognize an overall enhanced thermal conductivity for simulations with a high exchange frequency (a small exchange period *w*'). Due to the larger displacements of the molecules heat is transferred faster across the system. Only when the temperature gradient becomes small enough (at w' = 400 the difference between hot and cold slab is only 5 K) the profiles agree again with what was observed at smaller time steps. This artifact can easily be avoided by keeping the initially chosen step sizes of 2 fs. But the asymmetry of the profile was not changed at all, indicating that the step size is not responsible for this feature.

The last two tests deal with the description of the long range forces. Applying a cutoff radius and assuming a dielectric mean field beyond it can lead to artifacts. Thus, we tested the influence of the reaction field dielectric. A reduction of the applied reaction field dielectric constant ε_{RF} = 54 (the value the force field in use was parameterized with [XIX]) to 1 is equivalent of cutting all forces exactly at the cutoff radius. This necessarily leads to simulation artifacts. We tested the opposite extreme to answer the question whether an interaction with conducting boundaries (achieved by a very high reaction field constant ε_{RF} = 100 000) makes the asymmetry in the local thermal conductivity profile go away. A comparison of the corresponding profiles can be found in fig. 8.

We identify the same ordering of the maxima and the minima in both local thermal conductivity profiles. Despite all similarities they differ in some details. The most important feature is the shift of the local maxima next to the center of the membrane towards the middle of the lipid bilayer. Although this shift shows that the rule of thumb for homogeneous fluids that all ε_{RF} above 10 yield to the practically the same results does not apply here, the effect on the local thermal conductivity profile is symmetrical with respect to the middle of the membrane. The choice of the dielectric field parameter is not responsible for the asymmetry of the local thermal conductivity profile.

The second test for description of the long range force is the variation of the cutoff radius itself. Decreasing the cutoff radius from 1.2 nm to 0.8 nm leads to a surprising result: we observed a dramatic increase of the temperature gradient resulting in temperatures above 1150 K in the hot and below 10 K at the cold side. Accordingly the density in the hot area was almost reduced to half of the density in the cold slab. This result can be explained by local heat sources in the water left and right of the partially insulating membrane. The truncation of the long range interactions of the atoms with partial charges (mostly in the water molecules and to a lesser extent in the lipid head groups) leads to a local heating of these regions. This local heating is eliminated by the Berendsen thermostat which scales the velocities of *all* atoms and thus effectively introduces a local heat sink in the middle of the membrane. This is also visible in equilibrium simulations. When the RNEMD exchange starts to move kinetic energy from one side of the membrane a very steep gradient is built up since a lot of instantly generated thermal noise is also transported from the cold to the hot slab. Eventually the density of the system gets distorted so much that parts of the headgroups can enter the exchange slab. Finally the exchange of kinetic energy only between particles with the same mass (in this setup we assumed just to exchange kinetic energy of water molecules) fails and the RNEMD algorithm breaks down.

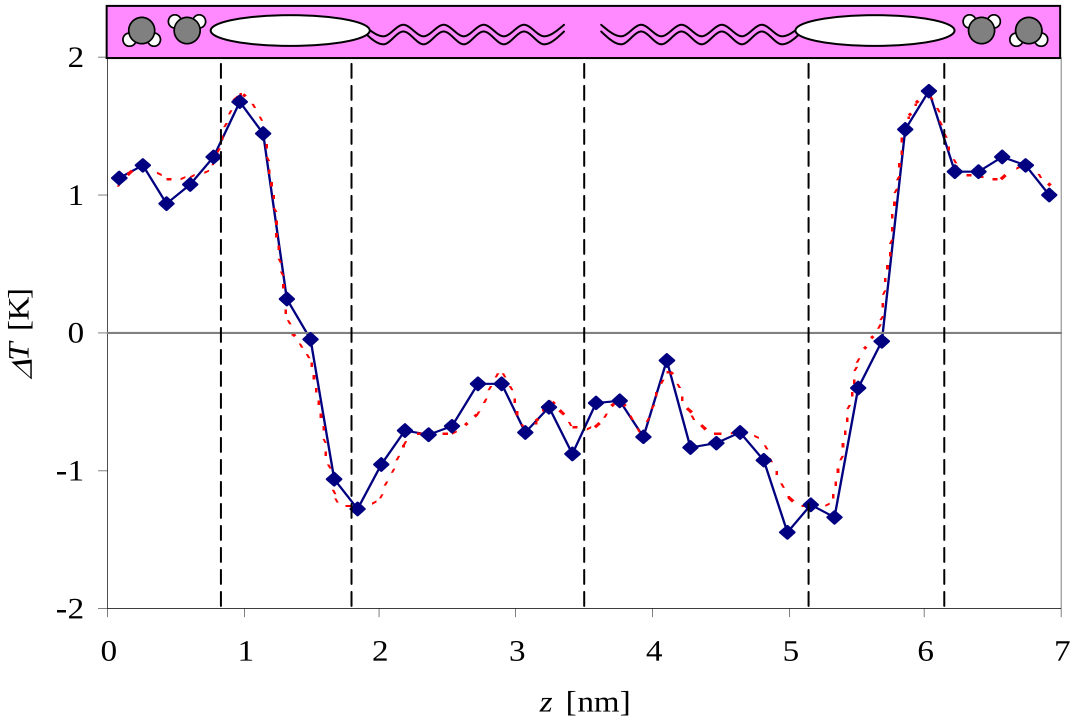

Fig. 9: Deviations of locally calculated temperatures from the average temperature in equilibrium simulations of the membrane with T_{targ} = 325 K: The region in the middle of the lipid bilayer is below the average while the one in the water is above. A pronounced heating area can be found at the water-headgroup interface and the head-group tail contact region shows a pronounced heat sink behavior. The dashed line indicates an average over both symmetric parts of the simulation box connected by splines.

When having a closer look at properties of structured systems which do not directly depend on temperature, the non-uniform temperature distribution is often overlooked. But in the current studies this was found to be a dominant feature of the simulation. To quantify the local heating the local temperature profile has been extracted from more than 30 ns equilibrium simulations of this system, which have been performed for the studies of mass transport through the membrane [XXI]. This amount of data is necessary to extract from the thermal noise the temperature profile presented in fig. 9.

We identify the local heat sources in the water phase. An even stronger heating can be observed at the headgroup-water interface (at z = 1 nm and z = 6 nm). Local cooling takes place in the lipid tails where the atoms contain no partial charges and therefore do not generate spurious heat from truncating electrostatic long range forces. The strongest heat sink, however, is observed at the head group region next to the tail groups. Overall we observe a deviation of ± 1.5 K from the average temperature. Modulations of the RNEMD temperature profile by additional heat sinks/heat sources in this order of magnitude has a significant impact on the temperature gradient and thus on the observed local thermal conductivities.

D) The final interpretation of the thermal conductivity profile: Does the existence of these heat sources and heat sinks fully explain the three largest peaks in the thermal conductivity profiles observed in figs. 2 and 6? Indeed, it does. With all the observations from above we can now go through the exemplary profile of fig. 2 from left (hot) to right (cold) and interpret it completely:

- z = 0 nm to z = 1 nm (water phase until the middle of the water-headgroup interface): The apparent increase in the thermal conductivity is an artifact of the truncation heating. While the water phase is globally a heat source, the maximum heat source at about z = 1 nm produces heat which flows to the right, but also to the left side. This heat which flows “backwards” in the global context causes the total temperature gradient to flatten which incorrectly implies a large thermal conductivity. In fact, at high exchange periods (w = 400) and a small global gradient, the truncation heat becomes dominant in the vicinity of the heat source. Thus the negative temperature gradient there is not a result of bad statistics but indicates a heat flux in the opposite direction.

- z = 1 nm to z = 1.7 nm (water-lipid interface): Although the concentration of water in this region is steadily decreasing the dominant part for the local thermal conductivity in this region is again the temperature profile from the truncation heating. It exhibits a rapid decrease in temperature. This steep gradient dominates again the one invoked by the global heat flux and thus we see a thermal conductivity in fig 2 which is below the correct value.
- z = 1.7 nm to z = 3 nm (head group to middle of tail group): Knowing about the heat sink at roughly z = 1.9 nm allows to argue like in the region from z = 0 nm to z = 1 nm. Heat flows against the totally imposed heat flux from the middle of the membrane to the left side. This leads to flat gradients and corresponding apparently high thermal conductivities. But we also identify the peak at z = 2.7 nm (discussed above) which effectively is an important real feature of the thermal conductivity profile of the membrane.
- z = 3 nm to z = 4.1 nm (lipid-lipid interface): The middle of the membrane is also the place where the system is closest to the target temperature T_{targ}. Heat fluxes due to local heat sinks or heat sources are negligible and in the middle the truncation heat flux to the left and the one to the right side cancel each other. In this region the globally imposed heat flux is the dominating effect. The thermal conductivity at this point is least influenced by artifacts.
- z = 4.1 nm to z = 5.4 nm (middle of the tail group to head group): Being now on the cold side of the membrane means primarily that the heat which is dragged to the local heat sink at about z = 5.2 nm flows in the same direction as the heat flux imposed by RNEMD. This results in an observed steeper gradient corresponding to a smaller thermal conductivity than there actually is. In this fact we also find the explanation why the physically important peak at z = 4.5 nm is well exposed while it is covered in the opposite monolayer.
- z = 5.4 nm to z = 6.3 nm (lipid to water-lipid interface): In this peak two different mechanism are hidden. From z = 5.4 nm to z = 6.0 nm the truncation heat profile shows a pronounced increase in temperature which dominates the overall temperature profile resulting in very flat or even negative gradients. Incorrectly, as already discussed above, these effects lead to erroneously very high local thermal conductivities. From z = 6.0 nm to z = 6.3 nm an additional heat flow which originates at the heat source at z = 6.0 nm in the direction of the global heat flux leads to an apparently enhanced local thermal conductivity. Note that in fig. 6 some of the profiles show intermediate data points in z = 5.4 nm to z = 6.3 nm. They are not due to statistical uncertainties of the data, but can be attributed to the change of one of the artifacts to the other.
- z = 6.3 nm to z = 7.1 nm (lipid-water interface to water phase): This region is under the influence of the additional heat from the heat source at z = 6.0 nm. The reduced thermal conductivity of water in the vicinity of the membrane compared to its bulk value [XXIII] results from that and not from a physical effect.

A good understanding of these undesirable effects is the first step to eliminating them from the results. Several strategies have been attempted to extract the pure linear response of the system to the externally applied flux.

Assuming the heat production due to the truncation errors is the same in the equivalent parts, geometrical averages can be made. Applying an external flux to the system leads to an odd temperature profile along the z axis (point symmetry with respect to the center of the bilayer). The structure of system as illustrated by the density profile is of even symmetry (mirror symmetry with respect to the center of the bilayer) and the deviations in the temperature profile caused by truncation errors show an even symmetry as well. If the total temperature profile is just a superposition of the two contributions (RNEMD and thermal noise) then they can be separated again. Use the point symmetry to average the total function with its image which is rotated by 180° and average over the two to get the strictly uneven RNEMD temperature profile. For example: heat generated by truncation at z = 1 nm (fig. 9) flows in the (hot) water phase against the global heat flow. At the cold side the heat generated by the mirror image heat source flows with the global heat flow. When averaging the heat flows of the two water phases with respect to the same direction of the global heat flow the truncation-generated heat flows cancel each other an all that remains is the global heat flux. Fig. 10 shows the

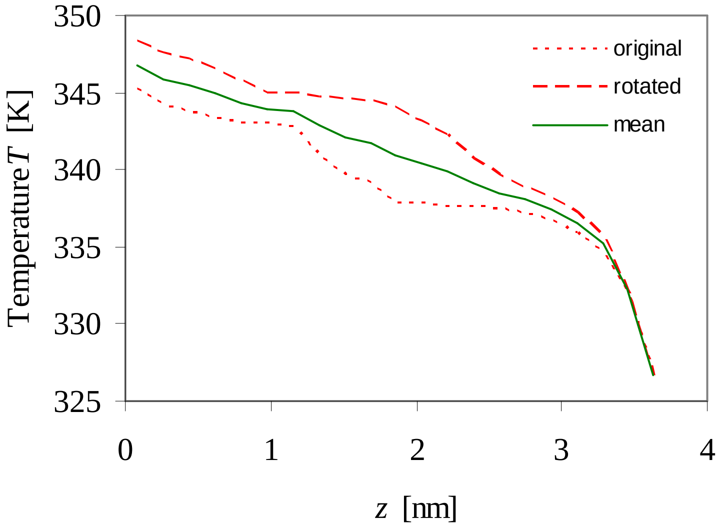

Fig. 10: The antisymmetry of the local thermal conductivity within the membrane at an average temperature of T = 325K and an exchange period of w = 100 time steps. The right part of the temperature profile is rotated at the center of the profile by 180°. The average of the rotated (cold side) profile and the not rotated (hot side) profile shows a straight line up to 3 nm. Beyond this point the tail groups of the two parts interact with each other and another temperature gradient corresponding to a different local thermal conductivity is visible.

results of one such averaging. We immediately identify two regions with completely different thermal conductivity properties: the tail-tail-interface (z > 3.3 nm) of the bilayer (roughly $\kappa = 0.085$ W m^{-1} K^{-1}) and the rest of the system including water, headgroups and tailgroups (roughly 0.52 W m^{-1} K^{-1} < κ < 0.83 W m^{-1} K^{-1}). Although these findings agree with the tendencies found previously in this study, they are only rough estimates. Compared to the previous results the resulting local thermal conductivity profile lacks the characteristic profile structures such as the peak of increased thermal conductivity in the tail regions. Thus this method is useful to remove the influence of the local heating efficiently to get good estimates for local thermal conductivities. But its lack of accuracy destroys local information and leads to smoothened results.

Another approach to separate the intermixed profiles assumes that the heat production and the heat removal by the cutoff/thermostat system do not depend much on the temperature. Therefore it can be considered constant over the internal temperature differences found here (maximum 40 K). This leads to the idea of a base line correction. But this approach did not succeed in simplifying the local thermal conductivity profiles (not shown).

Much more sophisticated methods could lead to a more detailed understanding of the truncation-heating process and its impact on the total heat flow. In analogy to the NEMD setup proposed by Terao and Müller-Plathe [XXVI] the exact knowledge of the heat sources an heat sinks (as well as the heat transferred between them) could solve that problem as well. The mathematical task of solving differential equations with the given temperature profile as well as the implementation of the additional code to actually measure the heat transfer induced by the thermostat are highly complex. It is just more likely that the system will be studied under RNEMD with a simulation package which does not rely on cutoffs and reaction fields to describe long range interactions

Note that in theory, the extraction of the local thermal conductivities from the temperature profile in fig. 9 is possible when knowing the heat which the thermostat removes from the system on average. Together with the local particle density and the local constraint density the local cooling rates can be determined. When combining these results with Fourier II one should be able to vary the local heating rates and the local thermal conductivities until fig. 9 is reproduced. Note also that the conscientious development of the method to this inverse problem is in the order of a master thesis and is out of scope of this contribution.

E. Barriers to heat flow in biomembrane assemblies. Finally, what biologically relevant data can be extracted from these simulations? The insight into the heat conduction properties of the membrane at the water-headgroup contact region is limited (results summarized for T_{targ} = 325 K). It is restricted to observations of lower limits for the local thermal conductivities in the headgroup-water interface (κ > 0.25 W m^{-1} K^{-1}) and in the tail groups close to the head groups (κ > 0.25 W m^{-1} K^{-1}) or to general estimates for the thermal conductivities in the whole system except the tail-tail interface (0.52 W m^{-1} K^{-1} < κ < 0.83 W m^{-1} K^{-1}). The region close to the center of the membrane however was easily accessible by the method. We observed the peaks in the middle of the lipid tails which have a local thermal conductivity of $0.5\ \mathrm{W\ m^{-1}\ K^{-1}} < \kappa < 1.0\ \mathrm{W\ m^{-1}\ K^{-1}}$ which therefore conduct heat as good as bulk water or even better. The overall limiting factor to the heat transfer of a biological bilayer system remains the region between the monolayers. The lowest density on the simulated setup correlates with the lowest number of transport channels which are accessible for heat transfer. To elucidate the effective local thermal conductivities (and their temperature dependences) fig. 11 summarizes the local thermal conductivities calculated at simulations with exchange period $w=100$ at different temperatures. We observe minimum thermal conductivities of 0.063 $\mathrm{W\ m^{-1}\ K^{-1}}$ at 300 K gradually increasing up to 0.083 $\mathrm{W\ m^{-1}\ K^{-1}}$ at 400 K. Over the whole temperature range, this is an increase by 25 % while the thermal conductivity of the neighboring peaks remains the same. This is interesting because the minimum density in this area increases with temperature (from 640 $\mathrm{g/cm^3}$ at 300K to 679 $\mathrm{g/cm^3}$ at 400K). This is in accordance with other systems where the thermal conductivity has been shown to increase with increasing density, i.e. the number of degrees of freedom per volume.[XII, XXVII] The deeper interpenetration of the two lipid monolayers enables a better heat transfer. In contrast, the vibrational modes in the aliphatic chains of the lipid tails are governed by the stiff intramolecular potentials and are not susceptible to changes of the environmental temperature.

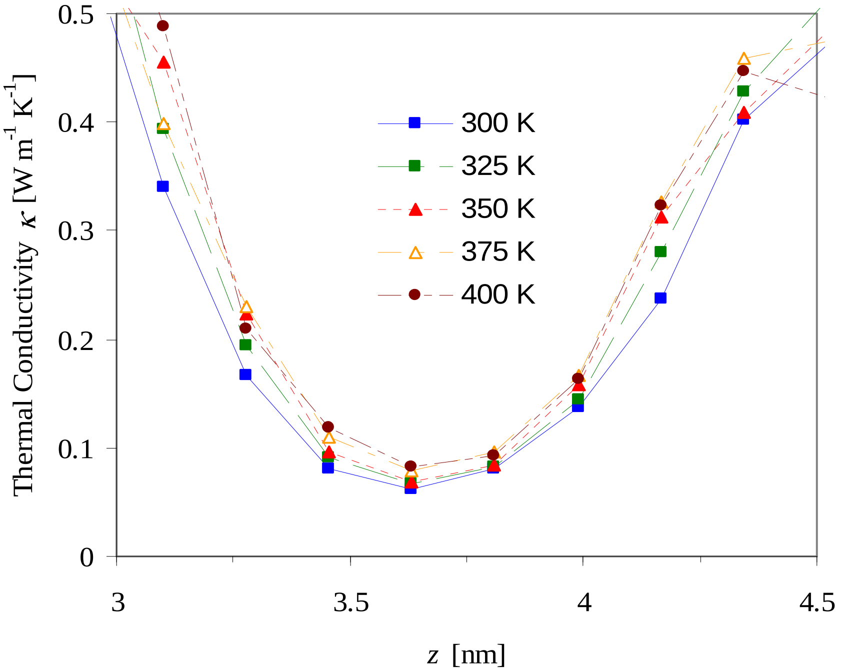

Fig. 11: Local thermal conductivities in the tail-tail interface, RNEMD simulations with an exchange period of $w = 100$. Although these simulations only computed a total simulation time of 6 ns, the local gradients are already sufficiently converged to derive the correct ordering of the local thermal conductivities at different temperatures near this interface.

V Conclusions

Reverse non-equilibrium molecular dynamics simulations have been proven to show strong artifacts when applied to highly ordered bilayer systems. The main issue is the existence of local heat sources and heat sinks introduced by calculation of long ranged electrostatic forces. We demonstrated in detail the effects of different simulation parameters on the local thermal conductivity profiles of the DPPC bilayer.

Several potential ways around this problem have been discussed. The heuristic idea of canceling the heat flow in the wrong direction by rotating the system has been shown to remove the effect efficiently while baseline corrections and an explicit treatment of additional heat sources were not successful or too complicated.

But what points of biological relevance can be learned from these simulations? Is the local thermal conductivity really asymmetric across a bilayer? While we have shown several arguments why and how the local thermal conductivity profiles are mainly distorted by cutoff effects, at this point asymmetry cannot be excluded completely. However we have proven that the most important, most heat-flow-hindering part of the membrane is the interlayer region where the lipid tails meet. There, the local thermal conductivity is symmetric and can be roughly estimated from our calculations. RNEMD allows us also to estimate the local thermal conductivity over a wide range of biologically relevant temperatures.

As powerful as RNEMD has been in the past decade to predict thermal conductivities for homogeneous systems, expanding the method to heterogeneous, highly ordered systems has hereby been proven to be difficult. The complications arise not from the RNEMD method itself, but from the heterogeneity of the system, which entails a non-uniform artificial heat source. In the present example, this effect is particularly severe, since a very polar part of the system (water plus zwitterionic head groups) was very prone to heat generation by thermal noise, whereas another part (aliphatic part) was not. The uncontrolled heat sources and heat sinks would corrupt any nonequilibrium and even equilibrium scheme. Thus the future work on this topic is outlined clearly. The influence of additional heating and cooling has to be eliminated or to be correctly incorporated in the calculations. This can be achieved by implementing different methods to cope with long range forces particle without the artifact of local heating due to truncation errors such as mesh Ewald summation into YASP or implementing the RNEMD algorithm into simulation suites which already have those methods implemented.

References

[I] J.G. Flores, ed. D.O. Cooney, *Biomedical Engineering Principles: An Introduction to Fluid, Heat and Mass Transport Processes*, Marcel Dekker, Inc., New York (1976)

[II] J.D. Hardy, E.F. DuBois, Proc. Nat. Acad. Sci. 23 (1937) 624-631

[III] R.J. de Dear, E. Arens, Z. Hui, M. Oguro, International Journal of Biometeorology 40 (1997) 141-156

[IV] B. Lee, DSTO-TR-0849 Aeronauticals and Maritime Research Laboratory (1999)

[V] D.N. Sørensen, L. K. Voigt, Building and Environment 38 (2003) 753-762

[VI] H. Heerklotz, J. Phys.: Condens. Matter 16 (2004) R441-R467

[VII] V.P. Ivanova, I.M. Makaroy, T.E. Schaffer, T. Heimburg, Biophys. J. 84 (2003) 2427-2439

[VIII] F. Müller-Plathe, J. Chem. Phys. 106 (1997) 6082-6085

[IX] D. Bedrov, G.D. Smith, J. Chem. Phys. 113 (2000) 8080-8084

[X] M. Zhang, E. Lussetti, L.E.S. de Souza, F. Müller-Plathe, J. Phyz. Chem B 109 (2005) 15060-15067

[XI] T. Terao, E. Lussetti, F. Müller-Plathe, J. Phys. Chem. B 111 (2007) 11516-11523

[XII] E.A. Algaer, M. Alaghemandi, M.C. Böhm, F. Müller-Plathe, J.Chem. Phys. A (2009) DOI: 10.1021/jp9009492

[XIII] E. Rossinsky, F. Müller-Plathe, J. Chem. Phys 130 (2009) 134905

[XIV] M. Alaghemandi, E.A. Algaer, F. Leroy, M. Böhm, F. Müller-Plathe Nanotechnology 20 (2009) 115704

[XV] T. Müller, F. Müller-Plathe, Chem. Phys. Chem. 10 (2009) 2305-2315

[XVI] F. Müller-Plathe, Comput. Phys. Commun. 78 (1993) 77-94

[XVII] K. Tarmyshow, F. Müller-Plathe, J. Chem. Inf. Model. 45 (2005) 1943-1952

[XVIII] F. Müller-Plathe, P. Bordat, Lect. Notes Phys. 640 (2004) 310-326

[XIX] I. Chandrasekhar, M. Kastenholz, R. D. Lins, C. Oostenbrink, L.D. Schuler, D.P. Tielemann, W.F. van Gunsteren, Eur. Biophys. J. 32, (2003) 67-77

[XX] W.F. van Gunsteren, S.R. Billeter, A.A. Eisenring, P.H. Hühnenberger, P. Krüger, A. E. Mark, W.R.P. Scott I.G. Tironi, *Biomolecular Simulation: The GROMOS96 Manual and User Guide*, vdf Hochschulverlag AG Zuerich, Groningen (1996)

[XXI] T. Müller, F. Müller-Plathe, J. Hazard. Mat. 138 (2009) 13-24

[XXII] W. Scott, F. Müller-Plathe, W.F. van Gunsteren, Mol. Phys. 82, (1994) 1049-1062

[XXIII] T. Müller. M. Al-Samman, F. Müller-Plathe, J. Chem. Phys. 129 (2008) 014102

[XXIV] P. L. Kapitza, J. Phys. (USSR) 4 (1941) 181

[XXV] M. Alaghemandi, F. Leroy, F. Müller-Plathe, M. Böhm, submitted to J. Chem. Phys.

[XXVI] T. Terao, F. Müller-Plathe, J. Chem. Phys. 122 (2005) 081103(1-3)

[XXVII] E. Lussetti, T. Terao, F. Müller-Plathe, J. Phys. Chem. B 111 (2007) 11516-11523

5. Folgerungen und Ausblick

Obwohl Computersimulationen in den letzten Jahrzehnten ein fester Bestandteil zur theoretischen Untersuchung von biologischen Systemen geworden sind, bleiben noch viele Fragestellungen bezüglich Transportphänomenen an Membranen offen. Diese Arbeit behandelt auf breiter Basis verschiedenste Aspekte von Massen-, Impuls- und Wärmetransport durch Zellmembranen.

Bei dem Vergleich der Dynamik von Senfgas und Heptan wurde gezeigt, dass die beiden Moleküle nicht nur eine unterschiedliche Affinität zu verschiedenen Regionen der Membran aufweisen, sondern auch innerhalb der Membrane unterschiedlich flexibel sind. Aufgrund dieser Beobachtungen konnte erklärt werden, weshalb sich Senfgasmoleküle bei gleicher externer Kraft schneller durch eine Membran bewegen als Heptanmoleküle. Eine Analyse der für die Diffusion am hinderlichsten Regionen, welche für die verschiedenen Moleküle unterschiedlich waren, rundete das Bild von der Dynamik des Penetrationsprozesses von den „united atoms“ Molekülen durch die Membran ab.

Die Fragestellung nach dem Transportweg bietet eine Möglichkeit zur Neutralisierung von Senfgas. Dafür muss in Zukunft von biologischer Seite her geklärt werden, ob die Diffusion des Zellgiftes durch die Zellwände wie angenommen der entscheidende Transportweg ist, oder ob Diffusion durch Kanäle (z.B. für Ionen) ebenfalls berücksichtigt werden muss. Ausserdem kann das Problem mit theoretischen Methoden von einem energetischen Ansatz her betrachtet werden. Die Berechnung von Energiebarrieren erlaubt das Verifizieren der hier gefundenen Diffusionswahrscheinlichkeiten.

Zukünftige systembiologische Ansätze, welche einen Transport des Giftes durch die Haut resp. im ganzen Körper von einem globaleren, medizinisch-pharmazeutischen Gesichtspunkt her modellieren, finden in den hier ermittelten Werten erste Angaben über die Permeabilität der Membran bezüglich Senfgas und somit einen der grundlegenden Parameter zur Beschreibung des Transportvorgangs.

Während die Untersuchung des Massentransportes auf bereits fest etablierten Methoden beruhte, wurde zur Untersuchung des Impuls- und des Wärmetransportes erstmals die „reverse non-equilibrium molecular dynamics“ (RNEMD) Methode verwendet. Trotz diverser Arbeiten verschiedener Kollegen mit diesem Algorithmus, stellte sich für das spezielle System einer Membran die Frage nach der Anwendbarkeit der Methode. In einer vorbereitenden Untersuchung konnte anhand von flüssigen Phasen kleiner Moleküle gezeigt werden, dass die Regel, welche bereits für die Thermostaten gefunden wurde, auch für die Manostaten Gültigkeit hat: Innerhalb der Fehlergrenzen stimmen die Resultate von Simulationen mit und ohne Manostat miteinander überein. Dabei muss aber als eine der grösstmöglichen Fehlerquellen darauf geachtet werden, dass bei einem Wechsel von einem System mit konstantem Volumen zu einem System mit konstantem Druck die Kraftfeldparameter so gewählt sind, dass sich die Dichte des Systems insgesamt nicht ändert. Ansonsten ist auch mit Veränderungen der Scherviskosität, die eine Funktion der Dichte ist, zu rechnen. Ebenfalls sei hier nochmals darauf verwiesen, dass die RNEMD Methode nur für Systeme mit konstanter Energie, konstantem Volumen und konstanter Temperatur hergeleitet werden kann. Wenn es das zu simulierende System erlaubt, sollte man deshalb wenn möglich auf diese Bedingungen zurückgreifen.

Unter Anwendung der obigen Resultate wurde die Scherviskosität der DPPC Biomembran untersucht. Die Einführung des Konzepts einer lokalen Scherviskosität erwies sich als nützlich, um das rheologische Verhalten einer Membran unter äusserem Scherfluss lokal aufgelöst zu beschreiben. So zeigte sich, dass die lokale Scherviskosität in der wässrigen Phase beinahe bis an den Rand der Simulationsbox noch durch die Membran beeinflusst wird. Im Bereich zwischen den Monoschichten wurde unter der Berücksichtigung der Verschlaufung der Lipidschwänze eine Scherviskosität hergeleitet, welche in einer vergleichbaren Grössenordung lag wie jene, die durch Coarse-Grained Rechnungen bestimmt wurden. Damit liegen die theoretisch ermittelten Werte aber um mindestens eine Grössenordung und somit markant unter den im Expermient gemessenen Scherviskositäten. In Zukunft wird die Frage zu klären sein, ob die Experimente nur die Scherviskosität messen oder ob noch weitere Effekte mitspielen und ob die Simulation von solch kleinen Modellsystemen ausreichend ist. So ist bekannt, dass die Membranen undulieren, was unter der heutigen Rechnerkapazität in einem komplett atomistischen Modell noch nicht in ausreichend langer Zeit gerechnet werden kann. Ebenso wurden aus Effizienzgründen bei den Rechnungen bedeutend grössere Scherraten als in den Experimenten angelegt, wodurch ein nicht lineares Verhalten der Scherviskosität eintreten könnte. Es bleibt abzuwarten, was zukünftige Simulationen mit bedeutend leistungsstärkeren Computern zur Klärung dieses Sachverhaltes beitragen können.

Auch diese Forschungsresultate werden in systembiologischen Betrachtungen auf weniger gut aufgelösten Grössenskalen herangezogen werden können. Gröbere Membranmodelle, deren Beschreibung einen Viskositäts- oder Reibungsparameter enthalten, finden in diesen Resulaten erstmals auf atomistischem Niveau berechnete Vergleichswerte. Diese vom Experiment unabhängigen und von den verglichenen, theoretischen Berechnungen mit den Experimenten am besten übereinstimmenden Parameter bieten eine fundierte Grundlage zur Beschreibung von Biegungsprozessen von Membranen (z.B. bei Vesikelbildung oder Endocytose).

Während dem Bestreben, die RNEMD Methoden erstmals auch für Wärmetransportuntersuchungen an Membranen anzuwenden, sind wir auf Probleme gestossen, deren Eingrenzung auch für zukünftige Simulationen mit dieser Methode nützlich sein wird. In dem entsprechenden Kapitel wurde nachgewiesen, dass das hohe Maß an Heterogenität entlang der Achse durch die Membran zu Artefakten in den Simulationen führen kann. In diesem Fall sorgt die lokale Aufheizung durch Rundungsfehler am Cutoff-Radius für einen zusätzlichen Wärmefluss neben dem durch die Methode induzierten. Der Effekt wurde für das hier verwendete System beschrieben und sein Einfluss unter verschiedenen Bedingungen getestet. Detailierte Untersuchungen haben gezeigt, dass die Existenz der lokalen Wärmequellen und Wärmesenken ausreicht, um die Artefakte genau zu beschreiben. Aufgrund der vollständigen Interpretation des lokalen Wärmeleitfähigkeitsprofils war es schlussendlich möglich grundlegende Aussagen über die Bedeutung der Schwanzgruppen-Schwanzgruppen-Grenzfläche für den Wärmetransport durch die Membran zu treffen.

Diese Anwendungsbeispiele der Computersimulation zeigen klar, dass theoretische Berechungen immer dann ein erfolgreicher wissenschaftlicher Ansatz zur Untersuchung des physikalischen Verhaltens von biologischen Systemen darstellen, wenn Messungen nicht detailliert genug oder zu gefährlich sind. Nichtsdestotrotz hat diese Arbeit auch gezeigt, dass obwohl molekulare Computersimulationen heutzutage zu den Standardmethoden zählen, ihre genaue Validierung unerlässlich ist. Während in dieser Arbeit gezeigt wurde, dass der Einfluss von Manostaten auf die RNEMD Resultate für Scherviskositäten nur gering ist, wurde ebenfalls demonstriert, wie unerwartet Berechnungsartefakte zu scheinbar unphysikalischen Resultaten führen können. In diesem Sinne schliesst diese Arbeit mit der Erkenntnis, dass, obwohl Computersimulationen schon seit Jahrzenten etabliert sind, neben den zahllosen resultatbezogenen und auf wissenschaftlichen Problemen beruhenden, thematischen Fragestellungen, auch heute noch viele methodologischer Aspekte der theoretischen Chemie unerforscht sind. Mit den hier präsentierten Resultaten konnte ich in beide Richtungen meinen Teil zur Vergrösserung des wissenschaftlichen Gesamtwissens beitragen.

6. Literaturverzeichnis

[1] O.G. Mouritsen, Life – As a Matter of Fat, Springer, Berlin, 2005

[2] N.A. Campbell, J.B. Reece, Biology, Prentice Hall International, San Francisco, 2008, 8th Edition,

[3] F. Müller-Plathe, YASP: a molecular simulation package, Comput. Phys. Commun. 78 (1993) 77-94

[4] K. Tarmyshov, F. Müller-Plathe, Parallelizing a molecular dynamics algorithm on a multiprocessor workstation using OpenMP, J. Chem. Inf. Model. 45 (2005) 1943-1952

[5] F. Müller-Plathe, A Simple Non-equilibrium Molecular Dynamics Method for Calculating the Thermal Conductivity, J. Chem. Phys. 106 (1997) 6082-6085

[6] M.P. Allen, D.J. Tildesley, Computer Simulation of Liquids, Clarendon Press, Oxford, 1988

[7] D. Bedrov, G.D. Smith, Thermal conductivity of molecular fluids from molecular dynamics simulations: Application of a new imposed-flux method, J. Chem. Phys. 113 (2000) 8080-8084

[8] M. Zhang, E. Lussetti, L.E.S. de Souza, F. Müller-Plathe, Thermal Conductivities of Molecular Liquids by Reverse Non-equilibrium Molecular Dynamics, J. Phys. Chem B 109 (2005) 15060-15067

[9] T. Terao, E. Lussetti, F. Müller-Plathe, Non-equilibrium molecular dynamics methods for computing the thermal conductivity: application to amorphous polymers, Phys. Rev. E 75 (2007) 057701

[10] E. Lussetti, T. Terao, F. Müller-Plathe, Non-equilibrium molecular dynamics calculation of the thermal conductivity of amorphous polyamide-6,6, J. Phys. Chem. B 111 (2007) 11516-11523

[11] E.A. Algaer, M. Alaghemandi, M.C. Böhm, F. Müller-Plathe, Thermal Conductivity of Amorphous Polystyrene in Supercritical Carbon Dioxide Studied by Reverse Nonequilibrium Molecular Dynamics Simulations, J. Chem. Phys. A (2009) DOI: 10.1021/jp9009492

[12] E.A. Algaer, M. Alaghemandi, M.C. Böhm, F. Müller-Plathe, Anisotropy of the Thermal Conductivity of Atreched Amorphous Polystyrene in Supercritical Carbon Dioxide Studied by Reverse Nonequilibrium Nolecular Dynamics Simulations, J. Chem. Phys B (2009) in press

[13] E. Rossinsky, F. Müller-Plathe, Anisotropy of the thermal conductivity in a polymer crystal: Non-equilibrium molecular dynamics simulation of the δ form of syndiotactic polystyrene, The Journal of chemical physics 130 (2009) 134905

[14] M. Alaghemandi, E. Algaer, M. Böhm, F. Müller-Plathe, The thermal conductivity and thermal rectification of carbon nanotubes studied using reverse non-equilibrium molecular dynamics simulations, Nanotechnology 20 (2009) 115704

[15] M. Alaghemandi, E.A. Algaer, F. Leroy, M. Böhm, F. Müller-Plathe, Thermal rectification in mass-graded nanotubes: A model aproach in the framework of reverse non-equilibrium molecular dynamics simulations, submitted to Nanotechnology

[16] F. Müller-Plathe, Reversing the perturbation in non-equilibrium molecular dynamics: An easy way to calculate the shear viscosity of fluids, Phys. Rev. E 59 (1999) 4894-4899

[17] P. Bordat, F. Müller-Plathe, The Shear Viscosity of Molecular Fluids: A Calculation by Reverse Non-Equilibrium Molecular Dynamics, J. Chem. Phys. 116 (2002) 3362-3369

[18] X. Chen, P. Carbone, W.L. Cavalcanti, G. Milano, F. Müller-Plathe , Viscosity and Structural Alteration of a Coarse-grained model of Polystyrene under Steady Shear Flow Studied by Reverse Nonequilibrium Molecular Dynamics, Macromolecules 40 (2007) 8087-8095

[19] W. Zhao, F. Leroy, S. Balasubramanian, F. Müller-Plathe, Shear Viscosity of the Ionic Liquid 1-*n*-Butyl 3-Methylimidazolium Hexafluorophosphate [bmim][PF_6] at 300 K Computed by Reverse Non-equilibrium Molecular Dynamics Simulations, J. Phys. Chem. B 112 (2008) 8129-8133

[20] T.J. Müller, F. Müller-Plathe, Determining the Local Shear Viscosity of a Lipid Bilayer System by Reverse Non-Equilibrium Molecular Dynamics Simulations, ChemPhysChem. 10 (2009) 2305-2315

[21] D. Reith, F. Müller-Plathe, On the Nature of Thermal Diffusion in Binary Lennard-Jones Liquids, J. Chem. Phys. 112 (2000) 2436-2443

[22] P. Bordat, D. Reith, F. Müller-Plathe, The influence of interaction details on the thermal diffusion in binary Lennard-Jones liquids, J. Chem. Phys. 115 (2001) 8978-8982

[23] M. Zhang, F. Müller-Plathe, Reverse non-equilibrium molecular dynamics calculation of the Soret coefficient in liquid benzene/cyclohexane mixtures, J. Chem. Phys. 123 (2005) 124502

[24] P. Polyakov, F. Müller-Plathe, S. Wiegand, Reverse nonequilibrium molecular dynamics calculation of the Soret coefficient in liquid heptane/benzene mixtures, J. Phys. Chem. B 112 (2008) 14999–15004

[25] P. Polyakov, M. Zhang, F. Müller-Plathe, S. Wiegand, Thermal diffusion measurements and simulations of binary mixtures of spherical molecules, J. Chem. Phys 127 (2007) 014502

[26] M. Zhang, F. Müller-Plathe, The Soret effect in dilute polymer solutions: Influence of chain length, chain stiffness and solvent quality, J. Chem. Phys. 125 (2006) 124903

[27] W. L. Cavalcanti, X. Chen, F. Müller-Plathe, Shear Viscosity Calculations through a Reverse Nonequilibrium Method, Phys. Stat. Sol. A 204 (2007) 935-939

[28] T. Terao, F. Müller-Plathe, A nonequilibrium molecular dynamics method for thermal conductivities based on thermal noise, J. Chem. Phys. 122 (2005) 081103(1-3)

[29] T. Terao, F. Müller-Plathe, Comment on: A nonequilibrium molecular dynamics method for thermal conductivities based on thermal noise, J. Chem. Phys. 123 (2005) 217101

[30] T.J. Müller, M. Al-Samman, F. Müller-Plathe, The influence of thermostats and manostats on reverse non-equilibrium molecular dynamics calculations of fluid viscosities, J. Chem. Phys. 129 (2008) 014102

[31] H. Eslami, F. Müller-Plahte, The Viscosity of Nanoconfined Polyamide-6,6 Oligomers: Atomistic Reverse Nonequilibrium Molecular Dynamics Simulation, J. Phys. Chem. B (submitted)

[32] J. Borak, F.R. Sidell, Agents of chemical warfare: sulfur mustard, Ann. Emerg. Med. 21 (1992) 303-308

[33] S. Singer, G.L. Nicholson, The fluid mosaic model of the structure of cell membranes, Science 175 (1972) 720-731

[34] E. Evans, V. Heinrich, Dynamic strength of fluid membranes, C. R. Phys. 4 (2003) 265-274

[35] E. Evans, A. Yeung, Hidden dynamics in rapid changes ofbilayer shape, Chem. Phys. Lipids 73 (1994) 39-56

[36] R.M. Raphael, R.E. Waugh, Accelerated interleaflet transport of phosphatidylcholine molecules in membranes under deformation, Biophys. J. 71 (1996) 1374-1388

[37] Y.A. Chizmadzhev, D.A. Kumenko, P.I. Kuzmin, L.V. Chernomordik, J. Zimmerberg. F. Cohen, Lipid flow through fusion pores connecting membranes of different tensions, Biophys. J. 76 (1999) 2951-2965

[38] S.A. Shkulipa, W.K. den Otter, W.J. Briels, Surface Viscosity, Diffusion, and Intermonolayer Friction: Simulating Sheared Amphiphilic Bilayers, Biophys. J. 89 (2005) 823-829

[39] W.K. den Otter, S.A. Shkulipa, Intermonolayer Fricition and Surface Shear Viscosity of Lipid Bilayer Membranes, Biophys. J. 93 (2007) 423-433

[40] F. Müller-Plathe, P. Bordat, Reverse Non-equilibrium Molecular Dynamics, Lect. Notes Phys. 640 (2004) 310-326

[41] R. Faller, H. Schmitz, O. Biermann, F. Müller-Plathe, Automatic Parameterization of Force Fields for Liquids by Simplex Optimization,J. Comp. Chem. 20 (1999) 1009-1017

[42] M. Hülsmann, T. Köddermann, J. Vrabec, D. Reith, GROW: A Gradient-based Optimization Workflow for the Automated Development of Molecular Models, submitted

[43] M. Hülsmann, J. Vrabec, A. Maaß, D. Reith, Assessment of Numerical Optimization Algorithms for the Development of New Molecular Models, submitted

7. Anhang

7.1. Kraftfeldoptimierung mittels der Simplex Methode

Neben den direkt mit meiner Forschung verknüpften Arbeiten verfolgte ich während meiner Dissertationszeit auch weitere Projekte. Auch wenn eine Anwendung der in diesem Anhang vorgestellten Arbeiten auf meine eigentliche Forschung aufgrund von mangelndem experimentellen Daten nicht möglich war, so werden sie hier aufgeführt, weil sie in den vorherigen Arbeiten referenziert wurden.

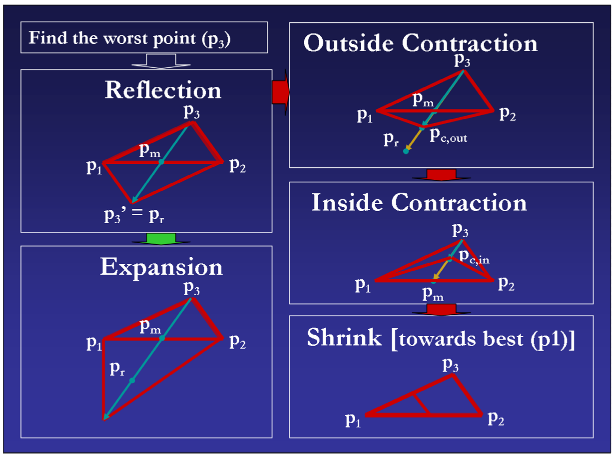

Abb. 6: Diagramm der Optimierungsschritte der Simplexmethode für ein zweidimensionales Problem.

Wie jedes physikalische Modell sind auch Molekular-Dynamik-Simulationen nur so gut, wie die zur Modellierung verwendeten Parameter. Dies trifft nicht nur generell für die den Berechnungen zugrunde liegenden Potentialfunktionen, sondern insbesondere auch für die Parametrisierung der Kraftfeldkonstanten zu. Auch wenn einige davon aus experimentellen Messungen (z.B. Federkonstanten für Bindungs- und Winkelschwingungen aus der Infrarotspektroskopie) oder auch quantenchemischen Rechnungen abgeleitet werden können, so ist eine Abweichung der berechneten physikalischen Größen von den experimentell bestimmten trotzdem möglich, da die Rechnungen an vielen Stellen unphysikalische Näherungen und Rundungen enthalten. So werden Ladungen beispielsweise generell als Punktladungen gerechnet, wobei die Physik eine Elektronendichteverteilung verlangen würde. Ebenso werden eigentlich dynamische Bindungen, die schwingen und auch brechen können, oftmals starr auf die mittlere Bindungslänge beschränkt. Um solche und ähnliche Einflüsse im Modell abzufangen, können die Parameter des Systems leicht abgewandelt werden, so dass die resultierenden physikalischen Größen wieder mit den gemessen Werten übereinstimmen. Solche Anpassungen folgen zwar gewissen Trends: Lennard-Jones Sigma Parameter beeinflussen den mittleren Abstand nichtgebundener Teilchen und damit maßgeblich die Dichte, Lennard-Jones Epsilon Parameter beeinflussen die Potentialtiefe und damit hauptsächlich die Verdampfungsenthalpie eines Systems. Im Endeffekt tragen aber alle Simulationsparameter in unterschiedlichem Maße zu allen Messgrössen bei. Ihr komplexes, vieldimensionales Zusammenspiel zur akkuraten Beschreibung eines Systems ist absolut nicht trivial und lässt sich nicht analytisch lösen.

In diesem Falle bieten Optimierungstechniken einen adäquaten Lösungsansatz. Im Rahmen der Industrial Fluid Properties Simulation Collective (IFPSC) Challenge entstand in Zusammenarbeit mit dem Fraunhofer-Institut für Algorithmen und wissenschaftliches Rechnen auf den Grundlagen von Roland Faller et al. [41] die vorliegende Arbeit, welche in Fluid Phase Equilibria 274 (2008) 27-35 veröffentlicht wurde. Die hier gewonnenen Erkenntnisse wurden von M. Hülsmann [42, 43] aufgegriffen, der mittels anderer Optimierungsmethoden (Steepest Descent) eine effizientere Optimierung von Kraftfeldparametern anstrebt.

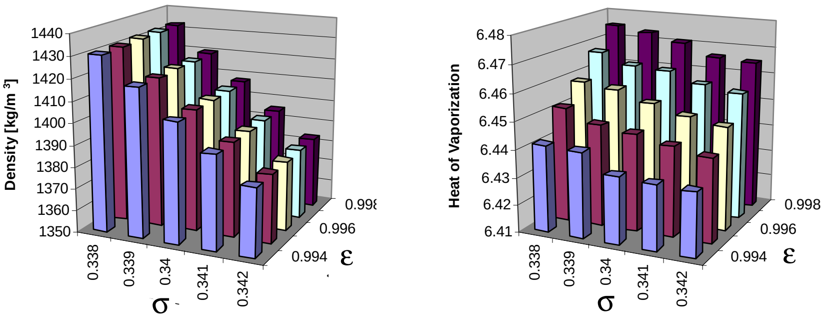

Abb. 7: Zusammenspiel von Lennard-Jones Sigma und Espilon in Berechungen von Ethylenoxid

Economic simplex optimization for broad range property prediction: Strengths and weaknesses of an automated approach for tailoring of parameters

Thomas J. Müller[a,1], Sudip Roy[a,1], Wei Zhao[a,1], Astrid Maaß[b,*,1], Dirk Reith[b]

[a] *Eduard-Zintl-Institut für Anorganische und Physikalische Chemie, Technische Universität Darmstadt, Petersenstr. 20, 64287 Darmstadt, Germany*
[b] *Fraunhofer Institute for Scientific Computing and Algorithms, Schloss Birlinghoven, 53754 Sankt Augustin, Germany*

ARTICLE INFO

Article history:
Received 31 January 2008
Received in revised form 18 May 2008
Accepted 18 June 2008
Available online 27 June 2008

Keywords:
Physical property prediction
Molecular dynamics
Simplex optimization
YASP
Monte Carlo

ABSTRACT

The need for predicting physical compound properties supplementing experimental data is considerable. Nowadays a wide range of classical simulation techniques is available for computing a multitude of such properties with acceptable effort. We here give a field report about our approach, which was to fit an initial model to a single point in the phase diagram. By way of accessing commonly available experimental values we developed a compound-specific force field via simplex optimization. For predicting the desired properties of the novel model we did engage classical equilibrium as well as reverse non-equilibrium molecular dynamics in combination with Monte Carlo methods and report here the performance of these methods in detail for the example compound ethylene oxide. We find that the new model describes the experimentally observed behavior of the test compound ethylene oxide (EO) very well in the molecular dynamics section. However, when applying the simplex optimized model to the Monte Carlo section, the limits of transferability become apparent.

1. Introduction

Highly reactive compounds are frequently involved in industrial processes. While reactivity is a desirable feature, it requires extremely careful handling and thus prohibits experiments that are dispensable at any means. Still, in daily practice the need for property data is pressing. Simulation data are useful to fill this gap. This was the motivation of the Industrial Fluid Properties Simulation Collective (IFPSC) for announcing the 4th challenge, when the ethylene oxide (EO) molecule was chosen as a relevant example compound for testing the transferability of methods and force fields to predict a wide range of properties [1].

When participating in this challenge, our main objective was to probe the capability of our simplex optimization procedure for deriving such individually tailored compound models by fitting them to very few basic experimental parameters. According to the contest rules, the results for the created models are compared to those obtained for a previously described reference model [2].

Atomistic soft matter simulations are most commonly used for investigating system properties that depend on intermolecular interactions for which the required large system size prohibits quantum mechanical methods [3]. Simplifying assumptions have to be made that lead to a limited number of analytic terms in order to construct a force field [4]. Compound-specific behavior is incorporated by the individual choice of the force-field parameters for each atom instead of considering the electronic structure. A variety of very general force-field parameters (AMBER [5], CHARMM [6], GROMOS [7], OPLS [8], UFF [9], others) that describe the behavior of a wide range of compounds globally quite well exists, but these force fields may lack the required accuracy for a specific compound [10]. Individual parameter sets created by quantum mechanical methods generally describe very well the intramolecular properties, but may not sufficiently reproduce intermolecular properties due to the inherent limitation of the underlying models [11].

Therefore, our approach to develop an all-atom force-field model of EO that allows extensive simulation studies is to follow a generic, most simple route: starting from the ab initio level and adjusting the model to very few, commonly accessible experimental data.

Thus, as the chosen optimization procedure is quite consumptive, the model is being calibrated with respect to only one point in the phase diagram, i.e. to the requested temperature of 375 K and the associated experimental value for the pressure. The properties we address comprise the densities, heat capacities, isothermal compressibilities, viscosities and thermal conductivities for both the saturated liquid phase and the vapor phase at 375 K, as well as

---

* Corresponding author. Tel.: +49 2241 142481; fax: +49 2241 142181.
E-mail address: astrid.maass@scai.fraunhofer.de (A. Maaß).
[1] All these authors contributed equally to this work.

information about the vapor pressure, the heat of vaporization, and critical properties. As we aim at predicting such a wide spectrum of diverse properties, especially including transport behavior, we opt for an all-atom model that provides the maximum number of internal degrees of freedom, in order to capture friction and exchange of thermal energy comprehensively.

2. Methods and computational details

The requested types of properties range from phase equilibria to caloric and dynamic properties. Especially for the latter, the simulation technique of choice is molecular dynamics (MD) simulation. For all MD simulations the program package YASP [12] was utilized. Transport properties were determined using reverse non-equilibrium molecular dynamics (RNEMD) [13], a comparatively fast converging method, likewise implemented in YASP. When needed, supplementary Monte Carlo simulations were performed with the MCCCS (Monte Carlo for Complex Chemical Systems) Towhee simulation program, version 5.2.1 [14].

Presuming a reasonable molecular geometry, the diverse physical properties mainly depend on the non-bonded interactions between the particles, which are modeled by Lennard–Jones (LJ) and electrostatic interactions in the classical approach. Thus, the LJ parameters (distance of zero-potential σ and potential-well-depth ε) are subject to modification, whereas the atomic charges were kept fixed.

In order to keep not only the computational demand low, but also the optimization problem feasible, we decided to restrict the model to only two atom types involved in LJ-interactions. Considering the numerical proportion of hydrogen to carbon (being 2:1), we neglected the hydrogen atoms consequently, thereby also maintaining comparability to the reference model.

2.1. *Models*

For starting the optimization procedure, an initial all-atom model representing ethylene oxide was created with Gaussian 03 [15] using a 6-31G (d) basis set for Hartree-Fock calculations in order to provide a suitable set of atomic charges and appropriate bond and angle geometries. Two sets of charge models were derived from the electrostatic potential (ESP) and fit to the ESP at points selected according to the CHelp [16] and CHelpG [17] schemes. The second charge model emphasizes the negative character of the oxygen atom compared to that of the carbon atoms more, however the overall charge distribution among the three atom types of EO is quite alike for both models. Finally, we used as partial charges the average atomic charges of both models. As EO is almost rigid due to its three-membered ring structure, throughout all simulations the bond lengths were kept fixed and only angles involving H-atoms were treated as flexible, the force constants being derived from the calculated vibrational spectrum. The LJ-parameters of oxygen and carbon are subject to variation during the optimization.

The reference or round robin model (RR) is labeled as model *A* by Wielopolski and Smith [2] and treats the methylene groups as united atoms. All employed modeling techniques create the LJ-parameters for mixed interactions according to the rules of Lorentz and Berthelot [18,19]. As implemented in YASP, we apply a reaction field to cope with long range Coulombic forces, whereas Towhee utilizes Ewald summation.

2.2. *Simplex optimization*

The chosen set of parameters is optimized according to an iterative algorithm, i.e. cycles of MD simulation, evaluation of target properties, and eventually readjustment of parameters according to the downhill simplex method are performed repeatedly until the abort condition is reached [20], which was the relative quadratic error $((\rho-\rho^{\text{target}})/\rho^{\text{target}})^2+((\Delta H_{\text{vap}}-\Delta H_{\text{vap}}^{\text{target}})/\Delta H_{\text{vap}}^{\text{target}})^2)$ to fall below the chosen threshold.

The readjustment of parameters is achieved by reflection, expansion or contraction in parameter space [21]. This optimization method is robust and applicable even if an analytical functional form is not available, as is the case here.

The choice of parameters to optimize was based on two considerations. The number of optimization iterations to find a minimum increases exponentially with the number of parameters to optimize in one go. Therefore, we were limited to only few parameters. Test simulations (not shown here) with up to 6 parameters in one optimization have been performed. We decided to keep the values from the quantum calculations fixed and to concentrate on the optimization of other parameters. Besides this technical consideration, we intended to start with a model for EO comparable to the RR model and to refine it stepwise to a new model. Thus, we started experimentally by optimizing σ- and ϵ-values independently and finally went on with the here reported procedure of optimizing σ and ϵ at the same time. When trying to incorporate the optimization of charges the algorithm changed the charges significantly outside of their expected range of values (even inverting the polarity), without improving the overall performance of the force field with respect to the goals of the challenge. Therefore we report here the results of the optimization of the LJ-parameters for the carbon and oxygen atoms.

For starting the simplex optimization procedure, initial values for the variables have to be provided manually. The values chosen should cover quite a large (but still reasonable) region in parameter space in order to avoid the results being confined in a local minimum all over the time. As the four-dimensional parameter space needs five starting points for the simplex algorithm, we considered quadruples of values which cover the following spans: $\sigma_{\text{CC}} = 0.3\text{–}0.4\,\text{nm}$, $\sigma_{\text{OO}} = 0.26\text{–}0.31\,\text{nm}$, $\varepsilon_{\text{CC}} = 70\text{–}95\,\text{K}$, $\varepsilon_{\text{OO}} = 60\text{–}80\,\text{K}$.

Table 1 summarizes all the details of the final models that are used for property prediction. The optimized model differs from the reference model mainly in the presence of hydrogen atoms, i.e. in the distribution of charges, as the LJ parameters for H-atoms are set to zero. Besides that the actual values of σ and ε differ.

Table 1
Summary of models

	RR	EO_{opt}
Lennard–Jones parameters		
σ_{OO} [nm]	0.2666	0.26308
ε_{OO} [K]	73	55.47
ε_{OO} [kJ/mol]	0.60695	0.46119
σ_{CC} [nm]	0.37143	0.38372
ε_{CC} [K]	90	74.82
ε_{CC} [kJ/mol]	0.7438	0.62209
Atomic charges		
q_{O}	−0.3216	−0.312
q_{C}	0.1608	−0.084
q_{H}	–	0.120
Bond lengths (fixed)		
r_{CO} [nm]	0.1431	0.1401
r_{CC} [nm]	0.1466	0.1453
r_{CH} [nm]	–	0.1077
Bond angles + force constants		
α(HCH)[degree], k_α [kJ/mol rad^2]	–	115.23, 276.33
α(CCH)[degree], k_α [kJ/mol rad^2]	–	119.88, 314.01
α(OCH)[degree], k_α [kJ/mol rad^2]	–	115.24, 293.08

2.3. System setup and simulation conditions

2.3.1. Molecular dynamics

In general, uniform settings were used throughout all simulations in order to ensure utmost consistency. However, as the system size affects computation time, even more drastically when repeated iteratively, previous to the optimization process the finite size effect on the density was studied by running liquid phase MD simulations of cubes with 256, 512 and 1024 molecules (data not shown). As a consequence 256 molecules per box were considered sufficient for the equilibrium MD runs of the optimization procedure. Due to different requirements concerning system geometries for other settings (Gibbs-Ensemble Monte Carlo (GEMC), NEMD), system sizes of 512 or 768 molecules were used for computing the heat capacities, transport properties or vapor–liquid-coexistence curves, respectively. The computational details for all simulations comprised a non-bonded cut-off of 0.9 nm and a neighbor list cut-off of 1.0 nm in case of the liquid phase systems and a non-bonded cut-off of 5.0 nm in case of the vapor phase systems with a neighbor list cut-off of 5.1 nm. The neighbor list was updated every 10 time steps, the reaction-field-dielectric was 14.5 in both cases. The temperature was coupled to 375 K using a Berendsen thermostat with a coupling constant of 0.2 ps while the pressure was coupled to 1428.5 kPa using a Berendsen manostat with a coupling time of 2 ps and a compressibility of 1×10^{-6} 1/kPa. The center-of-mass drift of the systems was removed every 1000 time steps. The frequency of snapshot collection and the instantly calculated properties was every 200 time steps. The time step size was 2 fs throughout.

The simplex algorithm implemented in YASP as published by Faller et al. [20] has been applied to optimize the parameter set. In each optimization cycle at least three different simulations have been carried out:

(1) A pre-equilibration of the starting configuration (which is the output coordinate file of the previous simplex steps with most similar parameter sets; or a standard equilibrated one if none is available) has been performed for 100 000 time steps.
(2) The system was considered sufficiently equilibrated, as soon as there was no significant drift detectable in the pressure of the system, i.e. a linear regression was performed on the recorded pressure values. The product of the slope of the regression line times the total number of datapoints needed to fall below the standard deviation of datapoints. Thus, the final equilibration of the system was achieved by repeating simulation cycles of 100 000 time steps each until the equilibration criterion was met.
(3) Starting with the equilibrated system the finally evaluated production run was performed for another 100 000 time steps.

After this sequence of simulations the simplex algorithm calculated the performance of the current parameter set by comparing the obtained density ρ to the target liquid density ρ^{target} of 747 kg/m^3 and the obtained heat of vaporization ΔH_{vap} to a target heat of vaporization $\Delta H_{\mathrm{vap}}^{\mathrm{target}}$ of 19.8 kJ/mol. The target values were derived from the data given in the ethylene oxide user-guide [22] and in Walters and Smith [23] and were chosen such that the final model is optimized at the chosen thermodynamic system settings, i.e. 375 K and 1428.5 kPa. With the resulting performance value, the simplex steps were executed, i.e. a new set of parameters was generated and finally a new cycle was started. This procedure was repeated until the performance fell below the threshold of 0.0001 in order to ensure convergence.

For setting up systems under saturated phase conditions, NpT simulations were conducted. We estimated the saturated vapor pressure by use of the definition of the acentric factor as given in [24]: $\log\,[P_{\mathrm{r}}^{\mathrm{sat}}]_{T_{\mathrm{r}}=0.7} = -(\omega + 1)$ with $P_{\mathrm{r}}^{\mathrm{sat}}$ being the reduced saturation pressure, T_{r} being the reduced temperature and ω the acentric factor. Applying the experimentally known data ($p_{\mathrm{crit}} = 7190$ kPa, $T_{\mathrm{crit}} = 469$ K and $\omega = 0.2114$ [22]) leads to a theoretical vapor phase saturation pressure of 10% below the experimental value at 328 K. This was transferred to 375 K yielding 1248.5 kPa as reference pressure for vapor phase simulations. Likewise the pressure was increased by 10% to 1571.4 kPa for the liquid phase simulations in order to ensure stable phase separation. As the compressibility of a liquid is usually very small, such a moderate increase in pressure should not significantly affect the final results.

For computing the transport properties, for all systems (both in liquid and in vapor phase) a $L \times L \times 3L$ box containing 768 EO molecules was built by replicating an equilibrated cubic box containing 256 molecules three times in z-direction. For both the RR model and the optimized model, RNEMD simulations were performed for the liquid phase at exchange periods of every 60, 200, 400, 800, and 1200 steps for calculating the shear viscosity and at exchange periods of every 100, 200, 400, 800, and 1200 steps for calculating the thermal conductivity. In the vapor phase, exchange periods of every 2, 5, 20, 40, 80, and 120 steps were applied for calculating the shear viscosity. Swap periods of 100, 200, 400, 800, 1200 steps, respectively, were employed for determining the thermal conductivity. In both cases, molecular velocity exchange has been done. All simulations were done for 9 ns and the last 8 ns were used for data analysis.

2.3.2. Monte Carlo

The Gibbs-Ensemble Monte Carlo method was utilized as described in Panagiotopoulos [26] and Martin [10] for recording vapor–liquid-coexistence curves. Therefore, 256 + 512 EO molecules of the respective model were distributed among two cubic boxes (for the vapor and the liquid phase), both with periodic boundary conditions. Initial configurations were generated by multiplying a single molecule and placing the copies on a simple cubic lattice to yield cubic boxes. The respective box lengths were chosen such that the corresponding experimental density was obtained and after subsequent equilibration the phase separation was maintained. In contrast to the reaction field method implemented in YASP, the MC program Towhee [14] utilizes Ewald summation, and for LJ-interactions a non-bonded cut-off distance of 1.0 nm and analytical tail correction. Although this is not fully consistent with the conditions used throughout the MD simulations and especially during the optimization, lacking exactly matching methods this proceeding was accepted.

For the rigid RR model only volume moves ($p = 0.002$), rotational bias two-box molecule transfer moves ($p = 0.001$) and center-of-mass translational as well as rotational moves ($p = 0.7$ each) were considered. Vapor–liquid-coexistence data were recorded for temperatures ranging from 230 to 375 K. The systems were equilibrated for 50 000 Monte Carlo cycles, where a cycle consisted of 768 moves. Additional runs of 50 000 cycles were executed and evaluated by splitting the simulation into 20 parts for estimating the uncertainties.

3. Calculation

The list of requested properties given in the challenge announcement is divided into three categories. Out of these we intend to determine the liquid and vapor phase densities, the heat of vaporization, the vapor pressure and the critical temperature and critical density, the heat capacity at constant pressure for both phases and the associated isothermal compressibilities, as well as the corresponding liquid state and gas state viscosities and thermal conductivities. The utilized techniques are specified below.

3.1. Category 1 properties

The current or finally the average density is a standard output value. According to Eq. (1) the density ρ of the simulated system is derived from the volume V of the cubic simulation box with box length l (therefore $V = l^3$) and the total mass in the system m_{sys} which is equal to the n (the number of molecules in the box) divided by the Avogadro constant A times the molecular weight of one ethylene oxide molecule $m_{\text{EO}} = 44.05\,\text{g/mol}$.

$$\rho = \frac{m_{\text{sys}}}{V} = \frac{n m_{\text{EO}}}{A l^3} \tag{1}$$

The heat of vaporization ΔH_{vap} is derived from the total non-bonded energy E_{nb}, the temperature T, the gas constant R, and the number of molecules n according to Eq. (2).

$$\Delta H_{\text{vap}} = -\frac{E_{\text{nb}}}{n} + RT \tag{2}$$

In order to derive the critical properties (temperature T_{crit} and density ρ_{crit}), the resulting liquid and vapor phase densities were fitted to the law of rectilinear diameters (Eq. (3)) and the law of order parameter scaling (Eq. (4)), where the critical exponent β_{crit} was taken as 0.313 [27]:

$$\frac{\rho_{\text{liq}} + \rho_{\text{vap}}}{2} = \rho_{\text{crit}} + C_1(T - T_{\text{crit}}) \tag{3}$$

$$\frac{\rho_{\text{liq}} - \rho_{\text{vap}}}{2} = C_2(T - T_{\text{crit}})^{\beta_{\text{crit}}} \tag{4}$$

From the latter production runs the resulting thermodynamic pressure of the gaseous box was taken as vapor pressure of the respective model at a given temperature.

3.2. Category 2 properties

The molar heat capacity at constant pressure C_p for the saturated liquid phase and for the vapor phase, respectively, has been calculated with five production runs at different temperatures (365, 370, 375, 380 and 385 K), but otherwise identical simulation conditions (see above). The total energy $\langle E_{\text{tot}} \rangle$ and volume $\langle V \rangle$ were averaged over time. The pressure used in the following formula is the target value of the manostat ($p = 1571.4\,\text{kPa}$ for liquid phase and $p = 1248.5\,\text{kPA}$ for vapor phase). A linear fit of the plot ($\langle E_{\text{tot}} \rangle + P\langle V \rangle$) versus T has been used to calculate C_p.

$$C_p = \frac{1}{n_{\text{mol}}} \left[\frac{\partial(\langle E_{\text{tot}} \rangle + p\langle V \rangle)}{\partial T} \right]_{p=1571.4\,\text{kPa}} \tag{5}$$

The isothermal compressibility β is a measure of the relative volume change depending on the pressure P at constant temperature:

$$\beta = -\frac{1}{V}\left(\frac{\partial V}{\partial P}\right)_T \tag{6}$$

This equation can be expressed in terms of density (ρ) as follows:

$$\beta = \left(\frac{\partial \ln(\rho)}{\partial P}\right)_T \tag{7}$$

As the density of a system is a function of the pressure, the slope of the graph when plotting $\ln(\rho)$ against P gives the isothermal compressibility β. In our case, the temperature was fixed to 375 K and simulations were conducted at 10 000, 20 000, 30 000 and 40 000 kPa for the liquid phase and 200, 500, 800 and 1000 for the vapor phase, respectively.

3.3. Category 3 properties

For computing the transport properties we apply RNEMD [13] where a steady gradient is established artificially. According to the linear-response theory, the shear viscosity η is the proportionality constant between a shear field and a flux of transverse linear momentum:

$$j_z(P_x) = -\eta \frac{\partial v_x}{\partial z} \tag{8}$$

The shear field, also called the shear rate, is defined as the gradient $\partial v_x/\partial z$: we have chosen the x-component of the fluid velocity relative to the z-direction. The momentum flux $j_z(p_x)$ is the x-component of the momentum p_x, which is transported in the z-direction during a given time. In order to calculate the shear viscosity, unphysical momentum transfer needs to be performed within the simulation box.

(1) The simulation box is divided into N (even) slabs labeled from 1 to N. Slab 1 is supposed to have a positive x-component for the momentum and the slab in the center of the box (slab $M = N/2 + 1$) has a negative x-component of the momentum.
(2) To achieve the first point, we look for the molecule in slab 1 with the largest negative x-component of the momentum in slab 1 and for the molecule with the largest positive x-component of the momentum in slab M.
(3) We exchange the x-component of the center-of-mass momentum p of the chosen molecules with each other. Since we only have one type of molecules, the mass of the chosen molecules is always the same. Therefore, we can exchange center-of-mass velocities instead. Simultaneously in both chosen molecules, the x-component of the center-of-mass velocity $V_x = (p_x/\sum_{i=1}^{n} m_i)$ is subtracted from the x-velocity component of every atom in the chosen molecule and added to the atoms in the other molecule.

If we repeat this procedure periodically, after a simulation time t, the total exchanged momentum is $P_{\text{tot}} = \sum_{\text{exch}}(p_{x,M} - p_{x,1})$ and the momentum flux is

$$j_z(P_x) = \frac{P_{\text{tot}}}{2tL_xL_y}, \tag{9}$$

where $p_{x,1}$ and $p_{x,M}$ are the two x-components of the exchanged momentum in the slabs 1 and M, respectively, and L_x and L_y are the lengths of the orthorhombic simulation box in the x- and y-directions. When the system has converged towards a steady state, we can measure the mean velocity in x-direction in each slab, determine $\partial v_x/\partial z$, and calculate the value of the shear viscosity using Eq. (8).

In our calculation, the strength of the shear field is controlled by the swap period W with which momentum swaps are executed; a larger value of W meaning a weaker shear field.

In analogy, the thermal conductivity λ relates a heat flux j_z to a temperature gradient $\mathrm{d}T/\mathrm{d}z$:

$$j_z = -\lambda\left(\frac{\mathrm{d}T}{\mathrm{d}z}\right) \tag{10}$$

In order to build up a steady temperature gradient induced by continuous heat flux, unphysical heat transfer needs to be performed within the simulation box. Similarly, the method contains three steps.

(1) The simulation box is divided into N (even) slabs labeled from 1 to N. Slab 1, at the beginning of the simulation box, is designated

as the hot slab, and slab M, at the center of the simulation box, is designated as the cold slab.

(2) The molecule in slab M with the largest modulus of its velocity vector and the molecule in slab 1 with the smallest modulus of its velocity vector are identified.

(3) The center-of-mass momenta of these two selected molecules are exchanged. This mimics the process of taking heat from slab M to slab 1 in an unphysical way.

Since the energy is conserved, it flows back through the system through a physical transport mechanism which results in a heat flux. After a long enough simulation time a steady temperature gradient will be established.

The heat flux through the system can be deduced from the unphysical heat exchange during the exchange steps.

$$j_z = \frac{1}{2tL_xL_y} \sum \frac{m}{2}(v^2_{\text{hot}} - v^2_{\text{cold}}) \qquad (11)$$

This allows to calculate the thermal conductivity according to Eq. (10). Again, the strength of the thermal field is controlled by the swap period W.

4. Results

4.1. Performance of models

With the chosen initial points in parameter space, the simplex algorithm yields the model EO_{opt} as summarized in Table 1. For the novel model as well as the reference RR model the physical properties have been determined. The final results are presented in Tables 2 and 3 and compared to experimental reference data.

4.1.1. Category 1 properties

We find that the liquid phase density of the RR model in the chosen range of temperatures is about 5–7% lower than the respective reference density, whereas the vapor phase densities are quite within the expected range. Correspondingly, the vapor pressure at 375 K of 1.468 MPa agrees well with the experimentally observed value of 1.437 MPa. The computed critical temperature of 467.1 K reproduces almost perfectly the reference value of 469.15 K, whereas the critical density ranges approximately 3% below the measured value, which is consistent which the general trend of too low densities. Consequently, also the heat of vaporization at 375 K is underestimated by approximately 5%.

For liquid densities of the optimized model we observe the same, but even more pronounced trend as for the RR model; accordingly the optimized model yields a critical density that is about 8% lower than the reference. The associated critical temperature of 448.7 K is approximately 20 K below the experimental value. In contrast, the gas phase densities tend to be higher than measured [22] and consequently the thermodynamic pressure exceeds the reference value by 15%.

The remaining physical properties were obtained by MD simulations. For the RR model the liquid density value at 375 K of 701.3 kg/m^3 matches nicely the value of 702.2 kg/m^3 that results from the Monte Carlo simulations, indicating a good consistency of results obtained by different simulation techniques under liquid phase conditions. For the vapor phase the density obtained by MD is 15% lower than that achieved in GEMC simulation or by experimental measurements, which is due to the reference pressure that was used for the manostat. This reference pressure was set to 1.248 MPa (instead of 1.468 MPa that were obtained by GEMC).

Concerning the optimized model and in contrast to the previous one, the values for the liquid density as well as for the heat of vaporization match perfectly the experimental values, as these numbers were used as target values during the optimization procedure. The vapor phase density however, is by roughly 50% much too low, compared to the experimental reference, which traces back to the same reason as above.

4.1.2. Category 2 properties

For the RR model, the heat of vaporization is 15% below the reference. The same applies for the specific heat capacity, which is consistently too low for the liquid, as well as for the vapor phase systems and thus does not resemble the experimental data. The obtained values for the isothermal compressibility are well reproduced in case of the liquid phase (14% below reference value), but almost twice as large in case of the vapor phase simulations.

The optimized model performs better in terms of heat of vaporization obviously, and heat capacity: the molar heat capacity for the liquid C_p is 37% higher than compared to experiment, but the vapor phase heat capacity is only 7% off; the recorded data are presented in Figs. 1 and 2. In terms of isothermal compressibility however, the results consistently exceed by approximately a factor of two the expected values.

4.1.3. Category 3 properties

Shear viscosity and thermal conductivity were studied using RNEMD simulations. Compatible to the observed low density, the liquid phase of the RR model displays a too low viscosity as well, whereas the vapor phase matches nicely the experimental value. The values for the thermal conductivity, in contrast are quite close to the reference values, where the one for the liquid phase was not measured, but calculated as well.

For the optimized model, the results are presented in more detail.

Fig. 3 shows the velocity profiles of all systems in liquid phase at different shear rates. Linear behavior was observed for the selected swap periods. We then calculate the shear viscosities at these shear

Table 2
Vapor–liquid-coexistence data and related properties for both models obtained by GEMC

Density [kg/m^3]	RR		EO_{opt}		Experiment [22]	
	Liquid	Vapor	Liquid	Vapor	Liquid	Vapor
230 K	910.6	0.257	870.3	0.287	955	0.253
260 K	875.1	0.747	829.4	0.869	918	0.738
290 K	835.6	2.531	788.4	2.976	878	2.50
330 K	778.2	8.307	724.1	9.71	820	8.29
375 K	702.2	23.897	644.1	28.09	744	24.1
400 K	650.1	37.247	592.7	44.43	694	–
T_{crit}	467.1		448.7		469.15	
ρ_{crit}	301.83		285.4		311	
$p^{375\text{K}}_{\text{vapor}}$ [MPa]	1.468 ± 0.0032		1.649 ± 0.0169		1.437	

Table 3
Physical properties obtained by MD at a simulation temperature of 375 K

	RR		EO_{opt}		Experiment [22,23]	
	Liquid	Vapor	Liquid	Vapor	Liquid	Vapor
Category 1 properties						
Density [kg/m^3]	701.3	19.8	749.8	11.0	746.7	24.6
ΔH_{vap} [kJ/mol]	17.00		19.87		19.8	
Category 2 properties						
C_p [J/g K]	0.79	0.86	3.16	1.79	2.30	1.67
β [1/10^{-6} kPa]	2.23	1591	5.23	1800	2.6	819
Category 3 properties						
Viscosity [mPa s]	0.081±0.002	0.010±0.003	0.171±0.003	0.0160±0.0004	0.151	0.012
Thermal conductivity [W/(mK)]	0.095±0.002	0.0125±0.0001	0.439±0.003	0.031±0.001	0.12 [30]	0.02

For computing the heat capacity, additional runs at 365, 370, 380 and 385 K were performed. For the liquid phase simulations the reference pressure was set to 1571.4 kPa, in case of vapor phase simulations to 1248.5 kPa.

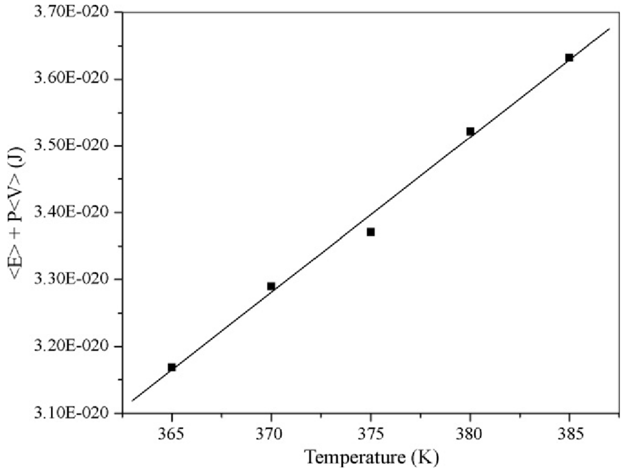

Fig. 1. From the temperature dependence of $\langle E_{tot}\rangle + P\langle V\rangle$ the molar heat capacities were derived for the optimized model in liquid phase.

rates and the results are shown in Fig. 4. The shear viscosities range from 0.164 to 0.171 mPa s, displaying almost a constant level, which is indicative for an appropriate magnitude of perturbation and a good signal-to-noise ratio. Therefore the value of 0.171 mPa s was taken as result and is in agreement with the experimental observation of 0.15 mPa s. The shear viscosity of the vapor phase was found to be 0.0160 mPa s which also compares well to 0.012 mPa s obtained experimentally.

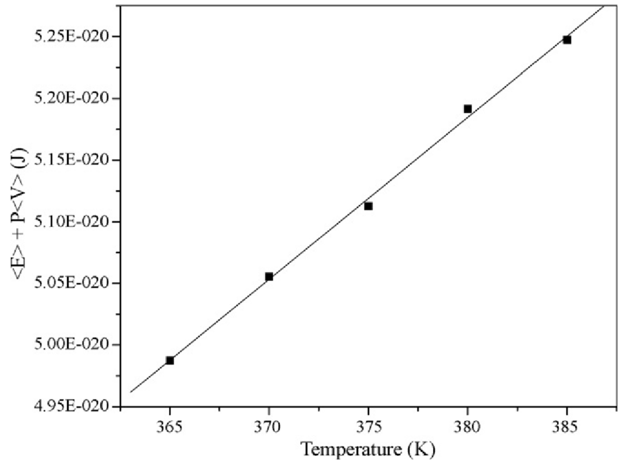

Fig. 2. From the temperature dependence of $\langle E_{tot}\rangle + P\langle V\rangle$ the molar heat capacities were derived for the optimized model in vapor phase.

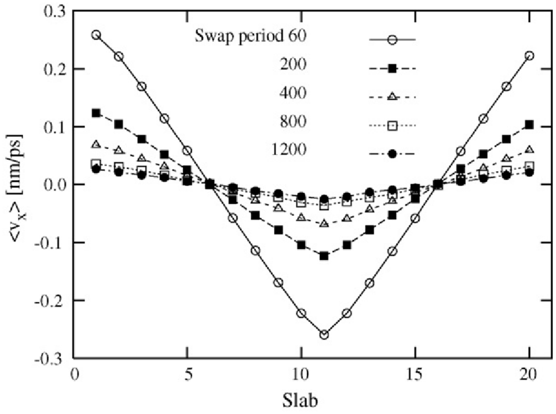

Fig. 3. Velocity profiles relative to the slabs of the simulation box for different swap periods as recorded for the optimized model in the saturated liquid phase.

The calculation of the thermal conductivity is in the same spirit as the calculation of shear viscosity. In Fig. 5, the temperature profiles of all systems are shown. Linear behavior was found for all perturbation rates tested for the liquid system. The obtained results range from 0.335 to 0.439 W/(mK), which is considerably higher than the computational reference of 0.12 W/(mK), estimated by the Missenard method [30]. This is suggested to be a general feature of all-atom models which have more degrees of freedom for transferring kinetic energy than united-atom models such as the RR model

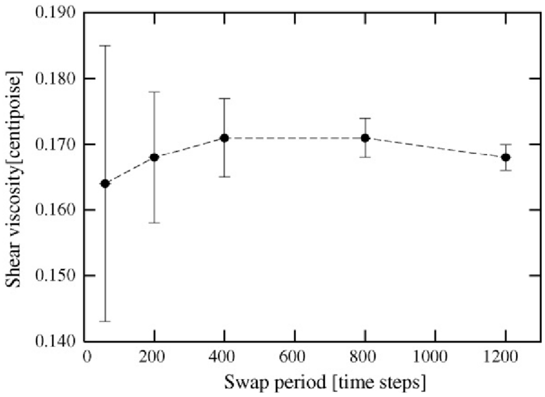

Fig. 4. Viscosity in dependence of exchange period.

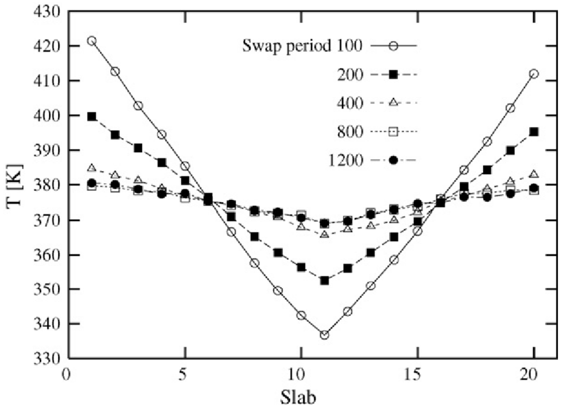

Fig. 5. Temperature profiles relative to the slabs of the simulation box for different swap periods for the optimized model in saturated liquid phase.

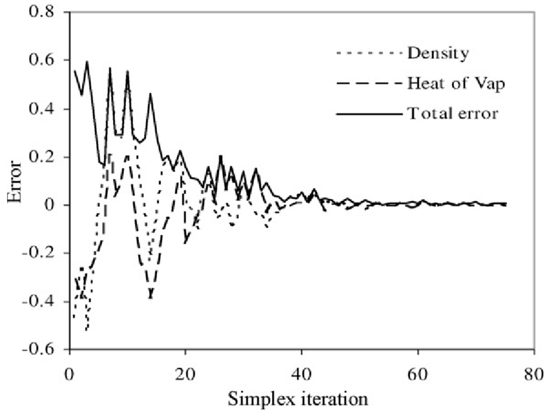

Fig. 6. Tracking the relative error of the calculated density to the target density, the relative heat of vaporization to the target one, and the total error value throughout the optimization.

which in this case gives a much better value of 0.125 W/(mK). The thermal conductivity of the vapor phase of the optimized model was found to be 0.031 W/(mK) which is in agreement with the experimental observation of 0.02 W/(mK).

5. Discussion

A wide range of simulation techniques ranging from simple MD to RNEMD and MC has been employed to predict very diverse physical properties for EO at conditions that require considerable care and effort when conducting experimental measurements. As a contribution to the fourth IFPSC challenge a new EO-model has been created by simplex optimization with respect to the experimental reference values for the liquid density and the heat capacity.

Generally, the reference model (RR) originally developed by Wielopolski and Smith [2] performs quite well. It is very good in reproducing the critical temperature and the vapor pressure, for the other properties however, the values were generally underestimated. The optimized model naturally performs better in terms of liquid density and heat of vaporization, but also with respect to the heat capacity and the transport properties. Generally, the properties accessible by MD or RNEMD for $\mathrm{EO_{opt}}$ were obviously much better predicted than those accessible by GEMC. Hence, the vapor–liquid-coexistence data given in Table 2 display much lower density values over the whole range of chosen temperatures than expected, leading to a much too low critical temperature as well. The associated density, however, is just within tolerable accuracy (8.6% below the experimental value), only the density-profile, when compared to the experiment, appears to be shifted to lower temperatures. Despite of agreeing very nicely for the RR model, the liquid density values of the optimized model obtained at 375 K by GEMC and MD do not match. This mismatching behavior was checked thoroughly (data not shown) and unfortunately is persistent, pointing at problems concerning the transferability of our proposed model.

The novel model was optimized explicitly, but also implicitly with respect to very special conditions, therefore not accounting for the subtle algorithmic nuances between YASP and towhee (e.g. energy and pressure corrections, treatment of long range electrostatic interactions, thermostats, barostats). Obviously this makes the model sensitive to changes and thus endangers its transferability from YASP to other programs.

The simplex algorithm is well known for being a very robust, but not a fast optimization method. Our intention of producing an acceptable model with a (still costly) minimum of computational expense in fact was not entirely satisfied. However, this was not immediately conceivable from the course of the optimization, which is detailed below.

With a starting parameter set of four variables chosen to span the full parameter space, the algorithm took about 40 iterations to achieve an accuracy of 1% for each parameter and about 90 iterations to reach an accuracy of 0.001%. The optimization did abort after 150 iterations while the parameters were only varying in the accuracy of 10^{-4}%. To illustrate the process of the optimization, Fig. 6 shows the relative error of the density, heat of vaporization, and of the total error function in dependence of the number of runs performed (the iteration number). We observe high fluctuations at the beginning of the optimization, which decrease to an absolute value of below 0.1% after 40 iterations and decrease further, the more cycles are performed.

The accuracy of the two target properties (density and heat of vaporization) can also be monitored. Fig. 7 shows the sequence of results calculated from the iteration runs. The wide fluctuation at the beginning of the optimization corresponds to the error fluctuations in Fig. 6. Although all the initial parameter sets produce too high densities and too high values for the heat of vaporization, the iteration converges to a minimum which is located outside the space spanned by the initial parameters.

A similar plot can be produced to show the history of the parameter values. Although all four variables have been optimized at the same time, for the sake of clarity, the two Figs. 8 and 9 show only

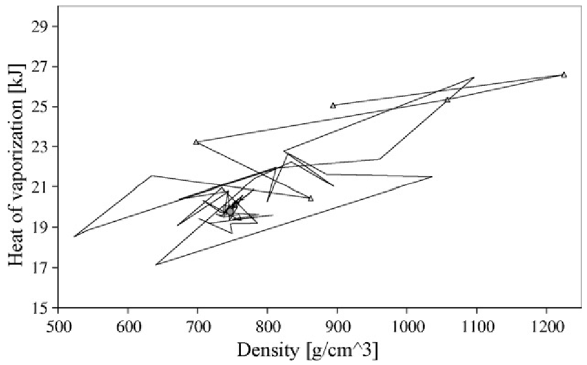

Fig. 7. Sequence of the calculated values against which the optimization was performed: density and heat of vaporization. The results of the initial five parameter sets are shown as light gray triangles while the target value (and the results where the optimization forced the system to) is marked by a dark gray circle.

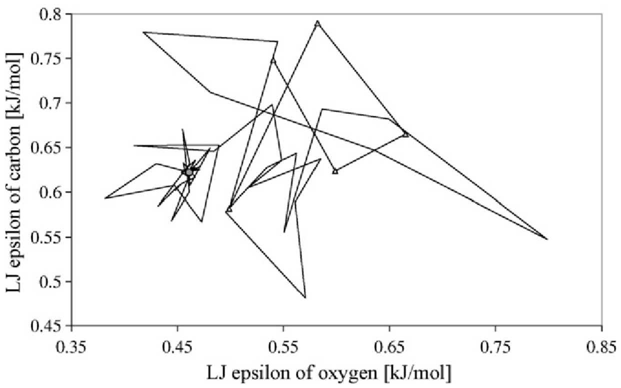

Fig. 8. Values of epsilon during the optimization for carbon and oxygen. Consecutively run values are connected by a line to show the evolution of values during optimization. The values of the five initial parameter sets are shown in light gray triangles while the final parameters are marked by a dark gray circle.

the two ϵ-values and the two σ-values in conjunction. We see here as well that the final parameter set is located outside the parameter space spanned by the initial parameter sets. Convergence is achieved due to the robustness of the method but requires lots of iterations. Nevertheless, computational resources were sufficient to afford this course to obtain parameters that lead to a better behavior of the model with respect to the target properties.

So a broad span of parameter values has been visited during optimization with the adjustments becoming smaller and smaller the closer the final minimum is being encircled. The final σ_{OO}-value is only 1.3% percent below the corresponding value of the RR model, and the σ_{CC} value is 3.2% larger (see Table 1). Given that the assumed bond lengths are slightly shorter, these values appear quite reasonable, as in terms of modeling the LJ-interactions both models are equal. However, the ϵ_{OO} and ϵ_{CC}-values for the optimized model are significantly (i.e. 45 and 20%) lower than those for the RR model. We note that the visited ϵ_{OO}-values fluctuate more than the ϵ_{CC}-values, possibly reflecting the 2:1 ratio of carbon to oxygen atoms, implying that any change in the carbon parameters will have a more pronounced impact on the model-performance than changes in the oxygen parameters. Considering the smaller partial charges in the optimized model, however, these ϵ-values seemed acceptable, too.

In principle, other parameters could have been chosen for optimization. As mentioned above, test runs including e.g. a reparameterization of partial charges have been performed previously, but did not yield promising models. Due to the nature of the contest, the limitation of time prevented investigating other parameter sets and evaluation functions. On the parameters side, especially the incorporation of the hydrogen atoms with (also optimizable) LJ parameters would introduce additional sterical features to the model. On the evaluation function side, taking into account the dipolar momentum would help to control the partial charges and a term controlling the kinetics (e.g. diffusion coefficients or shear viscosity) of the model is also desired for future investigations.

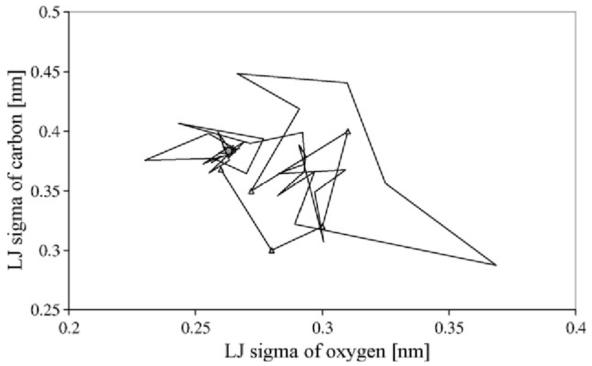

Fig. 9. Values of sigma during the optimization for carbon and oxygen. Consecutively run values are connected by a line to show the evolution of values during optimization. The values of the five initial parameter sets are shown in light gray triangles while the final parameters are marked by a dark gray circle.

The above detailed quality of the results however suggests, that at least a second point in the phase diagram or a parallel GEMC simulation during the optimization cycles would have improved the final outcome, especially with respect to transferability. Both options are equally and considerably consumptive, but obviously necessary. Finally when exploring the parameter space with simplex two mathematical aspects have to be remembered: simplex is a greedy algorithm which looks for local minima. Since the path through the parameter space depends on the starting parameters, the algorithm can get trapped in different local minima. Additionally we have to point out, that optimizing four parameters with only two target values is mathematically an underdetermined system, that consequently has more than one solution. These two issues lead to the fact, that generally simplex finds many parameter sets that fulfill the threshold criterion of sufficient accuracy of the target function. We tested four different starting parameter configurations, which simplex in all cases shifted to the same region in parameters space. The here reported parameter set was the most promising one.

6. Conclusion

Summarizing this work, the optimization of the LJ σ and ε-values of oxygen and carbon against the density and the heat of vaporization by the simplex algorithm has led to a new parameterization of the force field for EO. The strengths of this model lie in the evaluation of transport properties calculated with YASP. We obtained a novel parameter set which was located outside the initially estimated parameter space. Therefore the new parameter set may deviate from tabulated ε- and σ-values of oxygen and carbon which allow a physical interpretation according to LJ-theory; but it represents one solution to the mathematical problem of reproducing the target properties accurately and is a valid candidate for a new parameterization. We have shown hat using distinctly different simulation techniques, such as molecular dynamics, Monte Carlo, and reverse non-equilibrium molecular dynamics, this new parameter set performed in the tasks of predicting phase equilibrium data, caloric data and transport data mostly within the accuracy requested in the IFPSC challenge. Due to the conditions the model was optimized to, the strength of this model lies in describing the liquid phase properties.

For our future work, however, we will consider several options in order to increase the overall performance of this approach: although the simplex optimization procedure has proven to be robust and reliable, the method itself could be substituted by alternative, i.e. faster converging algorithms. In any case, as the accuracy of the repeatedly computed test properties (in our case: liquid density and heat of vaporization) is of utmost importance for limiting the number of iteration cycles, thus even longer equilibration and evaluation periods come into account. Furthermore, adding more test properties to the simplex evaluation function will improve the general performance of a model. The self-diffusion coefficient (if available) would be a natural choice for that purpose, because this value is easily accessible by simulation and then a dynamic property would be linked to the process of parameterization, which accomplishes the so far more static set.

Acknowledgements

We are grateful to Florian Müller-Plathe, Jadran Vrabec, Gerd Winter and Nico van der Vegt for valuable discussions. We also appreciate the support in fitting data given by Sabine Pott.

References

[1] Industrial Fluid Properties Simulation Collective, http://www.ifpsc.org.
[2] P.A. Wielopolski, E.R. Smith, Mol. Phys. 54 (1985) 467–478.
[3] A. Leach, Molecular Modelling, 2nd ed., Prentice Hall, 2001.
[4] B.J. Alder, T.E. Wainwright, J. Chem. Phys. 31 (2) (1959) 459.
[5] W.D. Cornell, P. Cieplak, C.I. Bayly, et al., J. Am. Chem. Soc. 117 (1995) 5179–5197.
[6] A.D. MacKerell Jr., D. Bashford, M. Bellott, et al., J. Phys. Chem. B 102 (1998) 3586–3616.
[7] W.R.P. Scott, P.H. Hunenberger, I.G. Tironi, et al., J. Phys. Chem. A 103 (1999) 3596–3607.
[8] W.L. Jorgensen, D.S. Maxwell, J. Tirado-Rives, J. Am. Chem. Soc. 118 (1996) 11225–11236.
[9] A.K. Rappe, C.J. Casewit, K.S. Colwell, et al., J. Am. Chem. Soc. 114 (1992) 10024–10035.
[10] M.G. Martin, Fluid Phase Equilibria 248 (2006) 50–55.
[11] R.D. Mountain, J. Phys. Chem. B. 109 (2005) 13352–13355.
[12] F. Müller-Plathe, Comput. Phys. Commun. 78 (1993) 77ff.
[13] P. Bordat, F. Müller-Plathe, J. Chem. Phys. 116 (2002) 3362–3369.
[14] MCCCS Towhee, http://towhee.sourceforge.net.
[15] M.J. Frisch, G.W. Trucks, H.B. Schlegel, G.E. Scuseria, M.A. Robb, J.R. Cheeseman, J.A. Montgomery, Jr., T. Vreven, K.N. Kudin, J.C. Burant, J.M. Millam, S.S. Iyengar, J. Tomasi, V. Barone, B. Mennucci, M. Cossi, G. Scalmani, N. Rega, G.A. Petersson, H. Nakatsuji, M. Hada, M. Ehara, K. Toyota, R. Fukuda, J. Hasegawa, M. Ishida, T. Nakajima, Y. Honda, O. Kitao, H. Nakai, M. Klene, X. Li, J.E. Knox, H.P. Hratchian, J.B. Cross, V. Bakken, C. Adamo, J. Jaramillo, R. Gomperts, R.E. Stratmann, O. Yazyev, A.J. Austin, R. Cammi, C. Pomelli, J.W. Ochterski, P.Y. Ayala, K. Morokuma, G.A. Voth, P. Salvador, J.J. Dannenberg, V.G. Zakrzewski, S. Dapprich, A.D. Daniels, M.C. Strain, O. Farkas, D.K. Malick, A.D. Rabuck, K. Raghavachari, J.B. Foresman, J.V. Ortiz, Q. Cui, A.G. Baboul, S. Clifford, J. Cioslowski, B.B. Stefanov, G. Liu, A. Liashenko, P. Piskorz, I. Komaromi, R.L. Martin, D.J. Fox, T. Keith, M.A. Al-Laham, C.Y. Peng, A. Nanayakkara, M. Challacombe, P.M.W. Gill, B. Johnson, W. Chen, M.W. Wong, C. Gonzalez, J.A. Pople, Gaussian 03, Gaussian, Inc., Wallingford CT, 2004.
[16] L.E. Chirlian, M.M. Francl, J. Comp. Chem. 8 (1987) 894ff.
[17] C.M. Brenemann, K.B. Wiberg, J. Comp. Chem. 11 (1990) 361.
[18] H.A. Lorentz, Ann. d. Phys. 12 (1881) 1703–1706.
[19] D. Berthelot, Comptes Rendus de l'Academie des Sciences Paris 126 (1889) 1703–1706.
[20] R. Faller, H. Schmitz, O. Biermann, F. Müller-Plathe, J. Comp. Chem. 20 (1999) 1009–1017.
[21] Numerical Recipes: The Art of Scientific Computing, 3rd ed., Cambridge University Press, 2007.
[22] C. Buckles, P. Chipman, M. Cubillas, M. Lakin, D. Slezak, D. Townsend, K. Vogel, M. Wagner, Ethylene Oxide User's Guide, August, 1999, http://www.ethyleneoxide.com.
[23] C.J. Walters, J.M. Smith, Chem. Eng. Prog. 48 (7) (1952) 337–343.
[24] P. Ghosh, Chem. Eng. Technol. 22 (5) (1999) 379–399.
[26] A. Panagiotopoulos, Mol. Phys. 61 (4) (1987) 813–826.
[27] R. Agrawal, E.P. Wallis, Fluid Phase Equilib. 131 (1997) 51–65.
[30] A. Missenard, Comptes Rendus 260 (1965) 5521.

7.2. Danksagungen

Hiermit bedanke ich mich herzlich bei all denen, die mich zu unterschiedlichsten Zeiten und mit vielfältigster Unterstützung auf dem Weg durch meine Promotionszeit begleitet und schliesslich in der einen oder anderen Form entscheidend zu dieser Dissertation beigetragen haben.

Allen voran danke ich Herrn Prof. Dr. Florian Müller-Plathe, der mir in einem Arbeitsklima des Vertrauens viele wissenschaftliche Freiheiten ließ, während ich mich auf guten Rat verlassen konnte, wann immer ich mit Diskussionsbedarf an seine stets offene Tür klopfte.

Selbstverständlich geht ein großes Dankeschön auch an alle Mitglieder des Arbeitskreises für Theoretische Physikalische Chemie. Ich erinnere mich lebhaft an heftige Diskussionen wissenschaftlicher und nicht wissenschaftlicher Natur und an jede Menge gemeinsam gelöster Probleme. Den folgenden Gruppenmitgliedern gebührt zusätzlich mein spezieller Dank:

... Dr. Volker Weiss, der nicht nur mit aktiver Motivation, sondern auch mit viel physikalisch-chemischem Wissen und ab und zu auch mit einem lektorierenden Rotstift mich in meiner Arbeit weiterbrachte.

... Dr. Michael Böhm, bei dem ich stets eine konstruktiv-kritische Zweitmeinung zu meinen Manuskripten fand.

... Dr. Sudip Roy und Dr. Daniel dos Santos, welche am meisten von allen meine Fragen in computergestützter Chemie zu beantworten hatten.

Mein Dank geht aber auch an Dr. Dirk Reith und Dr. Astrid Maaß vom Fraunhofer Institut für wissenschaftliches Rechnen für eine angenehme, intensive Kollaboration mit einem wertvollen Wissenstransfer.

Desweiteren bedanke ich mich bei all denjenigen Leuten, denen ich es verdanke, dass ich im Bereich der Theoretischen Chemie gelandet bin, wobei Prof. Dr. Wilfred van Gunsteren und Dr. Alice Glättli besonders zu erwähnen sind.

Und dann sind da auch noch die Menschen, die zwar nicht wirklich verstehen, womit genau ich mich beschäftigte, die für mich in der Zeit der Promotion aber genauso wichtig waren:

Ich danke meinen Eltern, die immer an mich geglaubt haben, auch wenn der einzige Naturwissenschaftler in der Familie sie mal wieder mit Fachausdrücken zutextete.

Ebenso danke ich meinen Freunden in Deutschland, die mich mit offenen Armen neu in ihren Reihen aufnahmen, und meinen Freunden in der Schweiz, die mich nicht vergessen haben, auch wenn zwischen uns doch ein paar hundert Kilometer Distanz lagen.

Und mein letzter, ganz spezieller Dank geht an Patrick. Danke für alles.

7.3. Eidesstattliche Erklärungen

Thomas Müller
Tannenweg 11
64354 Reinheim

30.10.2009

Eidesstattliche Erklärung

Ich erkläre hiermit bei Eides statt, dass ich meine Dissertation selbstständig und nur mit den angegebenen Hilfsmitteln angefertigt habe.

Thomas Müller

Thomas Müller
Tannenweg 11
64354 Reinheim

30.10.2009

Erkärung

Ich erkläre hiermit, noch keinen Promotionsversuch unternommen zu haben.

Thomas Müller

7.4. Akademischer Lebenslauf

Persönliche Angaben

Geburtsdatum/-ort: 4. Januar 1978 in Wintherthur (CH)
Eltern: Jakob und Esther Müller

Ausbildung

Promotion

2005-2009	Promotion in der Arbietsgruppe von Prof. Dr. F. Müller-Plathe zunächst an der International University Bremen (Jan.-Mai 2005) danach an der Technischen Universität Darmstadt

Studium

2000-2004	Chemiestudium an der ETH Zürich Schwerpunktthemen: Physikalische Chemie Informatikgestützte Chemie Diplomarbeit: NQR-Messungen von ^{14}N in Glycinen in der Gruppe von Prof. Dr. B. Meier
1998-2000	3 Semester Grundstudium in Physik an der ETH Zürich

Schule

1993-1998	Lateingymnasium in CH-9630 Wattwil
1991-1993	Sekundarschule in CH-9533 Kirchberg
1990-1991	Primarschule in CH-9533 Kirchberg
1985-1990	Primarschule in CH-8408 Winterthur

Wissenschaftliche Publikationen:

T.J. Müller, F. Müller-Plathe, „Determining the local shear viscosity of a lipid bilayer system by reverse non-equilibrium molecular dynamics simulations“, ChemPhysChem **10** (2009) 2305-2315

T.J. Müller, F. Müller-Plathe, „A comparison of sulfur mustard and heptane penetrating a dipalmitoylphosphatidylcholine bilayer membrane“, J. Haz. Mater. **138** (2009) 13-24

T.J. Müller, S. Roy, W. Zhao, A. Maaß, D. Reith, “Economic simplex optimization for broad range property prediction: Strength and weaknesses of an automated approach for tailoring of parameters”, Fluid Phase Equilib. **274** (2008) 27-35

T.J. Müller, M. Al-Samman, F. Müller-Plathe, „The influence of thermostats and manostats on reverse nonequilibrium molecular dynamics calculations of fluid viscosities”, J. Chem. Phys. **129** (2008) 014102

Konferenzteilnahme mit Posterbeitrag:

2008	Soft Matter in Aachen
2007	Rhein-Main Modelling Day an der TU Darmstadt Soft Matter Days in Salerno
2006	Rhein-Main Modeling Day am MPI Mainz
2005	CCP5 Summer School in Cardiff

Darmstadt, 30. Oktober, 2009